

# DOE/NASA TECHNICAL MEMORANDUM

## DOE/NASA TM-78165

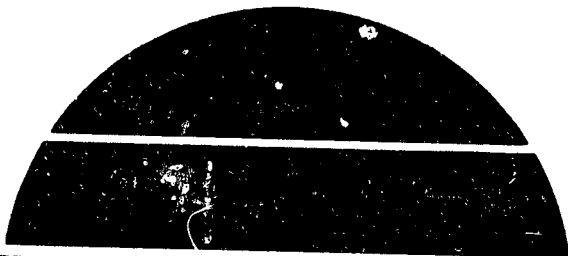
### USE OF THE MARSHALL SPACE FLIGHT CENTER SOLAR SIMULATOR IN COLLECTOR PERFORMANCE EVALUATION

Prepared by

**William R. Humphries**  
Structures and Propulsion Laboratory

National Aeronautics and Space Administration  
George C. Marshall Space Flight Center, Alabama

For the U. S. Department of Energy



(NASA-TM-78165) USE OF THE MARSHALL SPACE  
FLIGHT CENTER SOLAR SIMULATOR IN COLLECTOR  
PERFORMANCE EVALUATION (NASA) 128 p HC  
A07/MF A01

N78-21605

CSCL 10A

Unclas

G3/44

14127

# U.S. Department of Energy



## Solar Energy

## ACKNOWLEDGMENTS

Design, fabrication, and testing in a facility of this type is by necessity a multidisciplinary task involving many participants. Although it is impractical to mention all those who were involved in these activities, the author would like to recognize a few individuals and groups who were instrumental in getting the facility into operation.

The Center is indebted to the Department of Energy (formerly the Energy Research and Development Administration) for funding of this facility. The Marshall Solar Heating and Cooling Program Office provided program goals and overview of this project vital to successful completion. Mr. Don Bowden, past program manager, and later Mr. John Price, deputy manager, gave valuable support. Mr. Norm Thomas, as the program officer in charge of the simulator activity, has directed this program from its inception.

Cooperation by the Lewis Research Center in disclosing all facets of their 4 by 4 ft solar simulator design was extremely helpful. Many of the design features similar to those of the Lewis facility were embodied in the MSFC simulator design in an effort to expedite completion of the project. Messrs. F. Simon, K. Yass, R. Vernon, and P. Harlamert were especially helpful in this regard.

Mr. Jim Brock of the Facilities Office was in charge of facility structure, electrical, and other installation design functions. In the Science and Engineering (S&E) Directorate a number of individuals from the labs should be acknowledged. Messrs. Bill Richardson and Bernie Wiesenmaier provided project technical direction within the S&E Directorate. In the Structures and Propulsion Laboratory, Messrs. George Hopson, Joe Cody, and Dr. Wayne Little shared technical direction in the initial phases of design, particularly in regard to the collector test requirements and thermal/fluid design goals for the simulator. Messrs. Fred zur Burg and George Gerry provided general mechanical design requirements and drawing layouts, as well as solar array and tilt table designs. Dr. Pat Espy of the Space Sciences Laboratory provided initial optical arrangement design, coordinating this phase of the research on these features with the Lewis Center. Electrical system design was provided by Messrs. Clyde Jones, George Smith, and Paul White of the Electronics and Control Laboratory. Mr. Don Griner, also of the Electronics and Control Laboratory, performed optical and performance measurements on the simulator, as well as the lamp/lens combination. He also was instrumental in initial troubleshooting and modification to achieve acceptable facility performance. He and Mr. Charles Hawkins designed and built the mapping device. Dr. Tom McCrickard of the Test Laboratory coordinated facility installation modifications and test activities. Mr. Cary Riley, also of the Test Laboratory, designed the fluid/thermal simulator and performed initial facility checkout tests, and Mr. Paul Cates installed the control system in the test stand.

Wyle Laboratories, Inc., on contract to MSFC, is currently operating the test facility. Mr. Ralph Barber directs these activities with technical assistance from Dr. Howard Yen. Mr. Steve Patrick conducted initial tests after facility transfer to Wyle with Mr. Ken Shih, who is currently performing the test conductor duties.

The author is indebted to Mr. Ken Shih and Dr. Howard Yen who assisted him in gathering the information for this report.

4. TITLE AND SUBTITLE <b>Use of the Marshall Space Flight Center Solar Simulator in Collector Performance Evaluation</b>		5. REPORT DATE <b>April 1978</b>	
7. AUTHOR(S) <b>William R. Humphries</b>		6. PERFORMING ORGANIZATION CODE	
9. PERFORMING ORGANIZATION NAME AND ADDRESS <b>George C. Marshall Space Flight Center Marshall Space Flight Center, Alabama 35812</b>		8. PERFORMING ORGANIZATION REPORT #	
12. SPONSORING AGENCY NAME AND ADDRESS <b>National Aeronautics and Space Administration Washington, D. C. 20546</b>		10. WORK UNIT NO.	
		11. CONTRACT OR GRANT NO.	
15. SUPPLEMENTARY NOTES <b>Prepared by Structures and Propulsion Laboratory, Science and Engineering</b>		13. TYPE OF REPORT & PERIOD COVERED <b>Technical Memorandum</b>	
		14. SPONSORING AGENCY CODE	
16. ABSTRACT  <p>Details of the Marshall Space Flight Center (MSFC) solar simulator construction and operating characteristics are presented. Actual measured values from simulator checkout tests are detailed. Problems encountered during initial startup are discussed and solutions described. Techniques utilized to evaluate collector performance from simulator test data are given. Performance data generated in the simulator are compared to equivalent data generated during natural outdoor testing. Finally, a summary of collector performance parameters generated to date as a result of simulator testing are given.</p>			
17. KEY WORDS		18. DISTRIBUTION STATEMENT  <b>Unclassified - Unlimited</b>	
19. SECURITY CLASSIF. (of this report) <b>Unclassified</b>	20. SECURITY CLASSIF. (of this page) <b>Unclassified</b>	21. NO. OF PAGES <b>127</b>	22. PRICE <b>NTIS</b>

# TABLE OF CONTENTS

	Page
SUMMARY .....	1
I. INTRODUCTION .....	1
II. FACILITY DESCRIPTION .....	2
A. Sun Simulator Description .....	3
B. Solar System Simulator Description .....	14
C. Basic Facility .....	23
D. Instrumentation .....	29
III. SIMULATOR EVALUATION AND OPERATION .....	30
A. Sun Simulator Performance .....	30
B. Anomalies .....	40
C. Lamp Life Tests .....	42
D. Flux Mapping .....	44
E. Wind Simulation .....	45
IV. COLLECTOR PERFORMANCE EVALUATION .....	48
A. Stagnation Testing .....	48
B. Collector Efficiency .....	48
C. Incident Angle Modifier .....	62
D. Time Constant .....	66
E. Variations from ASHRAE Standard 93-77 .....	73
V. SIMULATOR TESTING .....	76
A. Advantages of Simulator Testing .....	76
B. Comparison of Outdoor and Simulated Indoor Tests .....	77
C. Production Collector Tests .....	86
REFERENCES .....	92

## TABLE OF CONTENTS (Concluded)

	Page
APPENDIX A — MEASUREMENT DEVICES .....	95
APPENDIX B — COLLECTOR OBSERVATIONS AND MEASUREMENTS .....	99
APPENDIX C — SIMULATOR OPERATING PROCEDURES .....	103
APPENDIX D — PROPERTIES OF 50 PERCENT BY VOLUME (52.7 PERCENT BY WEIGHT) ETHYLENE GLYCOL IN WATER .....	113

# LIST OF ILLUSTRATIONS

Figure	Title	Page
1.	Test facility arrangement . . . . .	4
2.	Tungsten-halogen lamps . . . . .	5
3.	Optical layout of single lens/lamp combination . . . . .	6
4.	Lamp/lens illumination array . . . . .	6
5.	Transmittance of lens . . . . .	7
6.	Fresnel lens . . . . .	9
7.	View of exposed lamp housing . . . . .	10
8.	Lamp/lens cooling system flow arrangement . . . . .	11
9.	Control console . . . . .	12
10.	Grid network and electrical arrangement . . . . .	13
11.	Tilt table with mapping rig . . . . .	15
12.	Air loop thermal simulator schematic . . . . .	18
13.	Air loop simulator arrangement . . . . .	20
14.	Liquid loop simulator schematic . . . . .	21
15.	Liquid loop simulator arrangement . . . . .	22
16.	Basic facility . . . . .	24
17.	Overall view of simulator . . . . .	27
18.	MSFC layout . . . . .	28

## LIST OF ILLUSTRATIONS (Continued)

Figure	Title	Page
19.	Simulator test arrangement . . . . .	31
20.	Lens housing and attenuation screen installation . . . . .	35
21.	Typical solar flux map . . . . .	38
22.	Plot of relative intensity versus angle . . . . .	39
23.	Variation of lamp/lens spectral irradiance with wavelength . . . . .	39
24.	Lamp voltage control scheme . . . . .	43
25.	Test plane overall flux level versus power controller setting . . . . .	46
26.	Uniformity measurement apparatus . . . . .	46
27.	Typical wind velocity profile . . . . .	47
28.	Collector area definitions . . . . .	50
29.	Typical collector surface measurement locations . . . . .	55
30.	Collector indoor thermal performance test . . . . .	56
31.	Overall collector efficiency data . . . . .	59
32.	Effect of wind on collector efficiency . . . . .	60
33.	Typical variation of heat loss with temperature . . . . .	61
34.	Variation of transmittance with incidence angle . . . . .	63
35.	Variation of normal flux with incidence angle . . . . .	65

## LIST OF ILLUSTRATIONS (Concluded)

Figure	Title	Page
36.	Preferential incidence angle modifier . . . . .	67
37.	Collector with preferential incidence angle modifier . . . .	68
38.	Collector incidence angle modifier versus east-west incidence angle . . . . .	69
39.	Collector incident angle modifier versus modifier parameters . . . . .	70
40.	Typical collector time constant plot . . . . .	74
41.	MSFC prototype air collector . . . . .	79
42.	Prototype liquid collector . . . . .	80
43.	Air collector outdoor/indoor collector efficiency comparison . . . . .	82
44.	Liquid collector outdoor/simulator efficiency comparison . . . . .	83
45.	Liquid collector efficiency . . . . .	84
46.	Air collector efficiency . . . . .	85
47.	Liquid type production collector efficiency . . . . .	88
48.	Air type production collector efficiency . . . . .	89
C-1.	Solar simulator setup . . . . .	105
C-2.	Solar simulator controls . . . . .	110



## LIST OF TABLES

Table	Title	Page
1.	Measurement Accuracy . . . . .	29
2.	Collector Performance Measurements . . . . .	34
3.	Features of Collectors Used in Simulator Evaluation . . . .	81
4.	Summary of Production Collector Features . . . . .	87
5.	Production Collector (Liquid) Efficiency Parameters . . .	89
6.	Production (Air) Collector Efficiency Parameters . . . . .	90
7.	Production Collector Incident Angle Modifiers . . . . .	90
8.	Production Collector Time Constant Data . . . . .	91

## NOMENCLATURE

<u>Symbol</u>	<u>Definition</u>
A	Cross-sectional area, m <sup>2</sup> (ft <sup>2</sup> )
A <sub>a</sub>	Transparent frontal area of collector, m <sup>2</sup> (ft <sup>2</sup> )
A <sub>L</sub>	Heat loss area of collector, m <sup>2</sup> (ft <sup>2</sup> )
A <sub>g</sub>	Gross outside collector area, m <sup>2</sup> (ft <sup>2</sup> )
A <sub>s</sub>	Shaded area of collector, m <sup>2</sup> (ft <sup>2</sup> )
a, b	Linear equation constant, dimensionless
℄	Centerline
d	Distance, m (ft)
F <sub>R</sub>	Heat removal factor, dimensionless
F'	Collector flow efficiency factor, dimensionless
FS	Full scale
h	Height m (ft)
I	Solar irradiation incident upon the plane of the collector, W/m <sup>2</sup> (Btu/h-ft <sup>2</sup> )
i	Arbitrary index
K <sub>τα</sub>	Incident angle modifier, dimensionless
L	Length m (ft)
ṁ	Mass flowrate of the transfer fluid, kg/s (lb/h)
N	Total number index

## NOMENCLATURE (Continued)

<u>Symbol</u>	<u>Definition</u>
$\dot{Q}$	Rate of heat flow, W (Btu/h)
$\dot{Q}_i$	Rate of energy "in," W (Btu/h)
$\dot{Q}_o$	Rate of energy "out," W (Btu/h)
$\dot{Q}_u$	Rate of useful energy extracted from collector, W (Btu/h)
$\bar{s}$	Average flux rate, W/m <sup>2</sup> (Btu/h-ft <sup>2</sup> )
$s_i$	Instantaneous flux rate, W/m <sup>2</sup> (Btu/h-ft <sup>2</sup> )
$T_a$	Ambient air temperature °C (°F)
$T_{fo}$	Temperature of the transfer fluid leaving the collector, °C (°F)
$\bar{T}_f$	Average fluid temperature, °C (°F)
$\bar{T}_p$	Average temperature of the collector plate, °C (°F)
$T_{fi}$	Temperature of fluid entering collector, °C (°F)
$t$	Time, decimal hours or seconds
$U_L$	Solar collector heat transfer loss coefficient, W/m <sup>2</sup> · °C (Btu/h-ft <sup>2</sup> -°F)
$\dot{V}$	Volumetric flowrate, m <sup>3</sup> /s (ft <sup>3</sup> /min)
$W$	Width, m (ft)

**ORIGINAL PAGE IS  
OF POOR QUALITY**

## NOMENCLATURE (Continued)

<u>Symbol</u>	<u>Definition</u>
$\alpha$	Absorptance, dimensionless
$\Gamma$	Collector parameters, $\frac{T - T_a}{I_n}, \frac{m^2 \cdot C}{W} \left( \frac{ft^2-h-\circ F}{Btu} \right)$
$\eta$	Collector efficiency based on overall area, dimensionless
$\theta$	Angle of incidence between direct solar rays and a normal to the collector surface, deg
$\rho$	Density, $kg/m^3$ ( $lb/ft^3$ )
$\tau$	Transmittance of the solar collector cover plate, dimensionless
$\tau_e$	Effective transmissivity — absorptivity factor at normal incidence, dimensionless
$\phi$	Electrical phase

### Subscripts

1,2	Arbitrary indices
a	Aperture
c	Collector
e	Effective

## NOMENCLATURE (Concluded)

### Subscripts

### Definition

f	Fluid
g	Gross
i	Inlet
L	Loss
n	Normal
o	Outlet
s	Shaded
u	Useable
$\theta$	Incidence angle

## USE OF THE MARSHALL SPACE FLIGHT CENTER SOLAR SIMULATOR IN COLLECTOR PERFORMANCE EVALUATION

### SUMMARY

The Marshall Space Flight Center (MSFC) Sun simulator and collector testing techniques are described herein. Details of simulator construction are given along with actual measured simulation performance characteristics. Collector testing procedures are described giving deviations from current standard practices. Initial comparative performance data from selected air and liquid collector tests are presented for both indoor simulator tests and outdoor tests. These data indicate exceptionally good collector efficiency correlations between the two tests. Comparisons prove sufficiently the validity of using the MSFC simulator for nonconcentration flat plate collector configuration performance evaluations.

### I. INTRODUCTION

As part of the National Aeronautics and Space Administration's (NASA) role in support of the Department of Energy (DOE), a test facility has been constructed at MSFC to evaluate solar collector performance under simulated outdoor operating conditions. The primary goal of this facility is to evaluate the performance capability of flat plate collectors which utilize either air or liquid transport media.

The stimuli for this facility is the time and labor savings derived from its use, as well as improved test results associated with the more controlled environment it allows. The environment improvements are the result of testing under conditions not subject to the capriciousness of ambient conditions.

Environmental parameters the facility can simulate include sunfall conditions such as solar radiation intensity, solar spectrum, collimation, and uniformity, as well as solar attitude. Prevailing wind conditions of velocity and

direction can also be simulated. The facility is capable of reproducing solar system conditions imposed on the collector, including transport media type and flowrate, collector fluid inlet temperature, and geometric factors of collector tilt and azimuth angles.

Sun simulation is achieved by 405 tungsten-halogen lamps which provide a source of energy near the solar spectrum at air mass 2. Each lamp is paired with a Fresnel lens for energy collimation. This combination forms a  $27 \times 15$  illumination array. The array, which is mounted with its long axis tilted up, is attached to an apparatus capable of being tilted around a horizontal axis. The array can irradiate a 1.2 by 2.4 m (4 by 8 ft) planar surface area. Collector orientation and thermal/fluid simulations are provided by a tilt table arrangement in conjunction with either an air or a liquid thermal/fluid loop. Wind velocity and direction on the collector are provided by two portable floor fans. These elements are all housed in a thermostatically controlled high bay building in the MSFC test complex.

Typically, testing in the simulator is performed to acquire collector efficiency data, the collector time constant, incident angle modifier data, and stagnation temperature values. Other testing may be performed, but is not discussed herein. The techniques utilized to make these evaluations follow in general the guidelines given in ASHRAE Standard 93-77, "Methods of Testing to Determine the Thermal Performance of Solar Collectors." However, a few deviations from this standard are noted.

Comparison of efficiency data generated in a natural outdoor environment to those generated in the simulator are presented. These comparisons are made for a double covered, selectively coated liquid collector and a single covered, nonselectively coated air collector. The comparisons indicate outdoor efficiency data can be reproduced in the simulator to within 6 percent of the outdoor measurement.

## II. FACILITY DESCRIPTION

The facility includes the capability to simulate sunlight on the collector surface as its primary feature. However, it also provides a capability to simulate other conditions imposed by the solar system (i.e., storage and heating and/or cooling subsystems inputs), as well as natural environment conditions

important to collector performance such as wind simulation and solar attitude. These simulations are accomplished by the major elements of the facility, which are the Sun simulator, the solar system or load simulator, and the basic facility (Fig. 1). A detailed description of each of the elements is given in the following paragraphs.

## A. Sun Simulator Description

The key element of this facility is the Sun simulator. This includes the lamp housing, lens housing, lamp/lens cooling equipment, and control equipment required to support these. Descriptions of these items follow.

1. Lamps. The simulator uses 405 GE Model ELH quartzline lamps to produce the solar intensity and radiation spectrum. These lamps are rated at 300 W at 120 V. They use a tungsten filament with an equivalent source temperature of 1843°C (3350°F). The filament is housed in a quartz bulb filled with halogen gas which produces an energy spectrum similar to that of the Sun at air mass 2. The bulb is attached to a dichroic-coated glass reflector. This ellipsoidal reflector is mounted to the base of the bulb to limit the direction of light from the bulb. It also serves to limit infrared emission due to the selective nature of the reflector reflectivity.

Early lamps had stippled reflectors, while later versions use a faceted surface texture (Fig. 2).

2. Fresnel Lens. Each lamp is mounted in a housing immediately opposite the lens housing. Each lens/lamp combination is mounted so that they have optically coincident axes (Fig. 3). Lenses are mounted with the refracting grooved surface facing the lamps. Spacing between corresponding lens/lamp pairs is 17.78 cm (7 in.). This spacing fixes the image created by the lamp 2.54 cm (1 in.) in front of the lamp reflector face and at the lens focal point. The 405 lens array is arranged in a 27 × 15 array (Fig. 4).

Focusing of energy through the lens is achieved by multiple circular line grooves cut into the plastic with a groove density of 125 lines per inch. These grooves refract light rays from the lamps so that the focus of energy occurs at a point 15.24 cm (6 in.) from the lens. The lens transmittance properties have been measured and were reported in Reference 1. These data are reproduced in Figure 5.

ORIGINAL PAGE IS  
OF POOR QUALITY



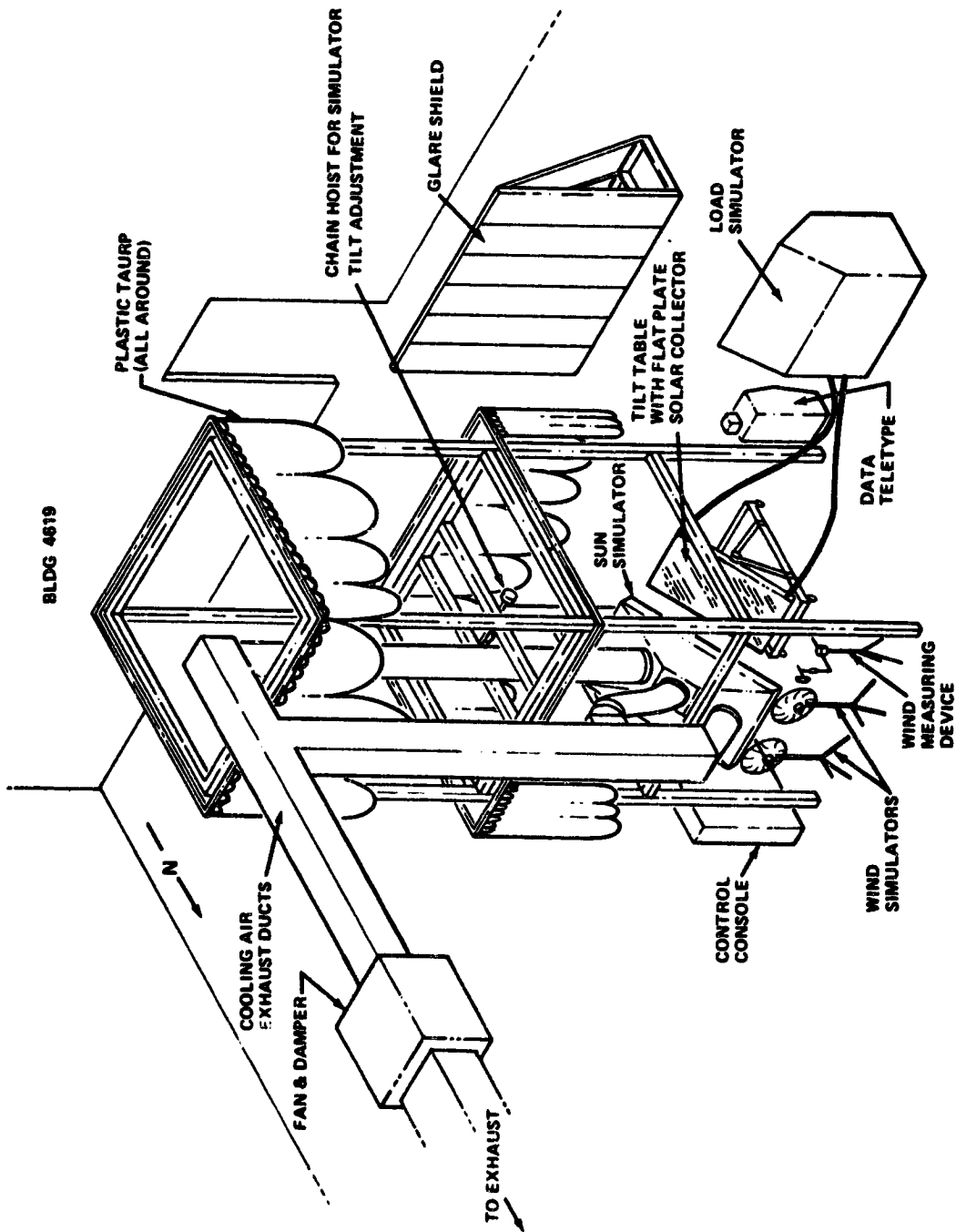


Figure 1. Test facility arrangement.

ORIGINAL PAGE IS  
OF POOR QUALITY

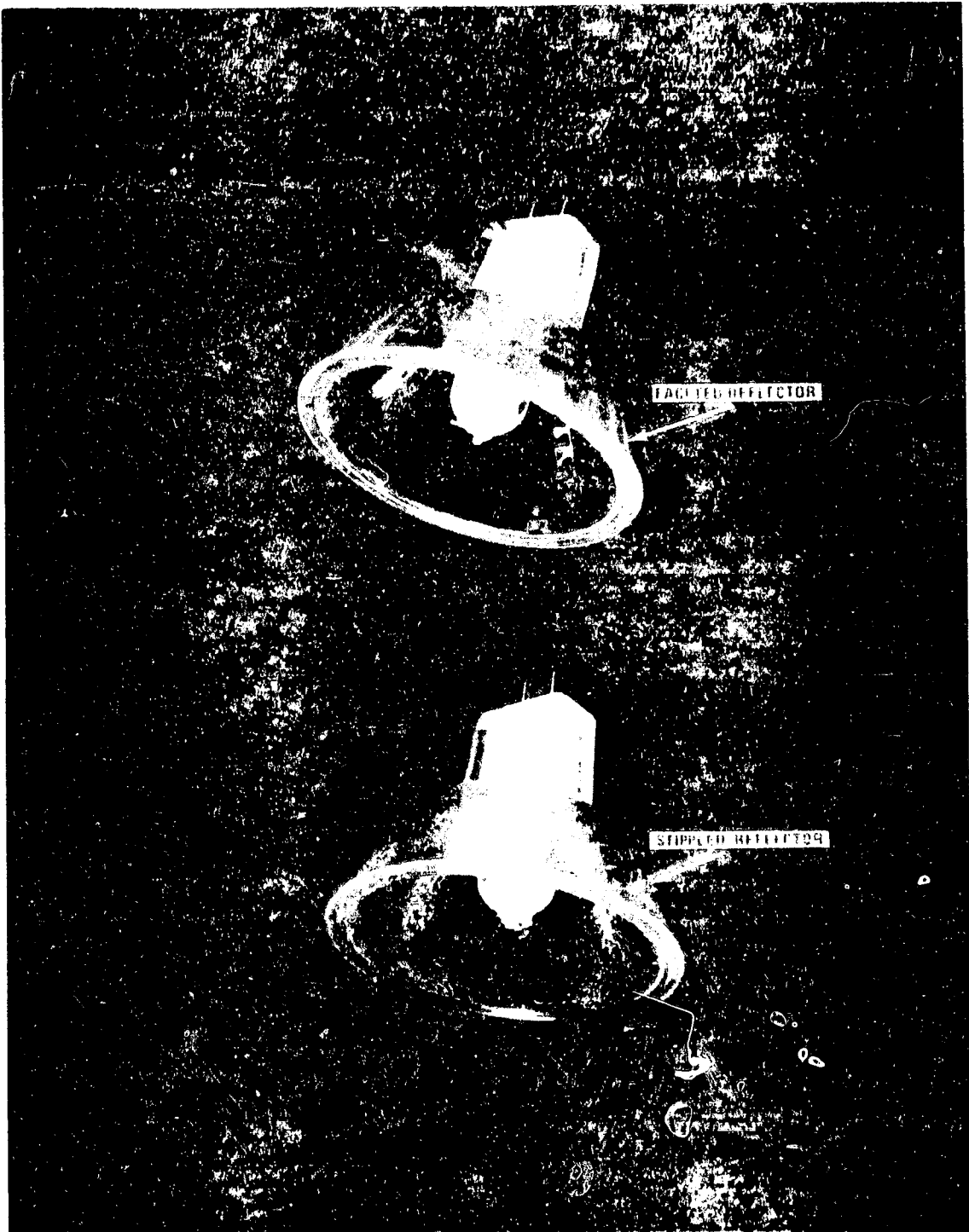


Figure 2. Tungsten-halogen lamps.

ORIGINAL PAGE IS  
OF POOR QUALITY

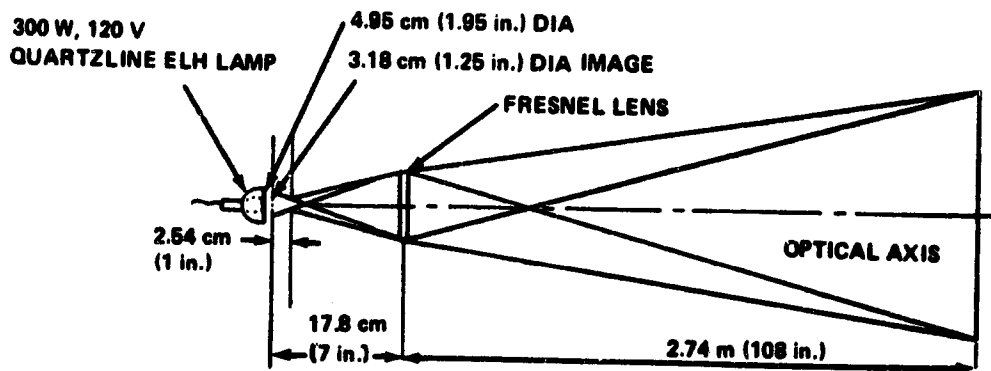


Figure 3. Optical layout of single lens/lamp combination.

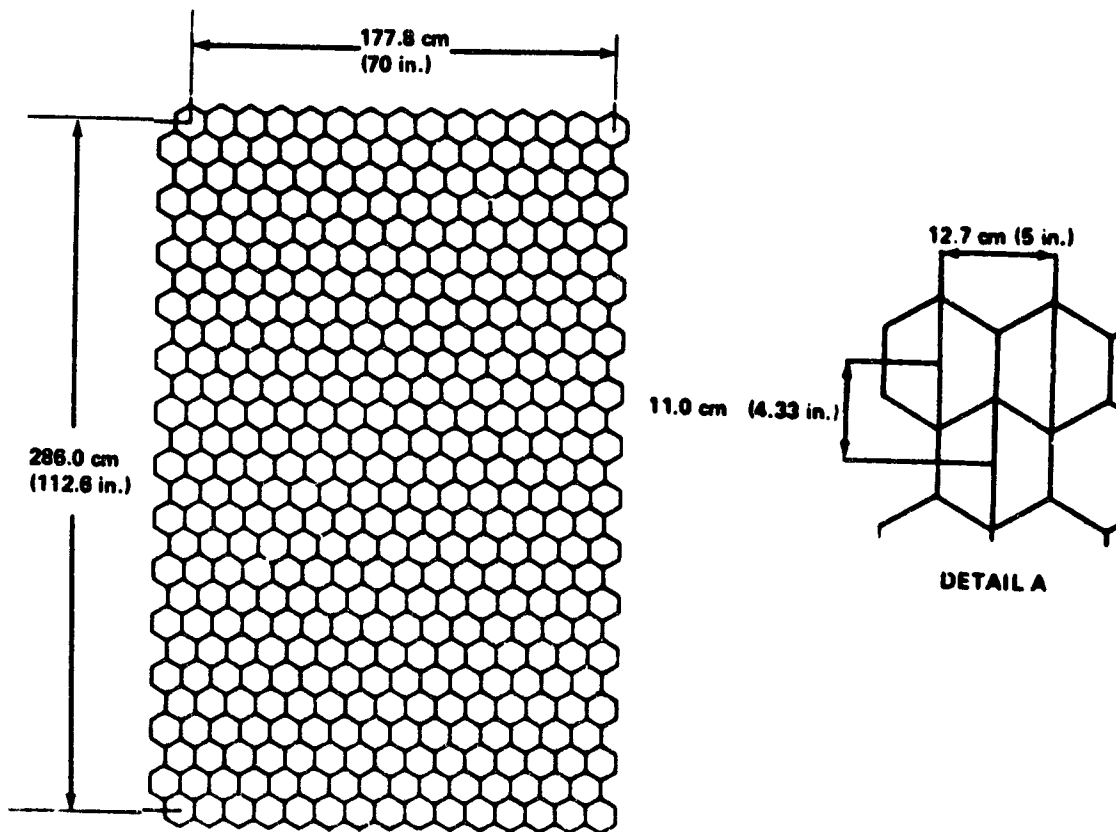


Figure 4. Lamp/lens illumination array.

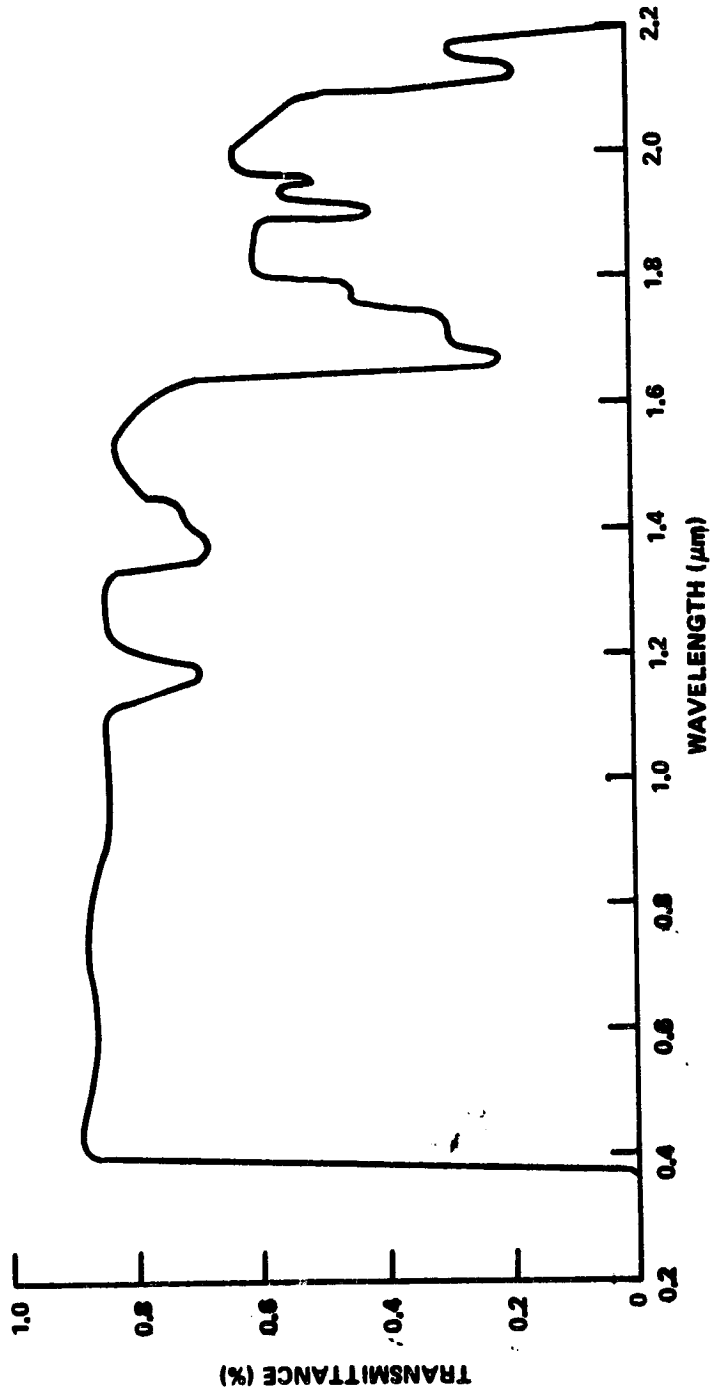


Figure 5. Transmittance of lens.

ORIGINAL PAGE IS  
OF POOR QUALITY

Lenses are made of 0.6 mm (0.1625 in.) thick acrylic. Circular stock is cut to a hexagonal shape 12.7 cm (5 in.) across flats. Semicircular notches are cut in opposite flats to allow mounting (Fig. 6). The lenses are secured to the lens housing by lightly torquing the mounting bolts. The lens housing is hinged to allow access to the lamps (Fig. 7).

3. Lamp/Lens Cooling. Cooling is provided the lamps and lenses by ingesting room air through eight household type fiberglass filters. The air then passes between the lenses and the lamps and through orifices in the lamp housing located adjacent to each lamp. Deflectors at the outlet of these orifices direct cooling air across the lamp base and into a tapered plenum immediately behind the lamp housing. The heated air is mixed in the plenum and drawn off through a 63.5 cm (25 in.) diameter duct. From the duct, the warm air may be either exhausted outside or returned to the high bay building (Fig. 8).

A variable position damper, located in the exhaust duct upstream of the fan, is used to control the cooling air flowrate. The damper position is manually set at the control console to maintain the lamp base temperature at or near an average of 288°C (550°F). A 283 m<sup>3</sup>/min (10 000 cfm) constant speed fan supplies air flow for this system. Opening and closing of the damper changes the flow resistance to allow the flowrate to be adjustable from a low of 125 m<sup>3</sup>/min (4400 cfm) to a high of 311 m<sup>3</sup>/min (11 000 cfm).

4. Controls. Lamp voltage control (and thereby flux intensity) and cooling flowrate is provided through a console located immediately adjacent to the simulator (Fig. 9). Simulator flux intensity control is manual, utilizing a 150 kVA Research Incorporated voltage controller, which was surplus from a past space test program. The device is a three-phase 208 V SCR angle and phase firing circuit which achieves root mean square (RMS) voltage output control by eliminating segments of the ac voltage input to the lamps. This is done by chopping portions of the sinusoidally varying voltage. This chopping provides a lower (or higher) average RMS voltage to the lamps. Lamps are connected selectively to each of the three voltage phases by zones, so that each quadrant of the Sun simulator is on opposite voltage phases. Figure 10 shows the lamp electrical phase arrangement, as well as the lamp/lens numbering scheme. Selective location of lamps within phases is used in an attempt to smooth non-uniformities in flux intensity resulting from voltage disparities between phases. The lamps are electrically wired so that they may be switched on and off in groups of five.

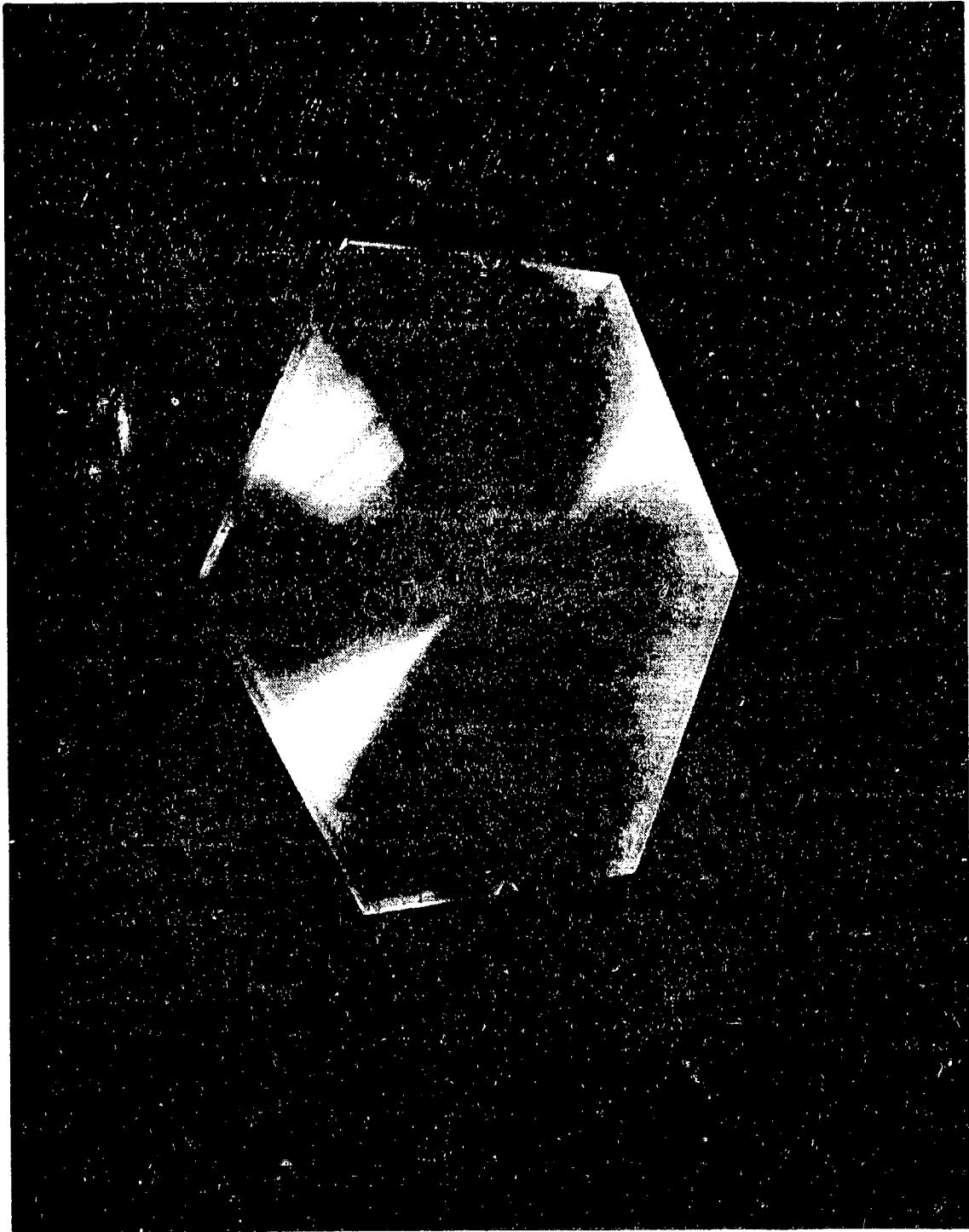


Figure 6. Fresnel lens.

**ORIGINAL PAGE IS  
OF POOR QUALITY**

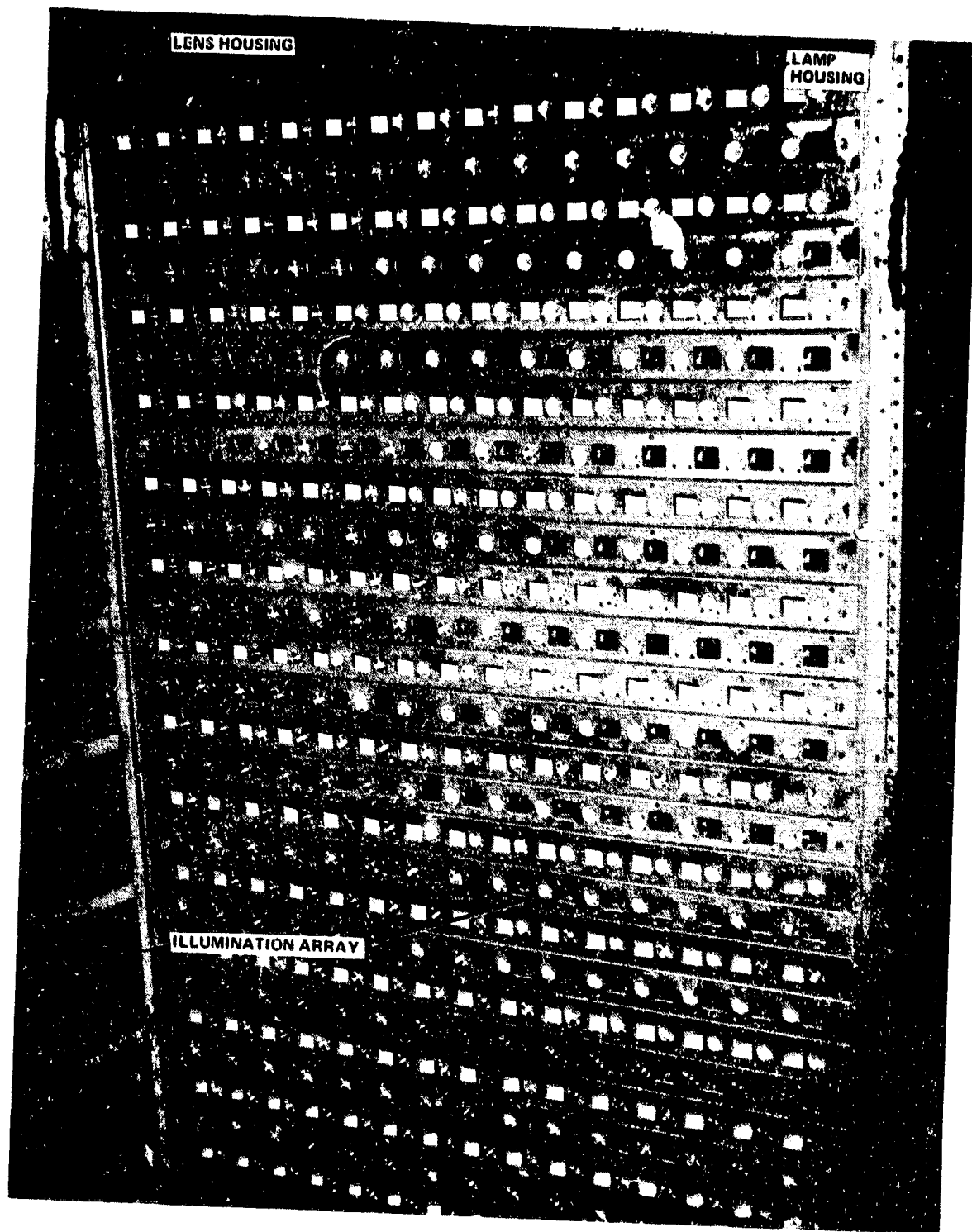


Figure 7. View of exposed lamp housing.

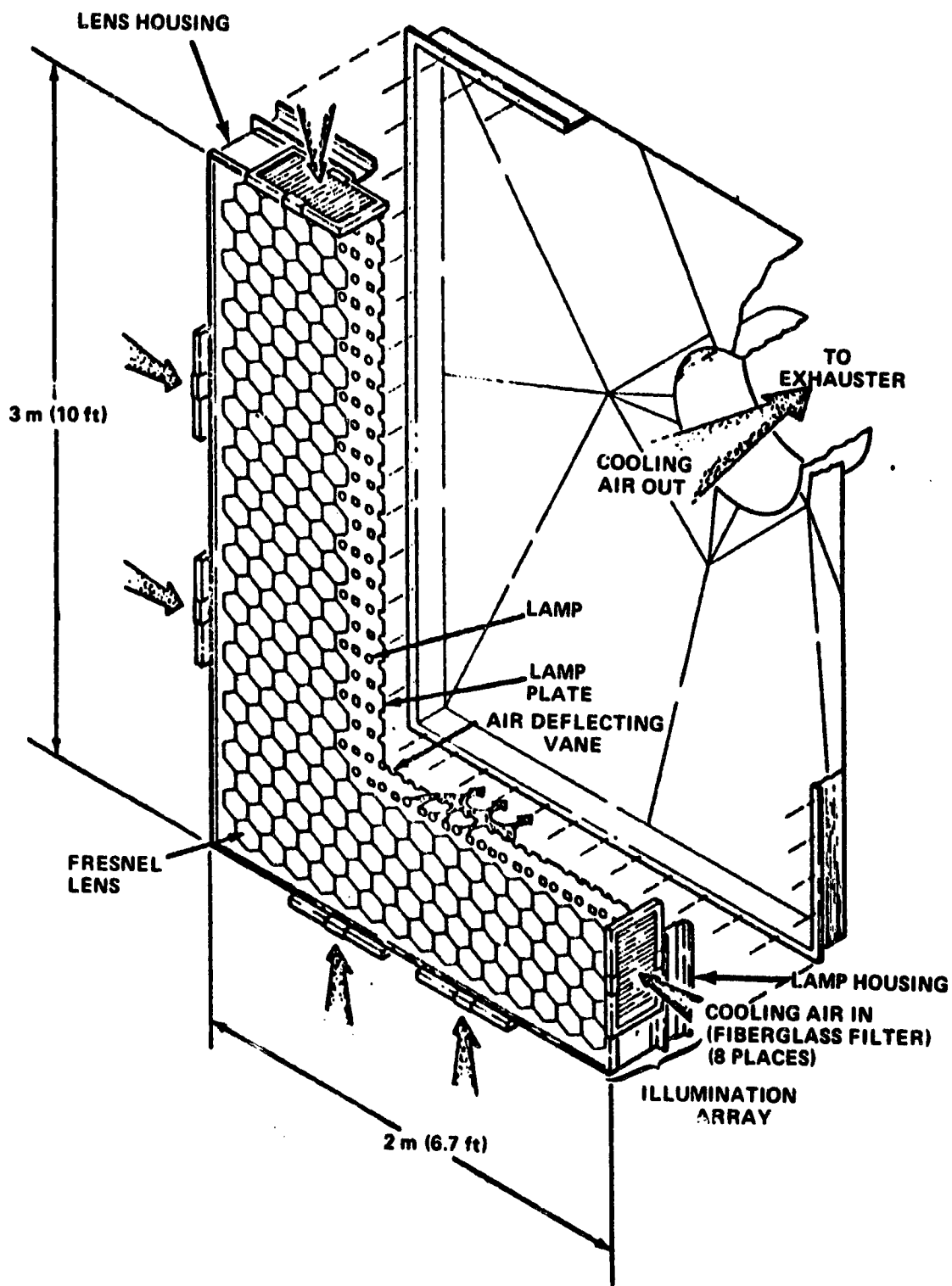


Figure 8. Lamp/lens cooling system flow arrangement.



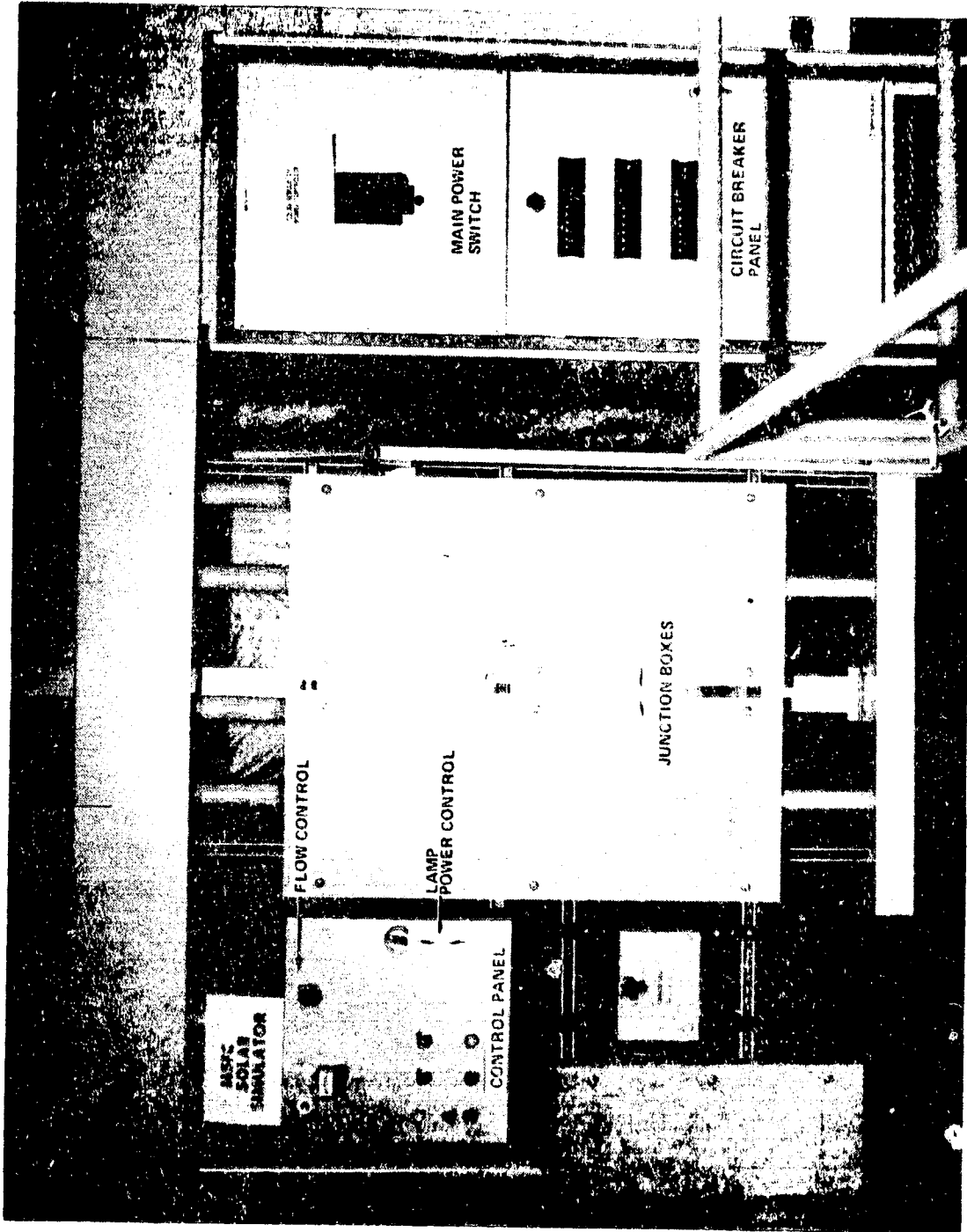


Figure 9. Control console.

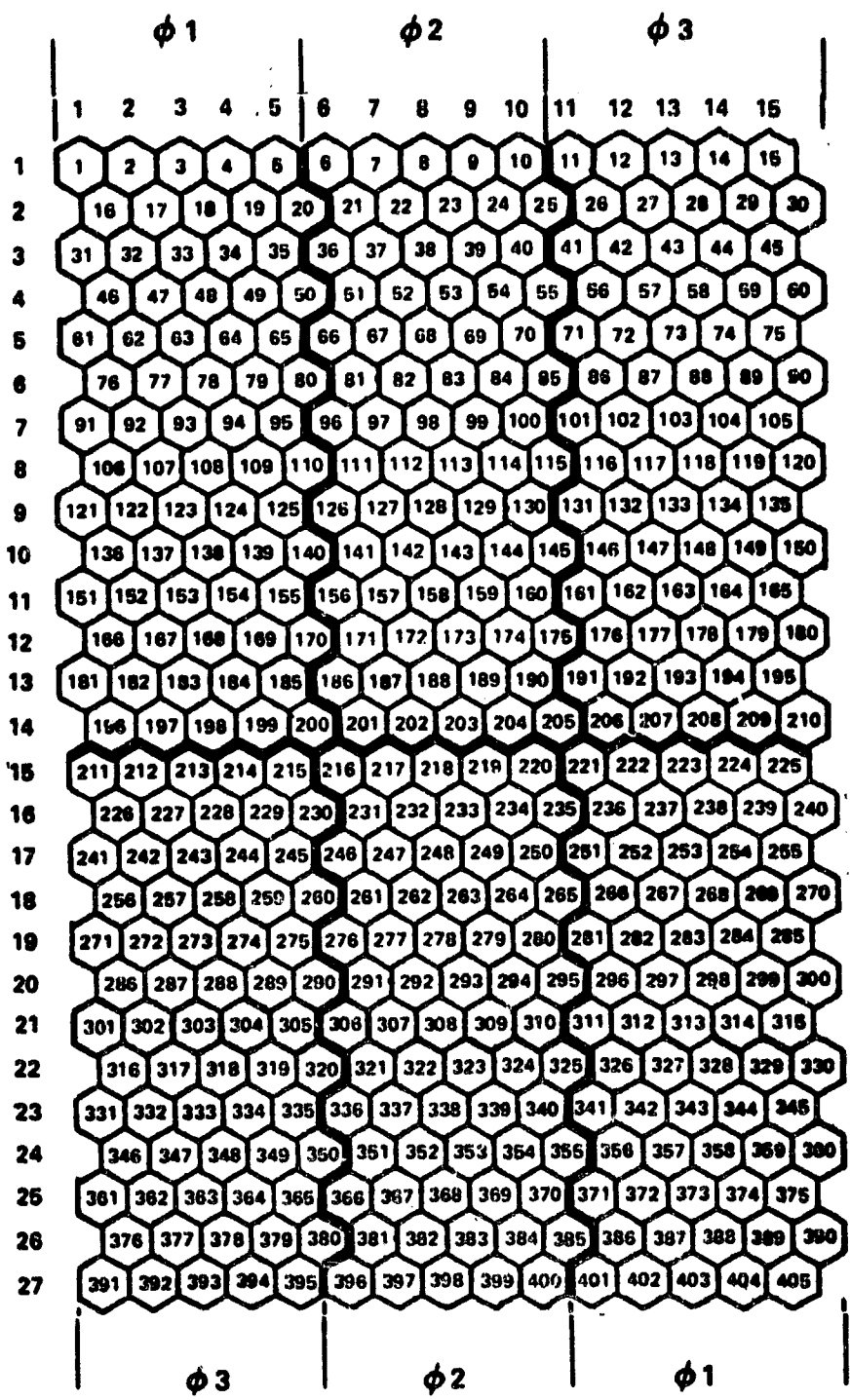


Figure 10. Grid network and electrical arrangement.

ORIGINAL PAGE IS  
OF POOR QUALITY

## B. Solar System Simulator Description

This simulation element includes the collector orientation positioning and solar system boundary condition simulation by the fluid loops, including transport media flowrate and temperature.

1. Orientation Simulation. Simulation of orientation is provided by a variable attitude tilt table to which the collector test item is mounted. The table provides a kinematic capability to set varying collector tilt angles and azimuth angles. Sun azimuth and control of incidence angle positions may be simulated using the tilt table along with an azimuth adjustment structure. The tilt table is capable of continuous adjustment of tilt angles from 0 to 72 deg from the horizontal. Azimuthal adjustments from 0 to 60 deg can be achieved by either rotating the entire tilt table or by use of a special azimuth adjustment structure mounted on the tilt table.

The table surface is 2.4 by 1.5 m (8 by 5 ft) in plan form. It consists of a 6061 aluminum angle structure to which a 142 by 244 cm (56 by 96 in.) sheet of 1.9 cm (0.75 in.) varnished plywood is bolted to form the collector mounting pad (Fig. 11).

### 2. Fluid/Thermal Loop Simulation.

a. Air Loop. This fluid/thermal simulation is provided by an open-air loop (Fig. 12). In this loop the transport media flowrate can be varied from 0 to 4.5 STD m<sup>3</sup>/min (0 to 160 STD cfm). Control within  $\pm 2$  percent of the desired flowrate, at steady state, can be achieved. Collector inlet air temperatures can be varied from near ambient to 93°C (200°F) and controlled to within  $\pm 0.6^\circ\text{C}$  ( $\pm 1^\circ\text{F}$ ).

The air load simulator is an open-flow loop drawing room air in and supplying it to the collector. The basic hardware in this loop consists of

1. A 1 1/2 hp, 115 V blower/motor combination
2. A 230 V proportional heater controller
3. Four 3.75 kW strip heaters

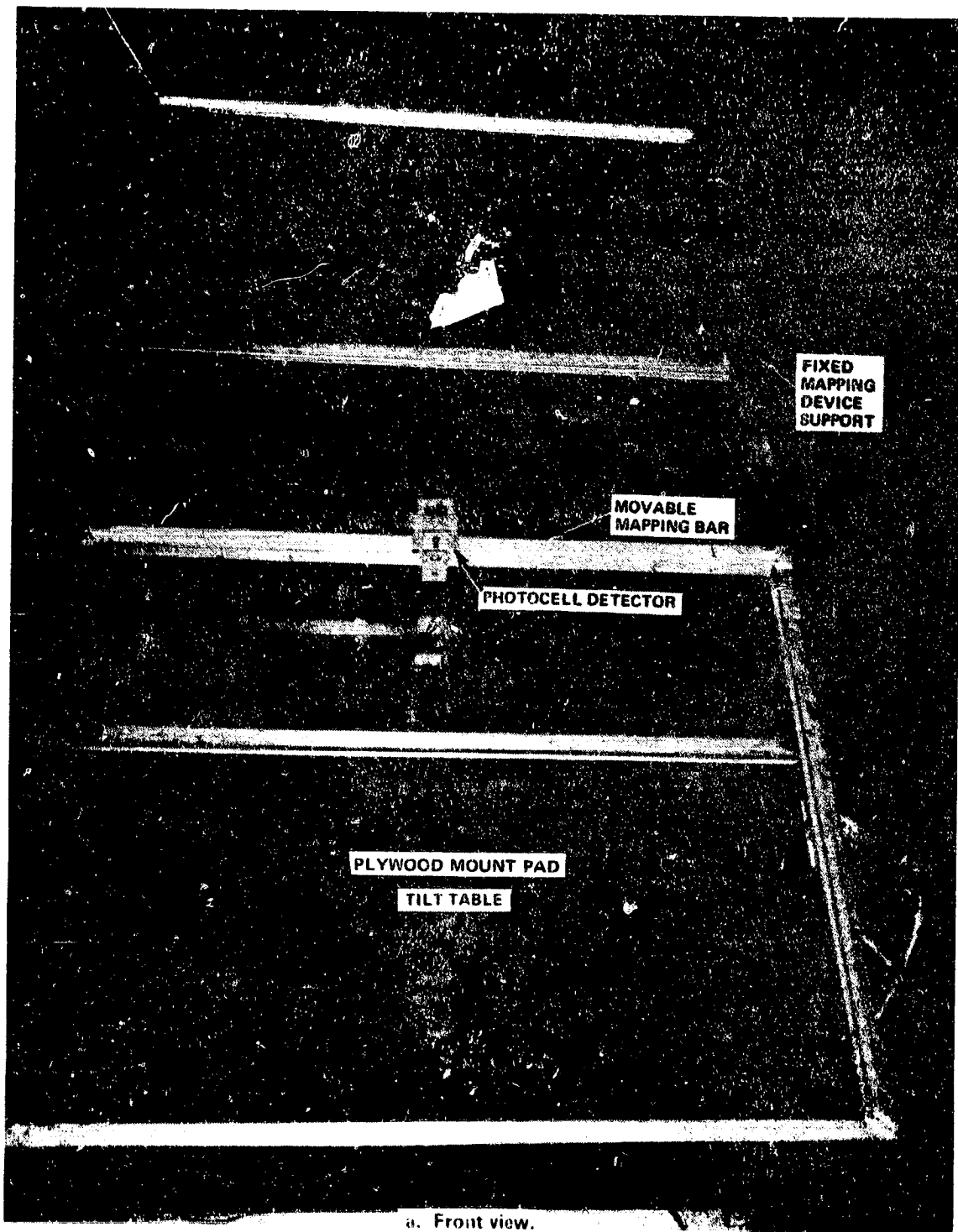


Figure 11. Tilt table with mapping rig.

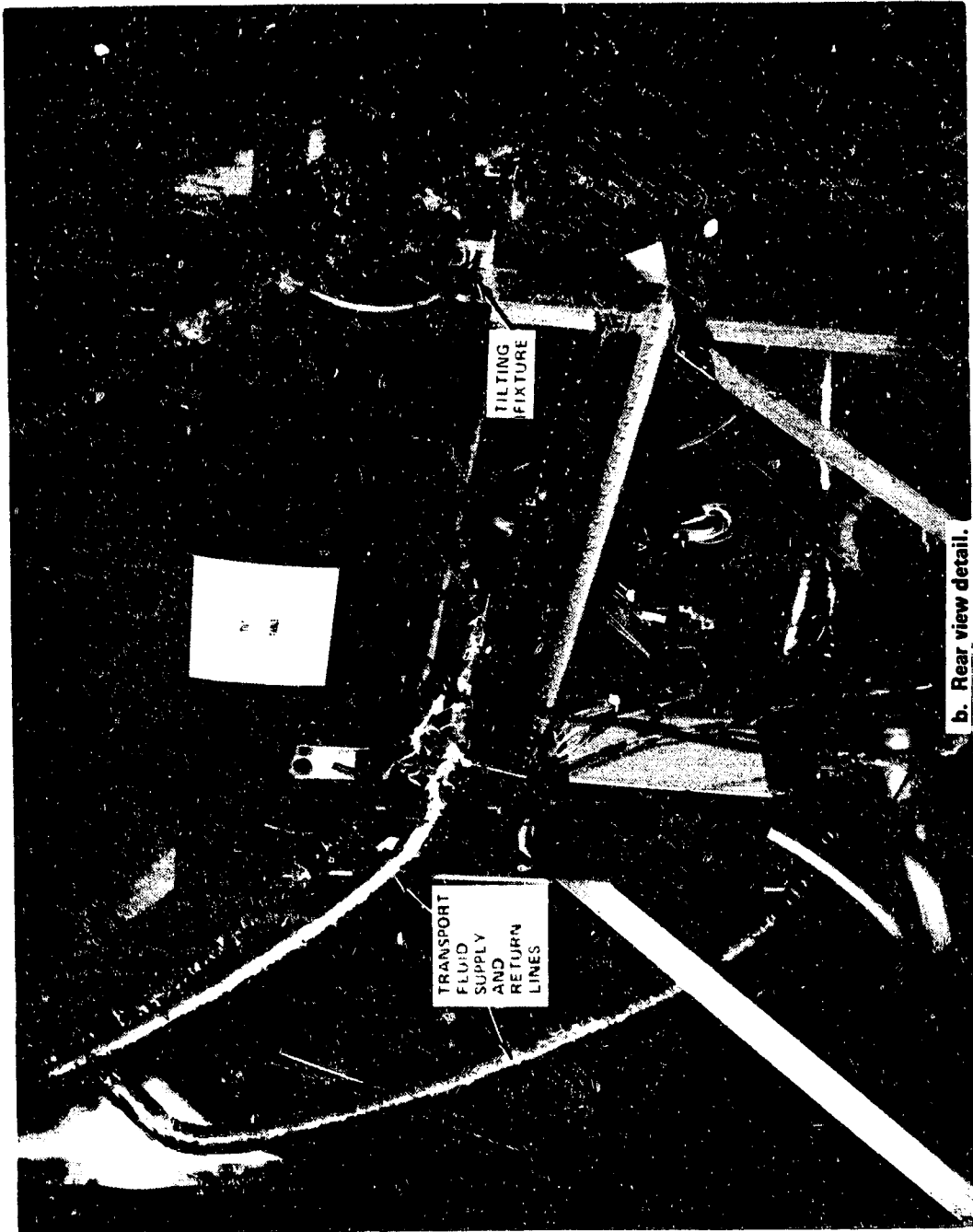


Figure 11. (Continued).

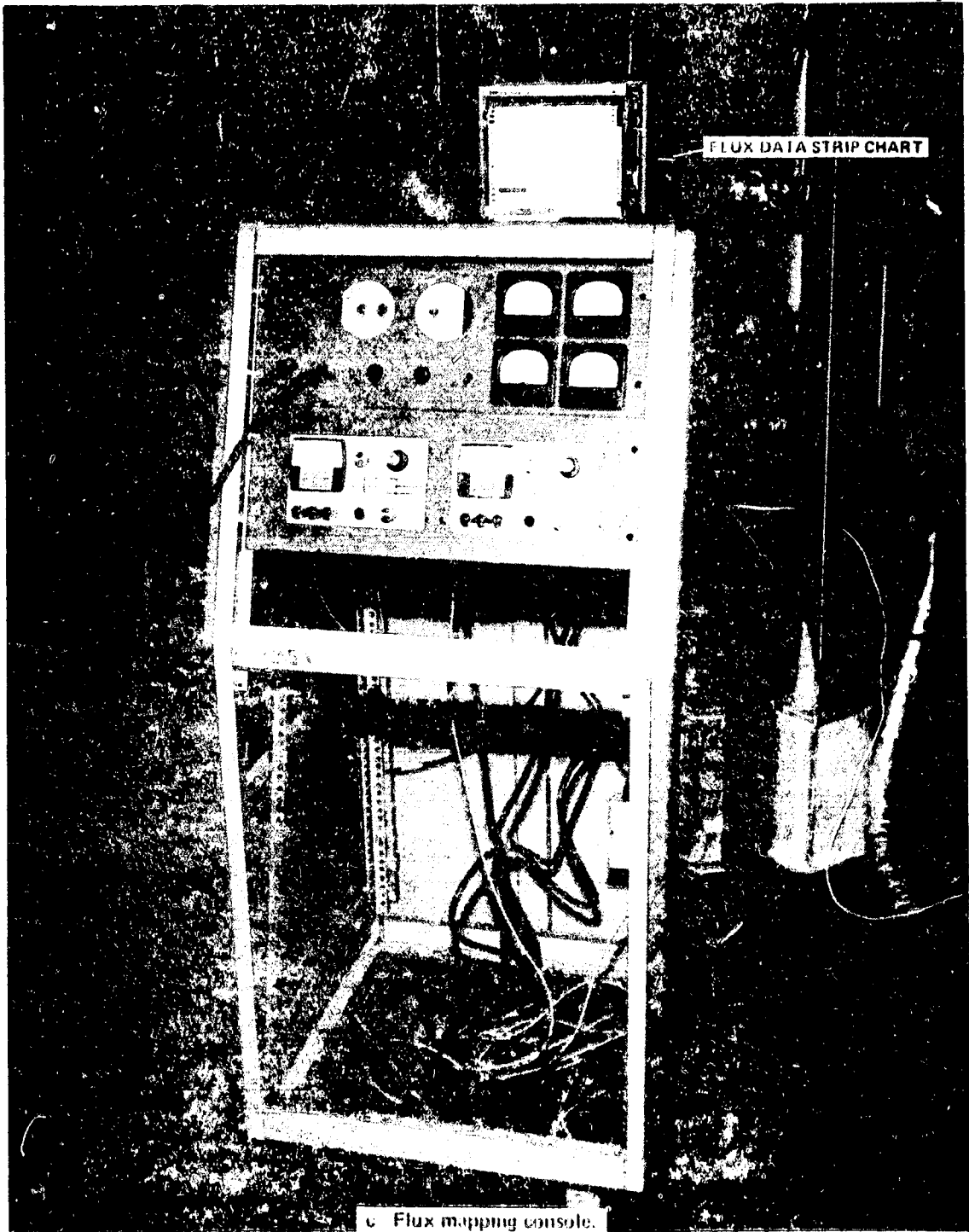
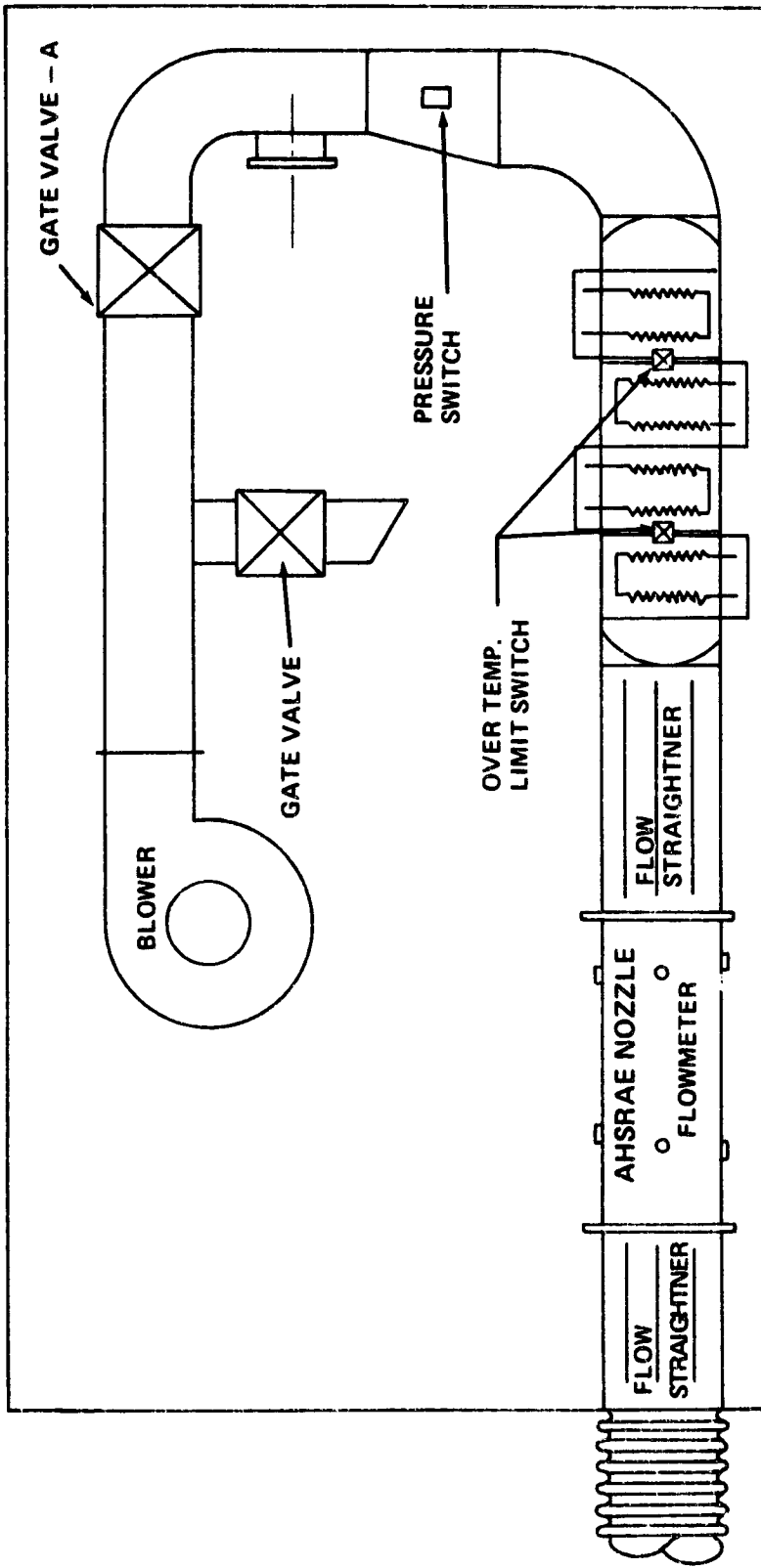


Figure 11. (Concluded).



4 HEATING ELEMENTS @ 3.75 KW 208 V

Figure 12. Air loop thermal simulator schematic.

4. ASHRAE standard nozzle and test section.
5. Two 20.34 cm (8 in.) gate valves.

Figure 13 depicts the arrangement of this hardware.

b. **Liquid Loop.** The liquid loop normally utilizes a 50 percent by volume (52.7 percent by weight) ethylene glycol (Prestone II)/water mixture with corrosion inhibitor. For this fluid, flowrates may be varied from 0.02 to 0.25 m<sup>3</sup>/h (6 to 67 gal/h) with  $\pm 2$  percent control of the flowrate at steady state. Inlet temperature control of 0.6°C ( $\pm 1^\circ$ F) can be achieved for these flowrates over a range of ambient plus 6°C ( $+10^\circ$ F) to 104°C (220°F) with the water/glycol mixture. Energy collection rates of up to 2632 W (9000 Btu/h) can be accepted while meeting these conditions. These conditions can be met while encountering fluid resistances up to 138 000 N/m<sup>2</sup> (20 psid). Most of the transport media used in solar systems may be used in this fluid loop with corresponding alterations in the thermal/fluid loop simulation capability. Hardware in this loop consists of:

1. A 110 V, 1/3 hp fluid pump
2. A 230 V proportional heater power controller
3. A 230 V, 18 kW submersion heater
4. A shell type single pass liquid/liquid heat exchanger
5. A fluid reservoir
6. A rotometer visual flowmeter
7. A valve controller
8. Miscellaneous hand valves.

Figure 14 is a schematic of the loop arrangement and Figure 15 is a photograph depicting the layout of hardware in this loop.





Figure 13. Air loop simulator arrangement.

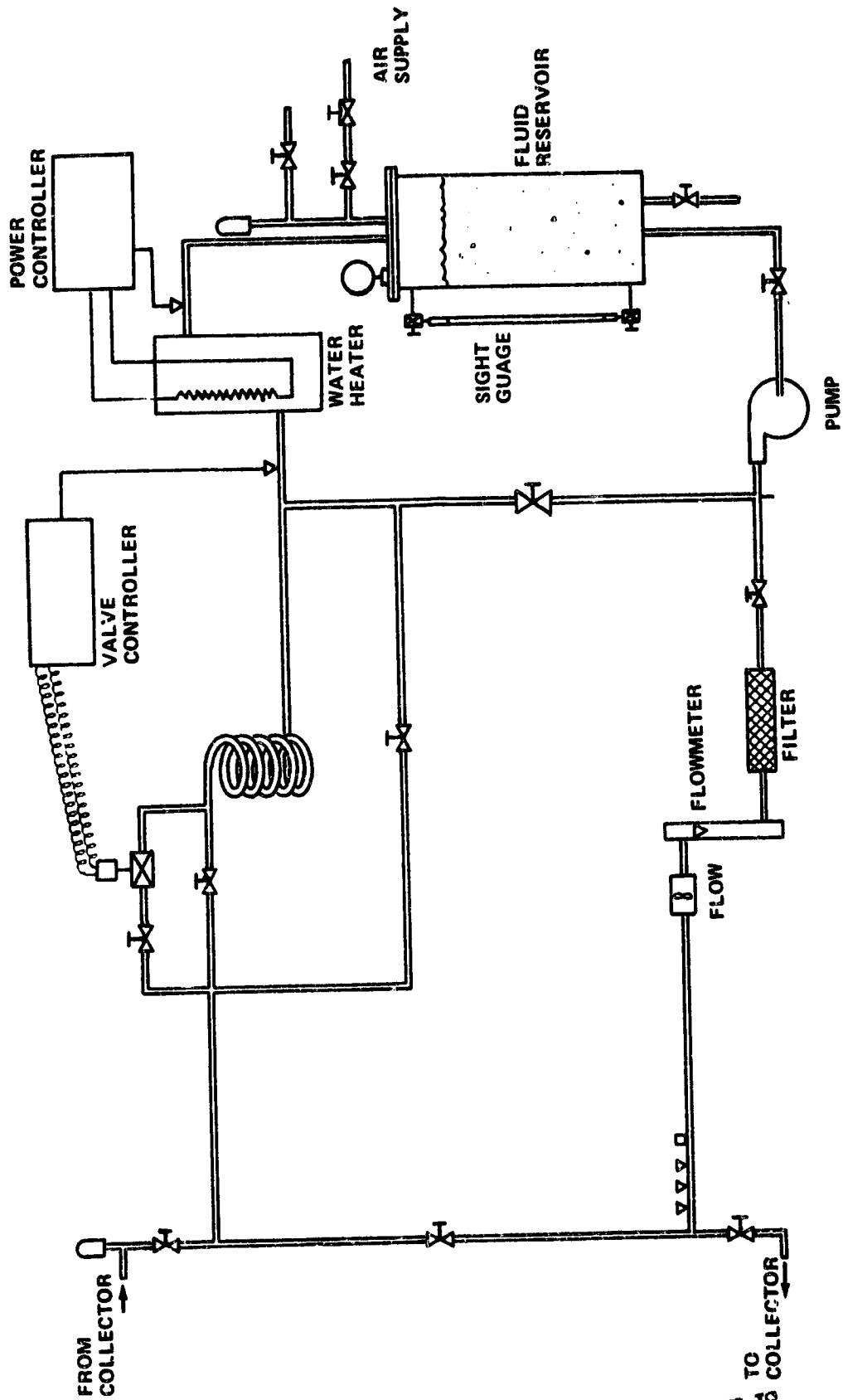


Figure. 14. Liquid loop simulator schematic.

ORIGINAL PAGE IS  
OF POOR QUALITY

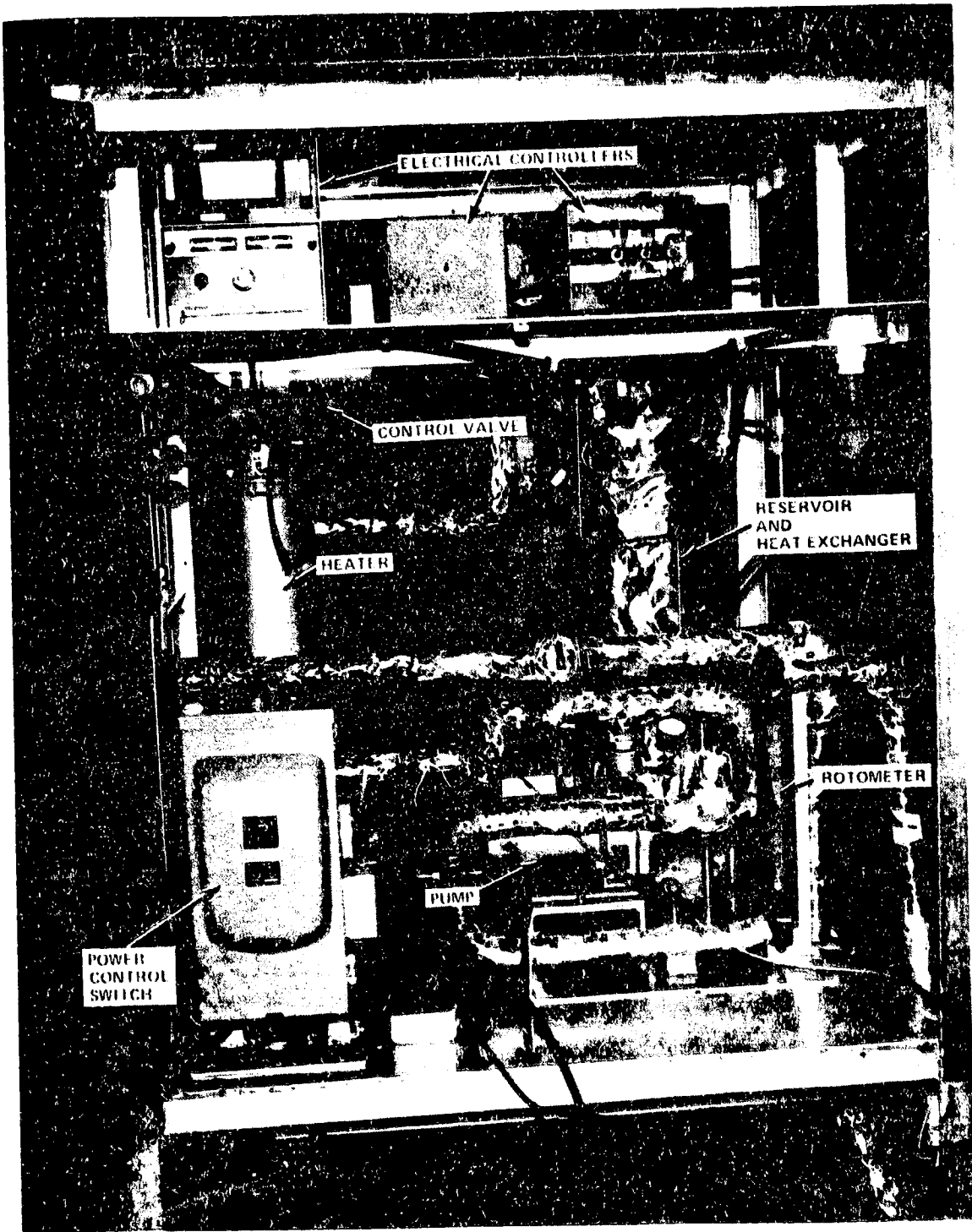


Figure 15. Liquid loop simulator arrangement.

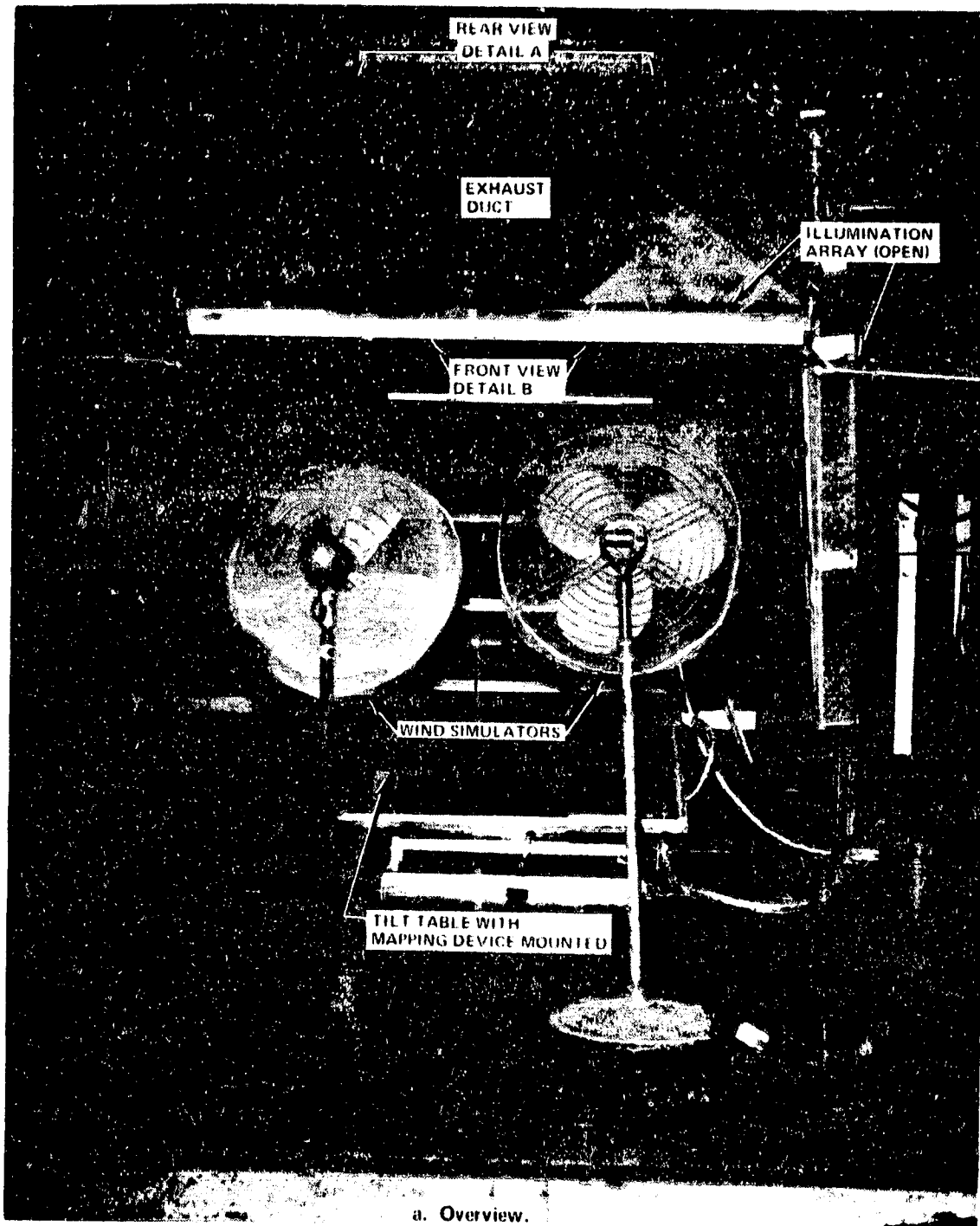
## C. Basic Facility

In addition to the previously discussed simulation capabilities of solar flux and attitude and fluid loop simulation, the basic facility also provides both external wind and Sun positional simulation capabilities. The Sun altitude position simulation is provided by the design of the floating illumination array mount. This floating arrangement allows varying the housing angle from horizontal to 72 deg above the horizontal. Control of this simulated solar altitude is achieved by manually adjusting a chain hoist attached to the illumination array. Since the flexible cooling air exhaust duct connected to the array has a limited travel, alternate duct position connections are provided. Three position connections are available to accommodate low, mid, and high solar altitude positions (Fig. 16).

Wind simulation is provided by two floor fans. The two 1/4 hp, 76 cm (30 in.) diameter blade fans are 168 and 160 cm (66 and 63 in.) high, respectively. The taller fan is three-bladed with a 1140 to 860 rpm range. The shorter fan is four-bladed with a 1140 to 790 rpm range. Velocities from 1.3 to 5.8 m/s (3 to 13 mph) can be achieved with the fans by moving the fans nearer and farther away from the tilt table mounted test item. Two fans are used to achieve better velocity uniformity across the test plane. Wind is normally directed into the collectors from the south, but mobility of the fan allows direction simulation from any angle.

All elements of the simulator, with exception of the control console (Fig. 17), are housed in a mild steel structure surplused from a previous test program. The structure is 8.5 m (28 ft) in height with a 4.3 m (14 ft) square plan form. The frame structure is covered on all sides except the south side with a blue plastic tarpaulin. A mobile glare shield is situated behind this open side and in front of a visitor viewing area to protect the eyes of passersby and limit spurious radiant energy inputs from other sources to the test item. This shield is constructed from angle iron structure and covered with the same tarpaulin material.

The entire simulator structure is housed in Building 4619. The simulator is located in the west end of the high bay portion of the building. This building is located near the corner of Rideout and Fowler Roads of MSFC (Fig. 18).



a. Overview.

Figure 16. Basic facility.

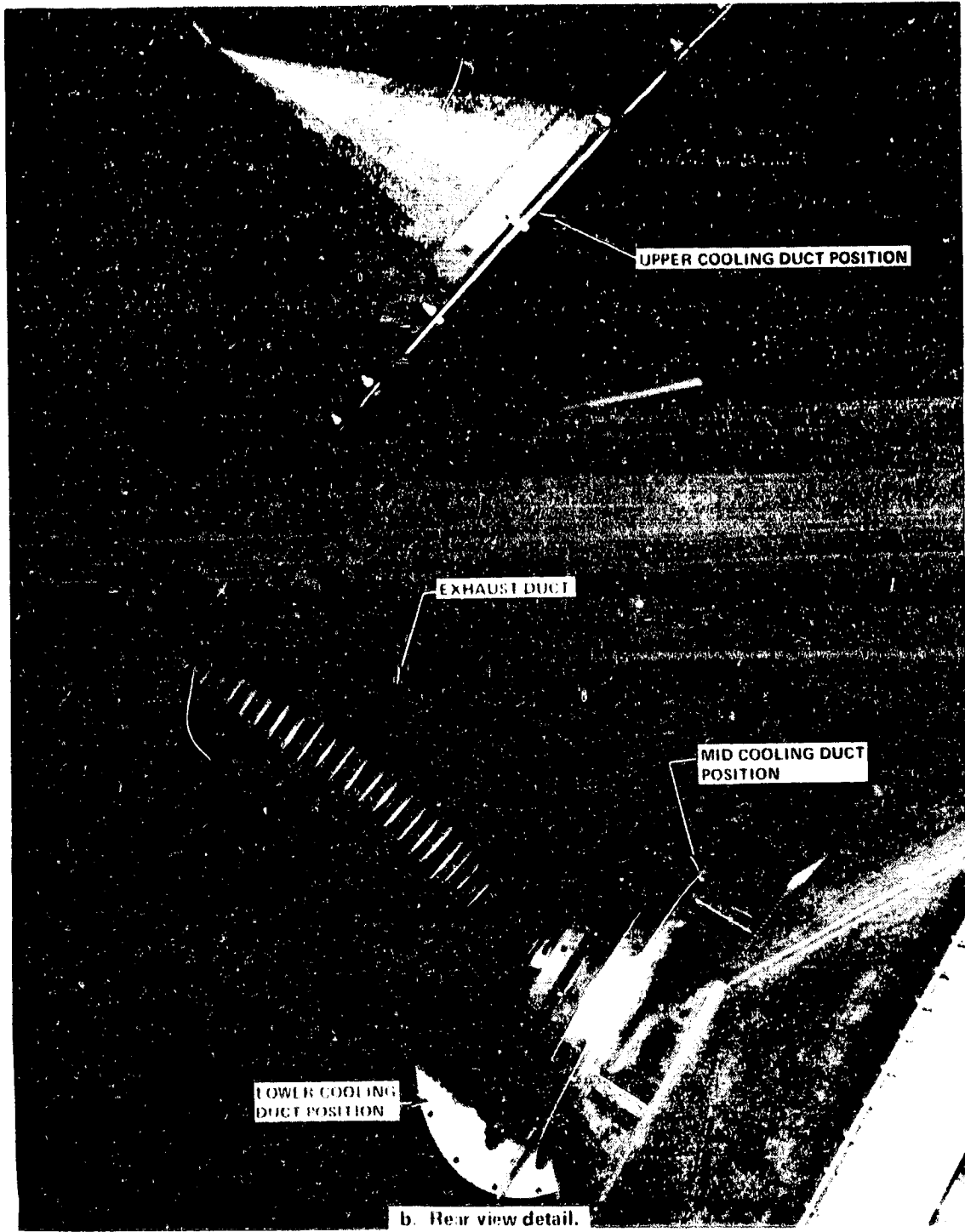
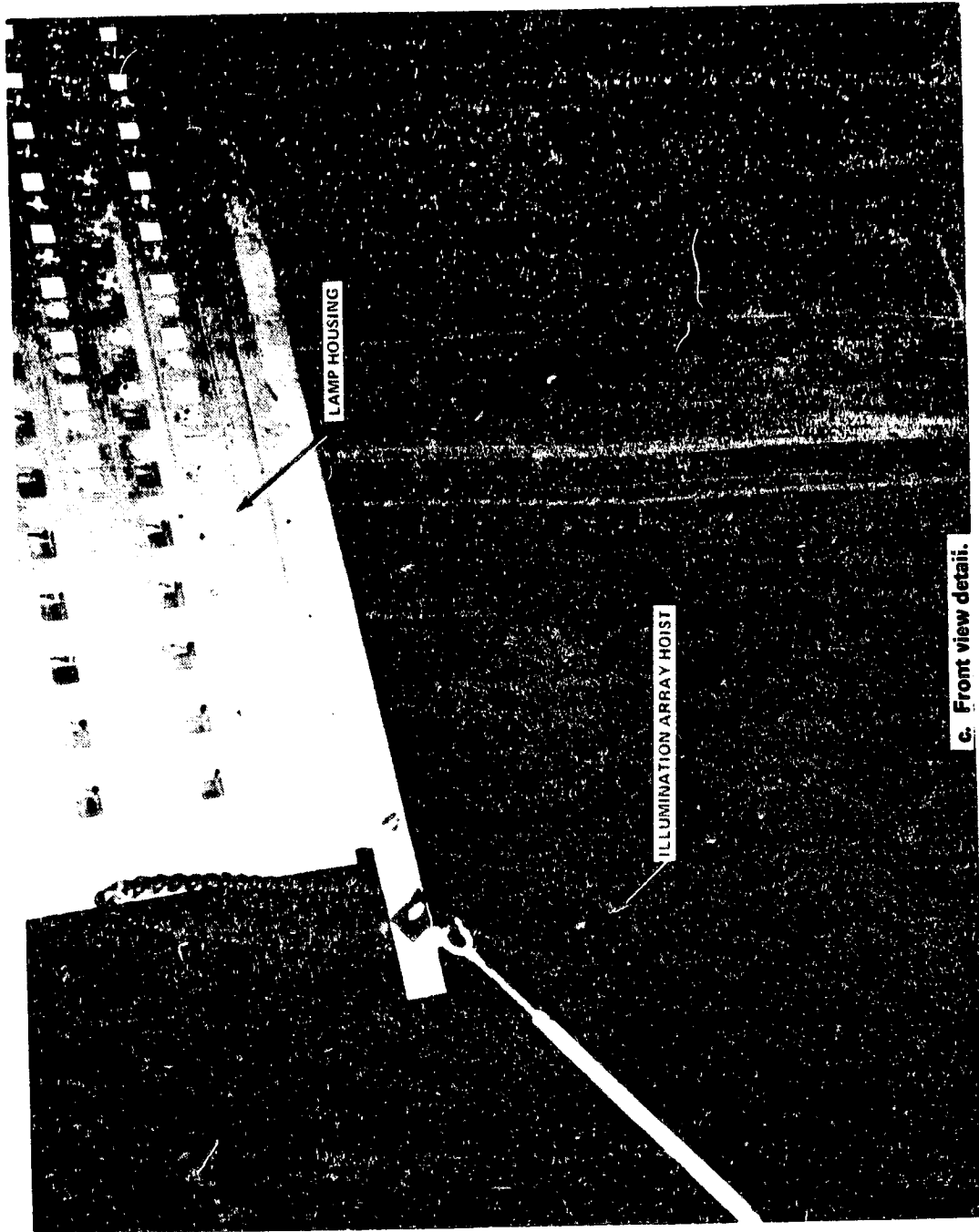


Figure 16. (Continued).



c. Front view detail.

Figure 16. (Concluded).

ORIGINAL PAGE IS  
OF POOR QUALITY



Figure 17. Overall view of simulator.



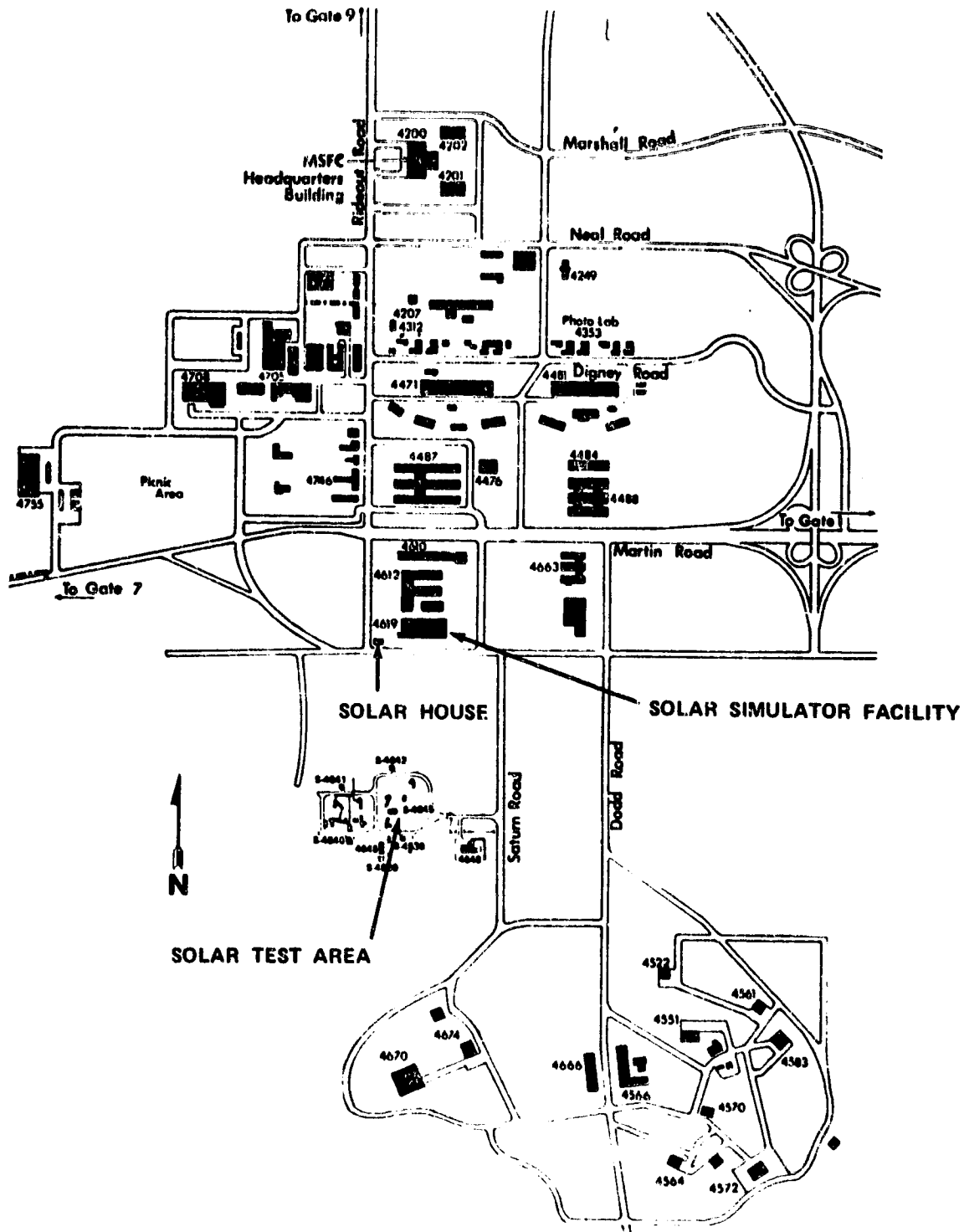


Figure 18. MSFC layout.

ORIGINAL PAGE IS  
OF POOR QUALITY.

## D. Instrumentation

The instrumentation/ data acquisition system available consists of 80 channels. Instrumentation for collector test items includes absolute and differential temperature measurements, flowrate measurements, absolute and differential pressure measurements, wind velocity, as well as total solar radiation measurements (diffuse and direct radiation measurements are not normally recorded but may be acquired for special tests). These measurements use a number of different type sensors depending on media, measurement type, and location of measurement. Appendix A details these measurements along with type and estimated accuracy of sensors. Overall measurement accuracies and minimum unit readout capabilities are given in Table 1.

TABLE 1. MEASUREMENT ACCURACY

Type	Media	Accuracy	Minimum Readout
Thermocouple	Liquid	$\pm 0.5^{\circ}\text{C}$ ( $\pm 0.9^{\circ}\text{F}$ )	$\pm 0.06^{\circ}\text{C}$ ( $\pm 0.1^{\circ}\text{F}$ )
Thermopile	Air	$\pm 0.06^{\circ}\text{C}$ ( $\pm 0.1^{\circ}\text{F}$ )	$\pm 0.4^{\circ}\text{C}$ ( $\pm 0.7^{\circ}\text{F}$ )
Resistance Thermometer	(Liquid and Air)	$\pm 0.3^{\circ}\text{C}$ ( $\pm 0.5^{\circ}\text{F}$ )	$\pm 0.006^{\circ}\text{C}$ ( $\pm 0.01^{\circ}\text{F}$ )
Solar Flux	N/A	$\pm 3\%$	
Flowrate	Liquid	$\pm 1\%$ of FS (1.2 gpm) ( $0.08 \text{ m}^3/\text{s}$ )	$\pm 0.00001 \text{ kg/s}$ ( $\pm 0.1 \text{ lb/h}$ )
	Air	$\pm 2\%$ of FS (210 cfm) ( $0.1 \text{ m}^3/\text{s}$ )	
Wind Velocity	Air	$\pm 3\%$ FS (30 mph) ( $13 \text{ m/s}$ )	N/A
Voltage	N/A	$\pm 0.5\%$ FS (0-500 V)	N/A

Facility peculiar instrumentation includes nine surface mounted thermocouples on simulator lens, a cooling air outlet temperature, six lamp bulb base temperature measurements, and the lamp array voltage output. Figure 19 depicts illumination array with details of lamp and lens instrumentation locations. A list of typical collector performance measurements are listed by name in Table 2.

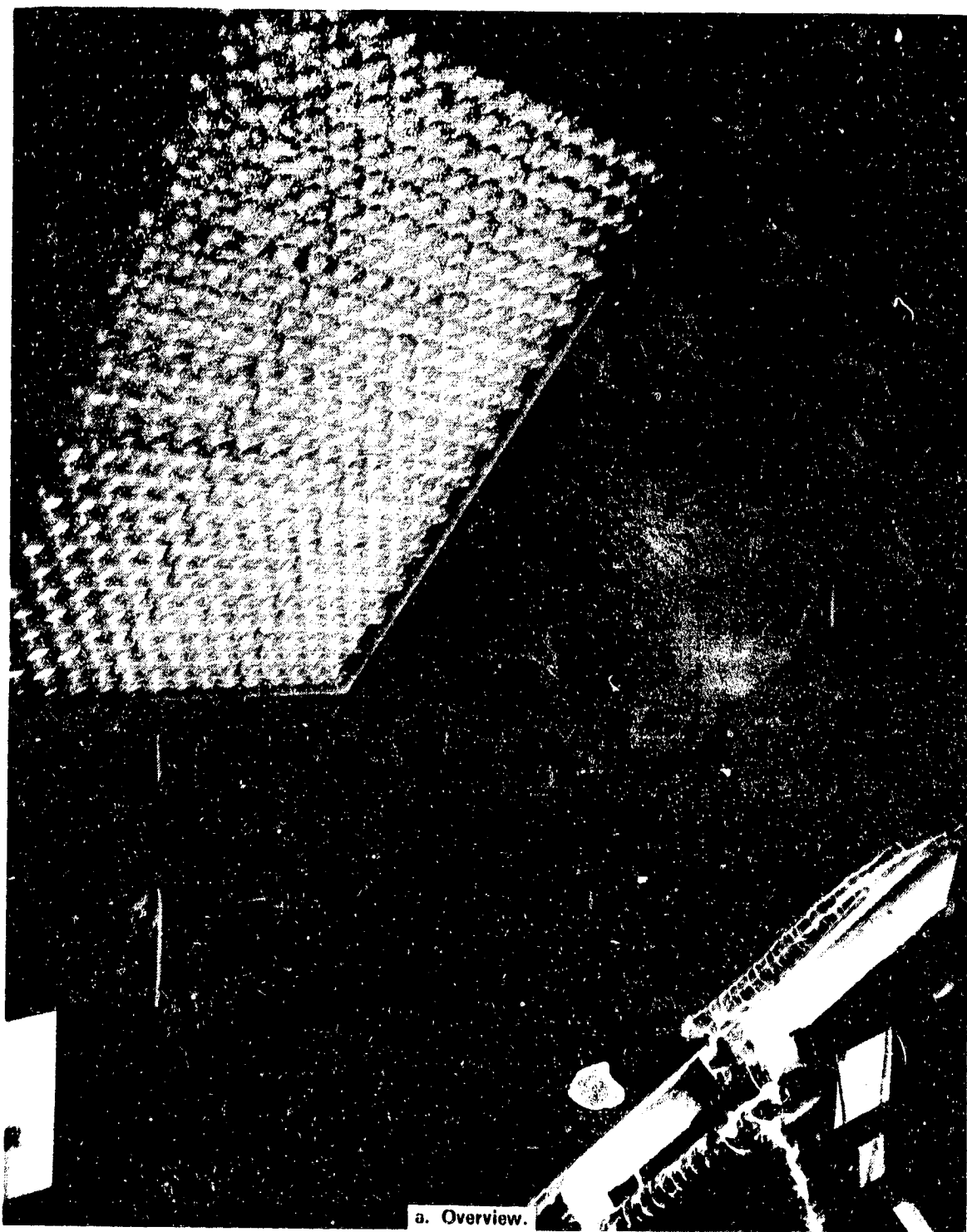
In addition to data recordings, before each test observations are made concerning each collector (Appendix B). These observation data include spectral property measurements, which in some cases cannot be made because of the adverse effect of collector disassembly on its subsequent testing or further use. For those collectors for which measurements can be made, five points on the cover and absorber (one in each corner and one in center) are used to acquire the average readings.

### III. SIMULATOR EVALUATION AND OPERATION

#### A. Sun Simulator Performance

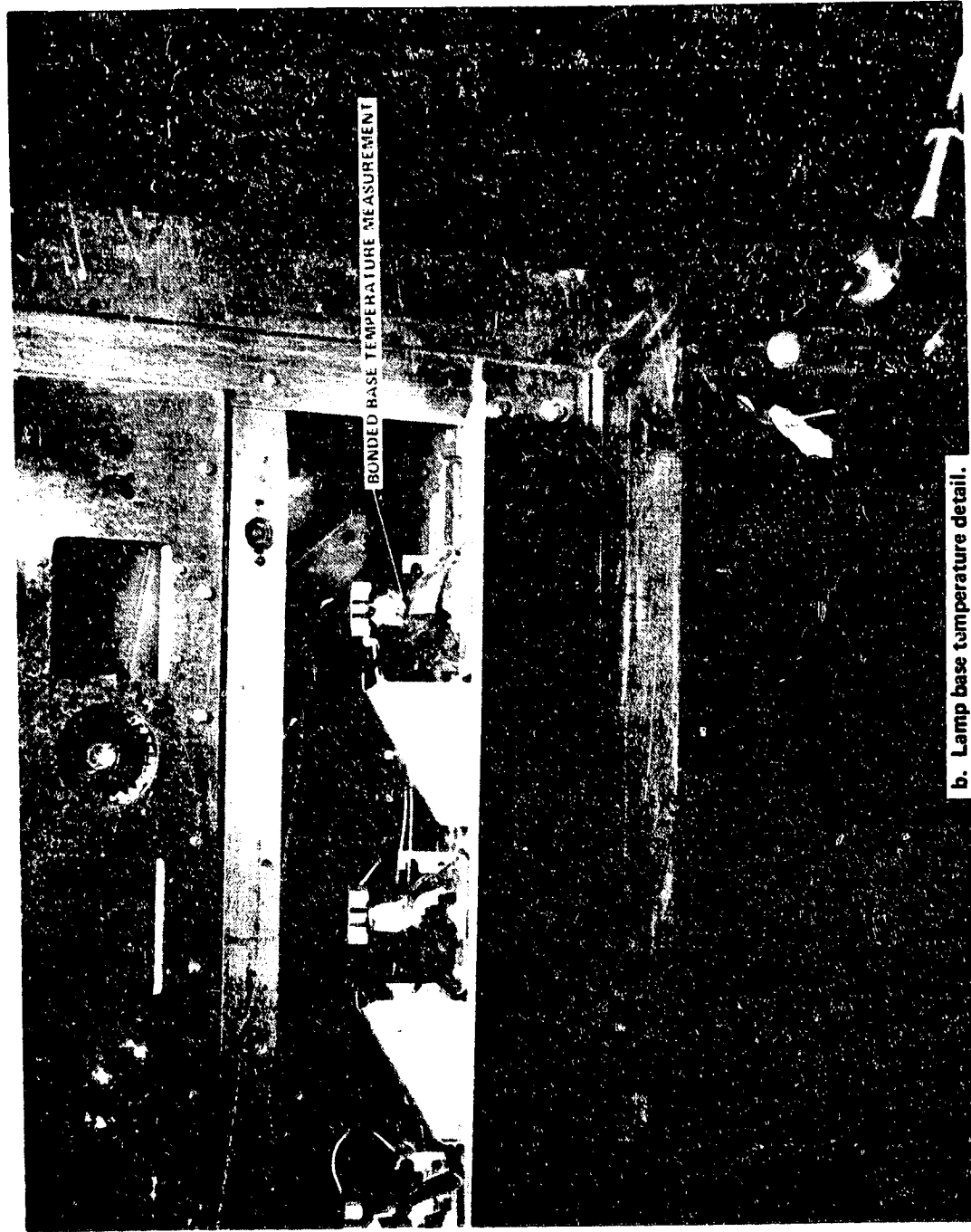
The capability of the Sun simulator to reproduce actual conditions has been determined. In particular, the parameters of interest are flux intensity variation capability, flux uniformity intensity on a plane surface, collimation of flux, and the capability to reproduce the solar energy spectrum. The initial target requirements are given in Reference 2.

The range of radiation intensity achievable by the facility is dependent on the facility configuration, as will be discussed later. During initial checkouts, it was found necessary to "build-in" a fixed attenuation of the intensity level because the flux level was found to be higher than desirable. As a result, an aluminum mesh wire (typical household window screen) with approximately 3 mm (0.13 in.) square grids (i. e., 8 × 8 mesh) was installed behind the lenses. A photograph of the screen is shown in Figure 20. The screen combined with the lenses attenuates approximately 40 percent of the radiation in the solar spectrum with the lens/screen configuration in place. The intensity can be varied from 395 W/m<sup>2</sup> (125 Btu/h-ft<sup>2</sup>) at 70 V to 962 W/m<sup>2</sup> (304 Btu/h-ft<sup>2</sup>) at 108 V. This is the average value of flux intensity as measured on a plane surface normal to the energy input and at a distance of 2.7 m (9 ft). The lower limit is dictated by the minimum continuous voltage at which the lamps can be operated without failure of the halogen cycle. The maximum is limited by the voltage



a. Overview.

Figure 19. Simulator test arrangement.



b. Lamp base temperature detail.

Figure 19. (Continued).

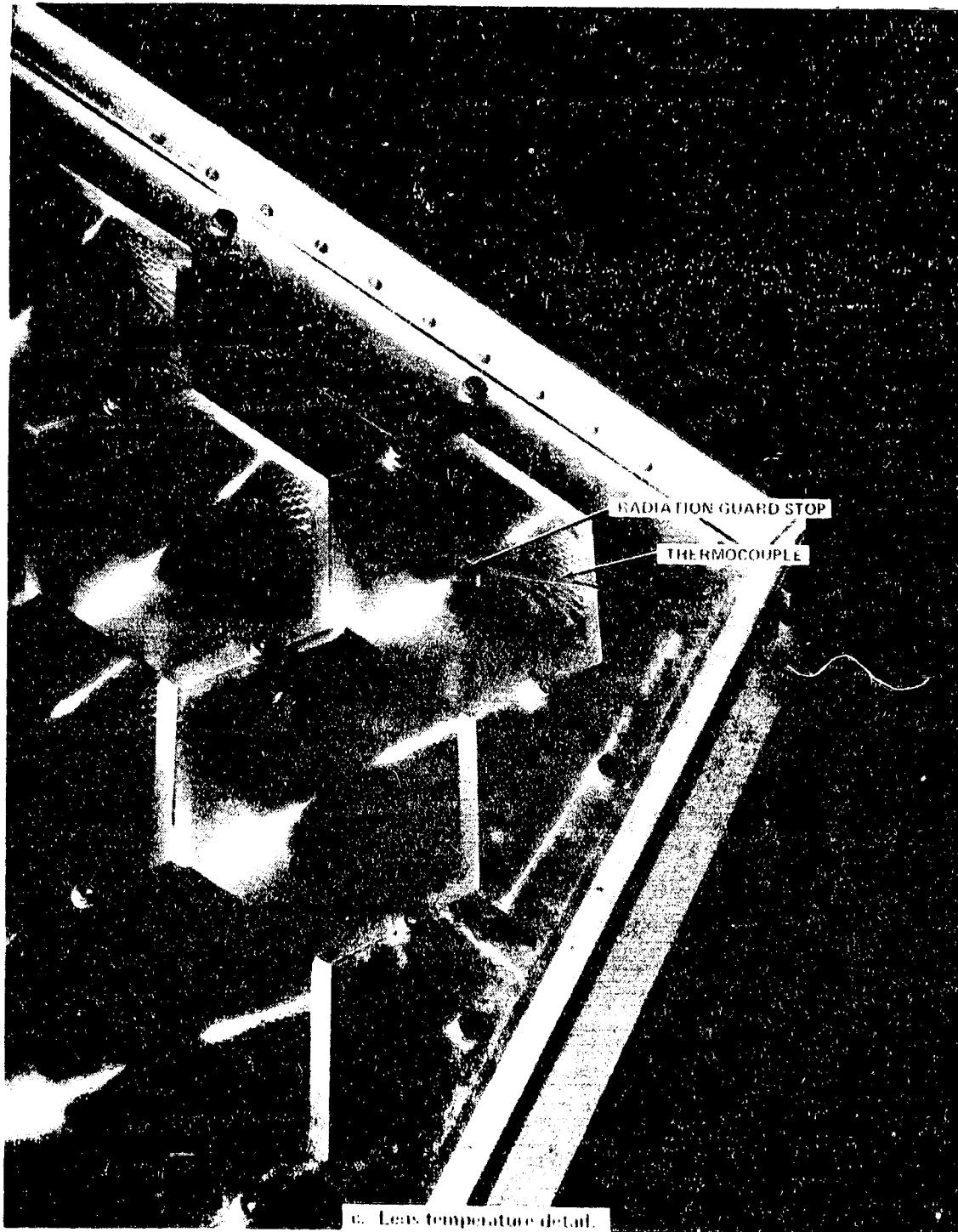


Figure 19. (Concluded).

ORIGINAL PAGE IS  
OF POOR QUALITY

TABLE 2. COLLECTOR PERFORMANCE MEASUREMENTS

Function
Absorber Surface Temperature, °C (°F)
Absorber Surface Temperature, °C (°F)
Absorber Surface Temperature, °C (°F)
Absorber Surface Temperature, °C (°F)
Absorber Surface Temperature, °C (°F)
Convactor Tube Surface Temperature, °C (°F)
Convactor Tube Surface Temperature, °C (°F)
Convactor Tube Surface Temperature, °C (°F)
Convactor Tube Surface Temperature, °C (°F)
Convactor Tube Surface Temperature, °C (°F)
Convactor Tube Surface Temperature, °C (°F)
Absorber Surface Temperature, °C (°F)
Absorber Surface Temperature, °C (°F)
Absorber Surface Temperature, °C (°F)
Absorber Surface Temperature, °C (°F)
Absorber Surface Temperature, °C (°F)
Absorber Surface Temperature, °C (°F)
Absorber Surface Temperature, °C (°F)
Absorber Surface Temperature, °C (°F)
Absorber Surface Temperature, °C (°F)
Absorber Surface Temperature, °C (°F)
Convactor Tube Surface Temperature, °C (°F)
Convactor Tube Surface Temperature, °C (°F)
Absorber Surface Temperature, °C (°F)
Ambient Temperature, °C (°F)
Insolation Rate, W/m <sup>2</sup> (Btu/ft <sup>2</sup> -h)
Flowrate, kg/s (lb/h)
Collector Inlet Temperature, °C (°F)
Collector Outlet Temperature, °C (°F)

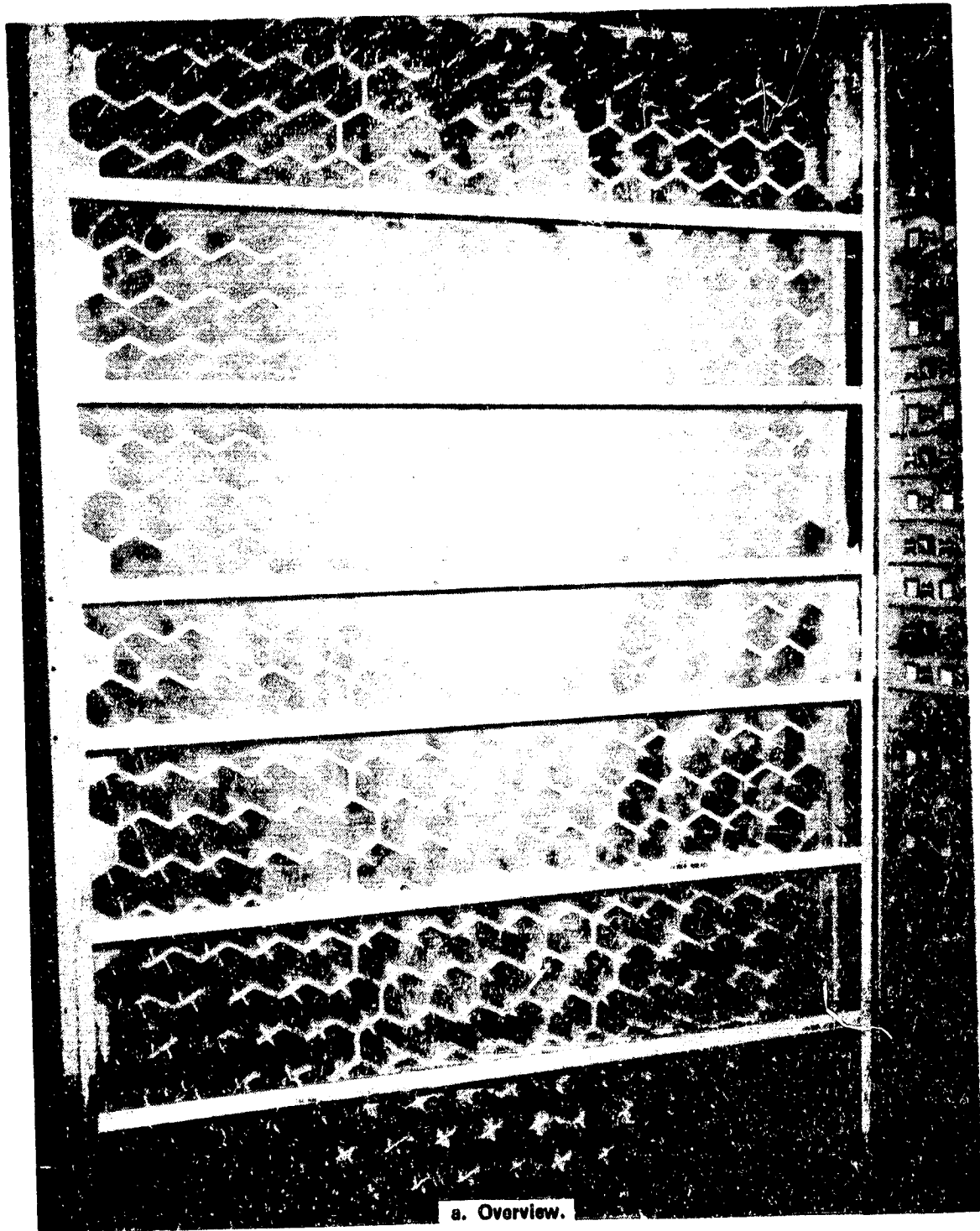
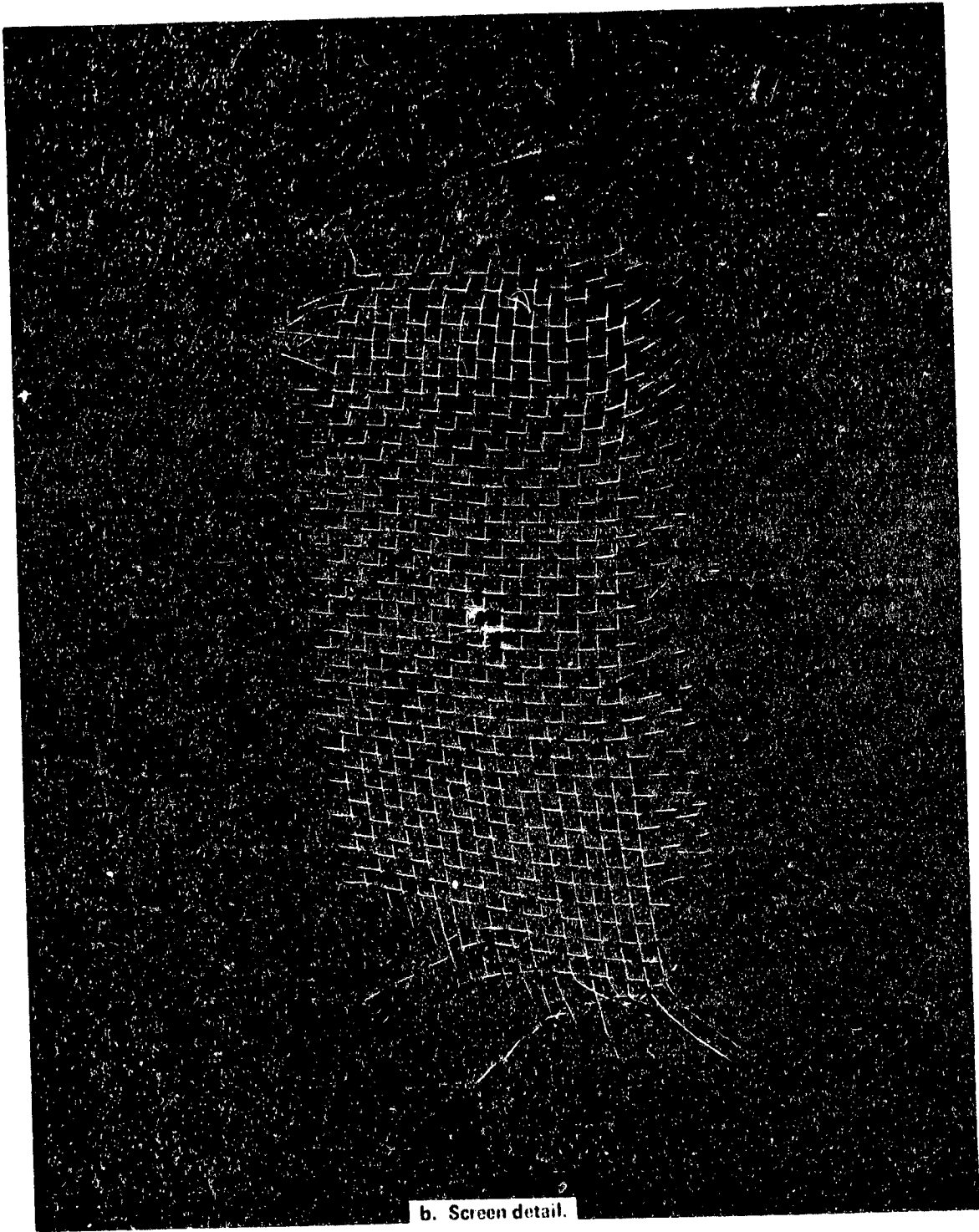


Figure 20. Lens housing and attenuation screen installation.

ORIGINAL PAGE IS  
OF POOR QUALITY





b. Screen detail.

Figure 20. (Concluded).

output capability of the controller. Higher intensity levels can be achieved, however, by either removing the attenuation screen, lowering the collimation lens, or both.

The maximum intensity nonuniformity that was initially targeted was  $\pm 7$  percent peak-to-peak based on original Lewis Research Center simulator specifications. However, measurements proved this value for the simulator to be  $\pm 10$  percent (Fig. 21). It should be noted that due to the nonuniformity being less pronounced in the center, this value is improved when testing collectors smaller than the tilt table. Using all data points a  $\pm 4$  percent RMS average resulted. These values were determined using a network of grid measurements across the tilt table. These grids were spaced at 15 cm (6 in.) intervals over its width. This resulted in a 551 point flux measurement matrix.

A simple photocell was used to determine the relative flux intensity continuously across this grid network. This data stream is transmitted to a plotter (Fig. 11). The average flux intensity position is then found using these data. This is done by either inputting this information into an 1108 computer, which automatically computes the average value, or by removing data from the flux plot and using simple manual calculation techniques. The radiation intensity is then measured at this average point by using an Epply PSP pyronometer.

All measurements are made at a 2.7 m (9 ft) distance from the test plane. Although this gives good uniformity, very little uniformity degradation occurs up to 3.7 m (12 ft) [3,4].

Flux collimation is important to assure proper uniformity and high fidelity reproduction of direct sunlight and shadowing characteristics of nature. Collimation of flux is defined for the lamp/lens combination as the angle which subtends a circle containing 95 percent of the energy incident on a flat plane. The value initially targeted for was 10 deg, but measurements indicate the actual value to be approximately 18 deg (Fig. 22).

Solar spectrum reproduction is of importance, especially for wavelength sensitive elements such as selectively coated collectors. Lewis Research Center has previously measured these values for the same lamp but a different lens [1]. However, since the same lamp and a similar lens is used in this installation, the spectral output of the combination should be very similar (Fig. 23). These data show extremely good reproduction of the spectrum by these lamps at air mass 2.

During these tests, the direct component of solar radiation striking the tilt table was found to be 88 percent of the total irradiation.

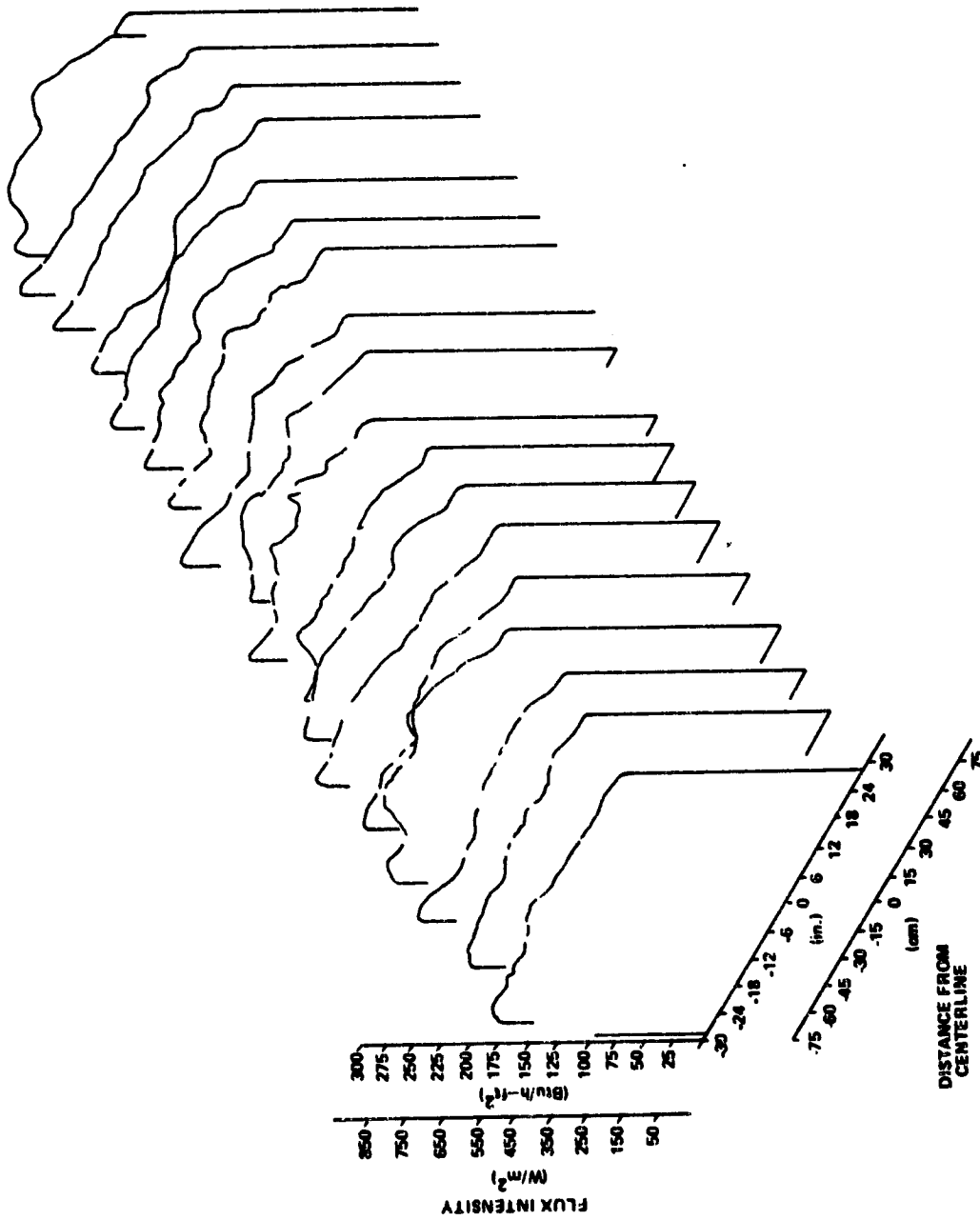


Figure 21. Typical solar flux map.

ORIGINAL PAGE IS  
OF POOR QUALITY

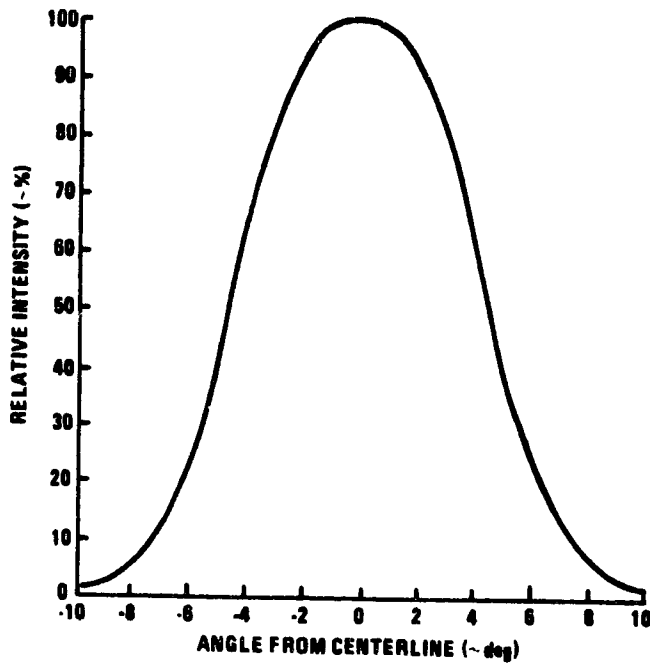
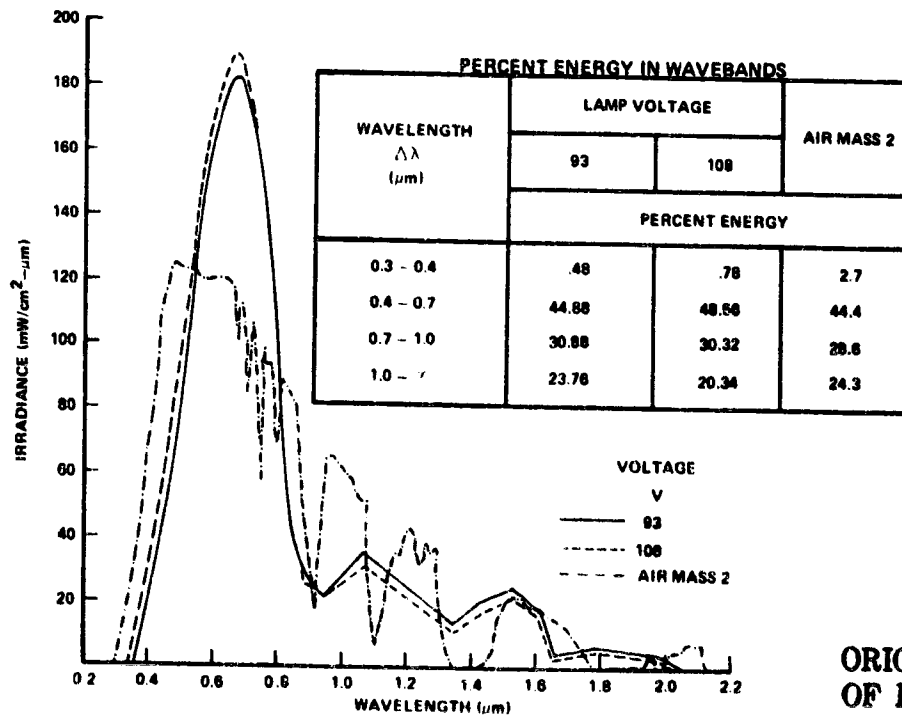


Figure 22. Plot of relative intensity versus angle.



ORIGINAL PAGE IS  
OF POOR QUALITY

Figure 23. Variation of lamp/lens spectral irradiance with wavelength.

## B. Anomalies

A number of anomalous conditions and unexpected problems were discovered during initial simulator checkout testing that affected overall performance. These include:

1. Higher flux intensity at normal operating voltages than desired
2. Out of tolerance peak-to-peak nonuniformity
3. Collimation angle too large
4. Blinking lamps.

The high flux intensity discovered initially was reduced by a flux attenuation device as previously described. It was also discovered that voltage to the lamps was slightly lower than faulty measurements had indicated so that minimum operating voltages had not been achieved as planned. After correction of this discrepancy and inclusion of the attenuation screen, the flux intensity level was brought into an acceptable range.

Out of tolerance nonuniformity was found to be caused by a combination of factors. These factors include:

1. Improper positioning of test plane away from illumination array
2. Variation of flux output from lamp-to-lamp
3. Lens warpage
4. Interphase voltage nonuniformity
5. Array warpage.

As discussed earlier the best uniformity is achieved at a distance of 2.7 m (9 ft). This fact, once discovered, allowed instant uniformity improvement by simply moving the test surface closer to the illumination array. Since that time, this distance has been held constant.

Nonuniformity due to variation in lamp output, which was found to be as large as 30 percent between any two lamps, was initially minimized by running individual lamp intensity versus voltage checks. These data were used for subsequent placement of lamps in the array for best overall uniformity. However, even with this selective placement of lamps, significant uniformity variations still existed. Further tests showed that reversing the lamp plug-in orientation caused significant variation in lamp output. Due to this uncertainty, and the time consuming nature of individual lamp checks, a simpler technique was adopted. In this new technique, the entire array output is mapped initially with new lamps in random locations. The judicious relocation of these lamps using these mapping data, combined with a subsequent remap and a second repositioning of lamps, has been found to produce uniformity at least as good as the more sophisticated time consuming technique of individual lamp checks.

During initial testing, Fresnel lens warpage was visible. This warpage was initially very severe because of the high intensity of radiation impinging on the lens caused by the previously discussed anomalies. These high levels caused lens temperatures to exceed the 65°C (150°F) upper temperature limit of the material deformation. However, after reducing the intensity to the desired level, warpage was still observed after a period of time, but to a lesser extent. The warpage appeared to be more severe in the center of the array. Measurement of lens temperatures in this zone indicated a range from 45 to 54°C (113 to 129°F) at an imposed flux intensity of 917 W/m<sup>2</sup> (290 Btu/h-ft<sup>2</sup>) and 41 to 51°C (105 to 124°F) at 190 W/m<sup>2</sup> (250 Btu/h-ft<sup>2</sup>). These values were well below the maximum acceptable temperature limit, indicating warpage occurs at a level below the manufacturer quoted limit and is a cumulative function of time. An effort is currently underway to investigate a new lens material more resistive to thermal warpage.

All the previously mentioned discrepancies contribute to nonuniformity. An examination of the data indicate 70 to 80 percent of the nonuniformity now existing is due to lamp-to-lamp variations, 5 to 10 percent is due to lens warpage, and only a very small portion is a result of array warpage and interphase voltage nonuniformity. Since the total effect of these nonuniformities does not appear to significantly affect the fidelity of flat plate collector performance evaluation (as will be discussed later), further improvements in uniformity were not considered necessary.

ORIGINAL PAGE IS  
OF POOR QUALITY

During startup tests, it was discovered that a blinking or stroboscopic effect existed in the illumination from the array. This blinking could be seen by the naked eye and was detected by flux sensors as a significant oscillation in intensity. This was found to be the result of using a digital component in the phase firing controller. This component forced the control output to periodically eliminate an entire cycle to achieve the desired RMS voltage. Replacement of this component with an antilog type device eliminated the problem. The new antilog component controls RMS voltage by eliminating only a portion of each phase rather than entire cycles (Fig. 24). This technique gives a high frequency cutoff control which is not detectable by either the eye or the flux sensor.

As noted earlier, the collimation angle was found to be 18 deg rather than the 10 deg value targeted. This is due to the short focal length of the lens and the resulting close spacing between lens/lamp pairs. As a result of later performance test comparisons, this larger collimation angle was found to be not sufficiently detrimental to collector performance evaluation to warrant further attention.

Finally, variations between delivery voltage to lamp banks on each of the voltage phases was noted. This interphase voltage variation resulted in a small difference in the uniformity across the test plane and was not pursued further.

### C. Lamp Life Tests

Due to the significant impact of lamp life on facility operating cost, the need for long lamp life is apparent. As a result, a lamp life test was conducted in the simulator to determine expected life of lamps at a low voltage power setting. Also, the lamp startup procedure was specified to avoid fast voltage transients on the lamps which might reduce life.

In the life test, the earliest lamps failed at 105 h (without cycling) at 85 V or approximately  $133 \text{ W/m}^2$  ( $200 \text{ Btu/h-ft}^2$ ). These data indicated lamps may be run for extended periods at levels below the 90 V minimum recommended by the lamp manufacturer without significant failures occurring. These tests were run on a cluster of 5 adjacent lamps with array cooling set to give a lamp base temperature of  $288^\circ\text{C}$  ( $550^\circ\text{F}$ ). The simulator was tilted at 45 deg during all testing.

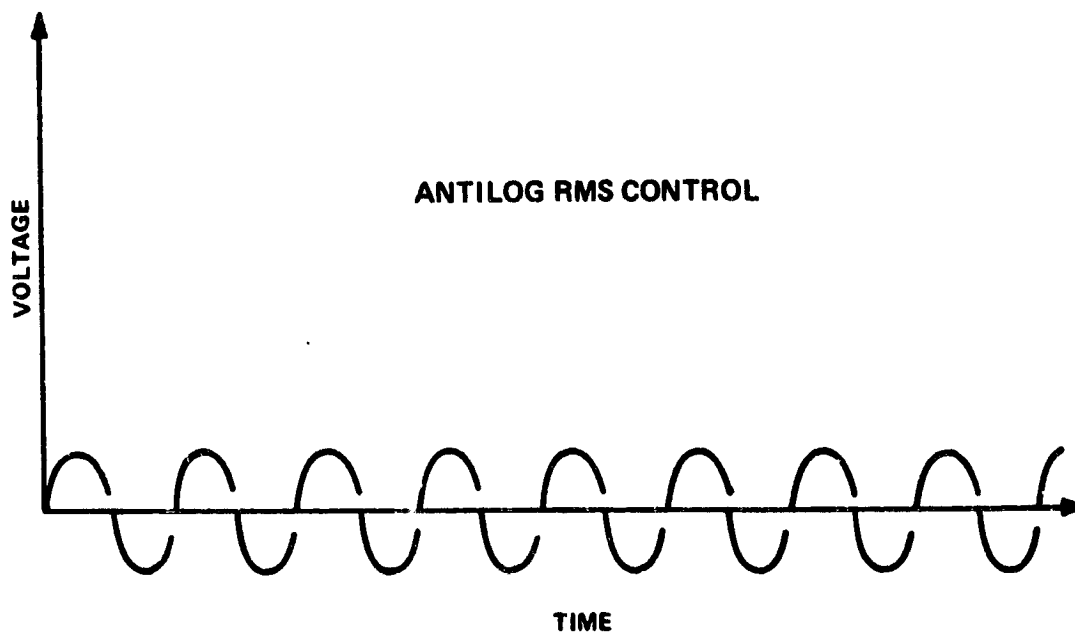
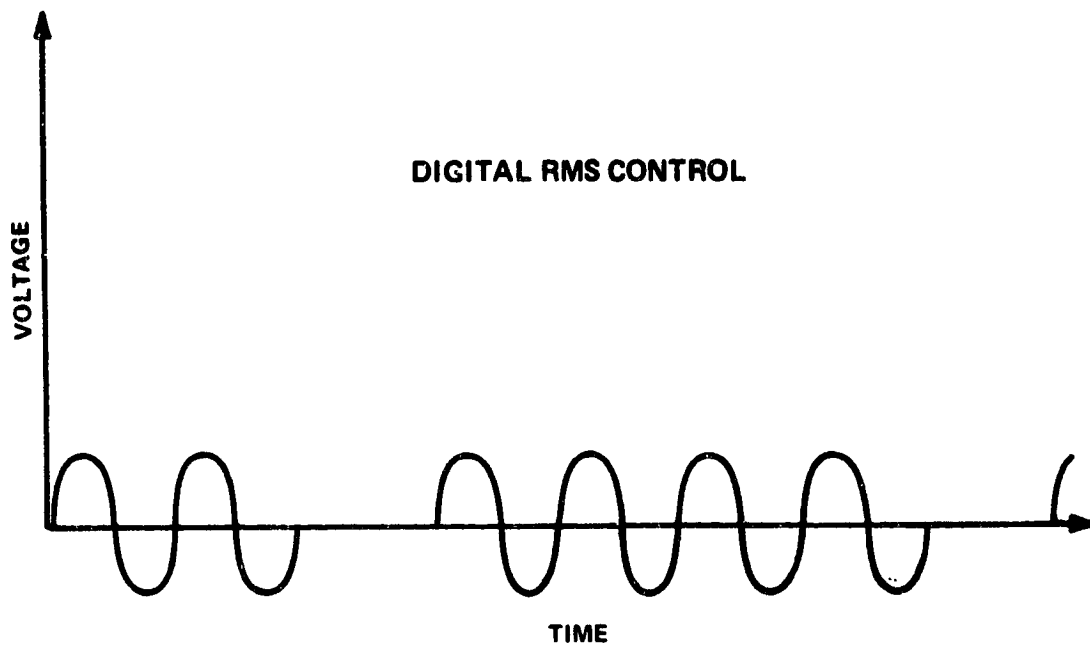


Figure 24. Lamp voltage control scheme.

ORIGINAL PAGE IS  
OF POOR QUALITY



Lamp failures can occur in a number of ways. Failures occurring at low voltage and/or high cooling air flowrates typically exhibit black speckling of tungsten on the bulb. This is a result of the halogen cycle not performing well enough to return sublimated tungsten to the filament; consequently, tungsten collects on the cooler surface of the bulb. Once started, speckling rapidly becomes severe enough to degrade lamp performance significantly. In opposition, the primary degradation of lamps at high voltage and/or low cooling air flowrates is filament burnout. If sufficient cooling is not provided to the lamp base or lamp voltages significantly higher than the rated value are used, premature filament burnout may occur. Marginal undercooling may also cause reflector cracking and/or dichroic reflector coating degradation.

Operation of the simulator at typical voltages of 93 and 103 V has resulted in lamp life from 60 to in excess of 80 h. At 60 h failures are infrequent; however with the passage of time failures become more frequent. After approximately 80 h of operation, the probability of failure increases rapidly. Assessment of lamp life is a very tenuous task, depending on the startup technique used, number of cycles, history of the voltage levels imposed on the lamp, cooling level, and lamp orientation. As a result, the minimum lamp voltage is limited to 80 V, whereas the maximum voltage is 108 V where cooling air flow is sufficient to avoid undercooling.

The procedure used in the facility to maximize lamp life is to replace failed lamps during a test only when more than five lamps have failed. If more than five fail before 80 h, the simulator is shut down and lamps replaced as required to avoid over five lamps being out at a time. At 80 h, all old lamps are replaced at one time as a standard facility maintenance item.

As noted, the rate at which voltage is applied to the lamp also has been found to have a significant effect on lamp life. This is especially important since the simulator duty cycle requires many start-stop cycles. For this reason, a rheostat is used in place of an on-off switch for lamp activation. This allows the operator to slowly increase the voltage input to the lamp. This technique significantly lengthens lamp life by applying the voltage slowly rather than instantaneously to the lamp filament.

#### D. Flux Mapping

Prior to each test, a complete map of the solar flux over the entire 1.4 by 2.4 m (4.5 by 8 ft) tilt table surface is accomplished. In the event more than five lamps fail during a test, post-test mapping is also performed. Using

that zone of the tilt table covered by the collector test item, the average flux point is located and a single flux intensity measurement taken with a class I total hemispherical pyranometer. This flux level value is used to compute collector performance for the test. The details of the technique used in mapping are given in Reference 5. Appendix C gives excerpts of this procedure from this reference.

The simulator lamp voltage is set by the power controller. An approximate relation between the average center point flux intensity and the power controller dial setting (Fig. 25) is used to set the initial flux near the desired setting. Subsequently, mapping is accomplished by using a phototransistor detector to measure flux intensity across the grid network on the face of the tilt table. A support frame is mounted over the tilt table surface. A lateral scanner bar which supports the detector carriage is mounted on the frame. Left-right (or east-west) scanning with the detector is accomplished by a servomotor device traversing the horizontal carriage. After a complete horizontal scan across the bed, the carriage is manually moved to a new vertical (or north-south) position where the scan is repeated. A strip chart recorder automatically records the detector output (Fig. 26). By this means, relative flux is determined from sensor data output. Grid locations are at 15 cm (6 in.) intervals across the length of the 2.4 m (8 ft) test table and on 5 cm (2 in.) centers across the 1.4 m (4.5 ft) bed width. This gives a 29 x 19 measurement array or 551 flux points. All measurements are made at a tilt angle equal to that planned for the subsequent test. The average flux value is then determined at the average flux point for the collector area by

$$\bar{S} = \sum_{i=1}^N \frac{S_i}{N} \quad , \quad (1)$$

and this fixed value is used in all performance calculations unless post-test remap becomes necessary.

## E. Wind Simulation

Typical plots of wind velocity at five points on the test table are shown in Figure 27. Using an average of the values of velocity from these points, a 3.4 m/s (7.5 mph) wind velocity is set prior to each test. The wind velocity

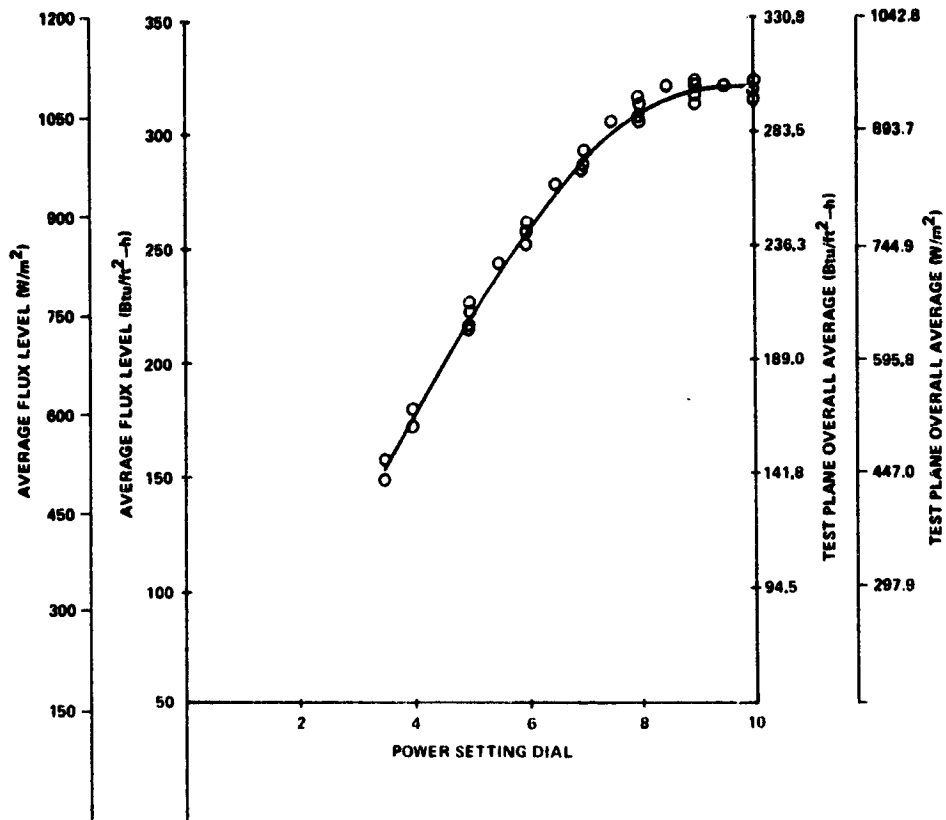


Figure 25. Test plane overall flux level versus power controller setting.

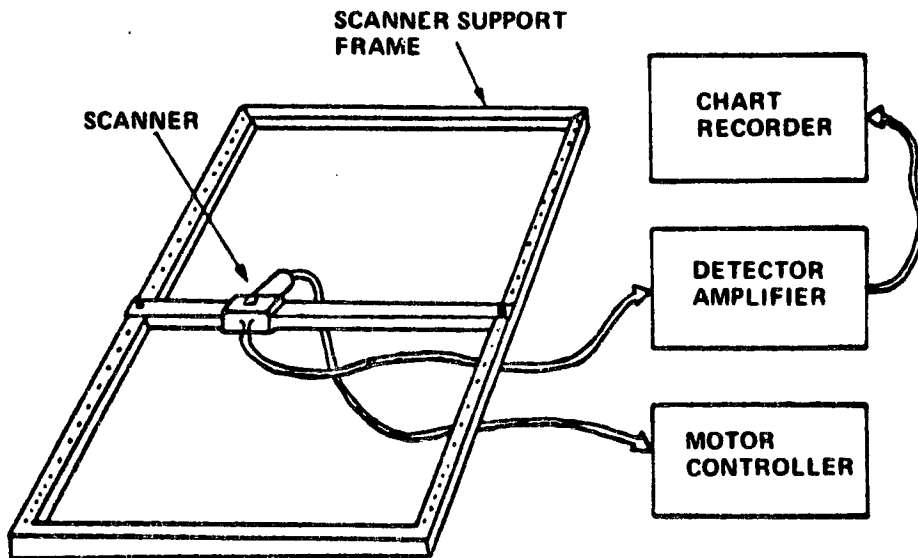


Figure 26. Uniformity measurement apparatus.

ORIGINAL PAGE IS  
OF POOR QUALITY

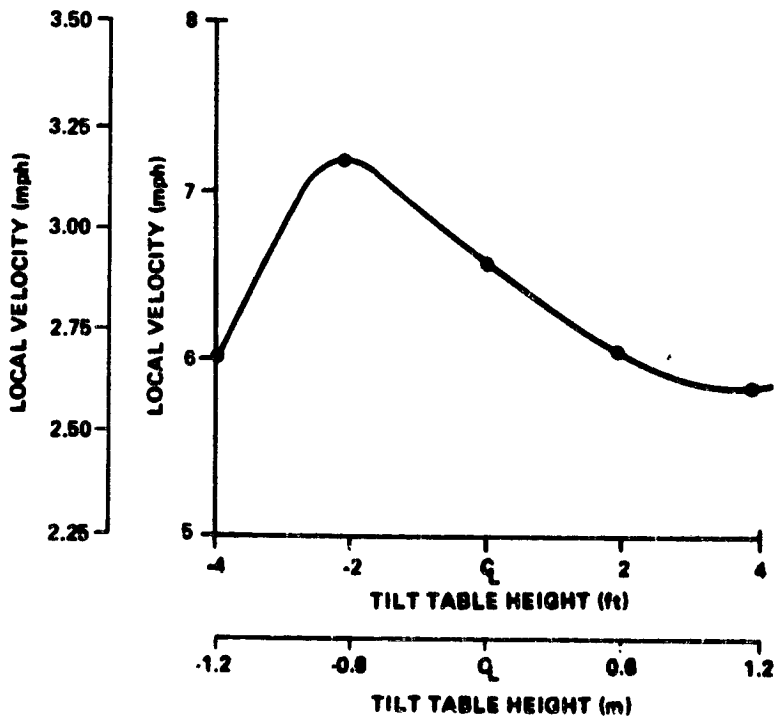
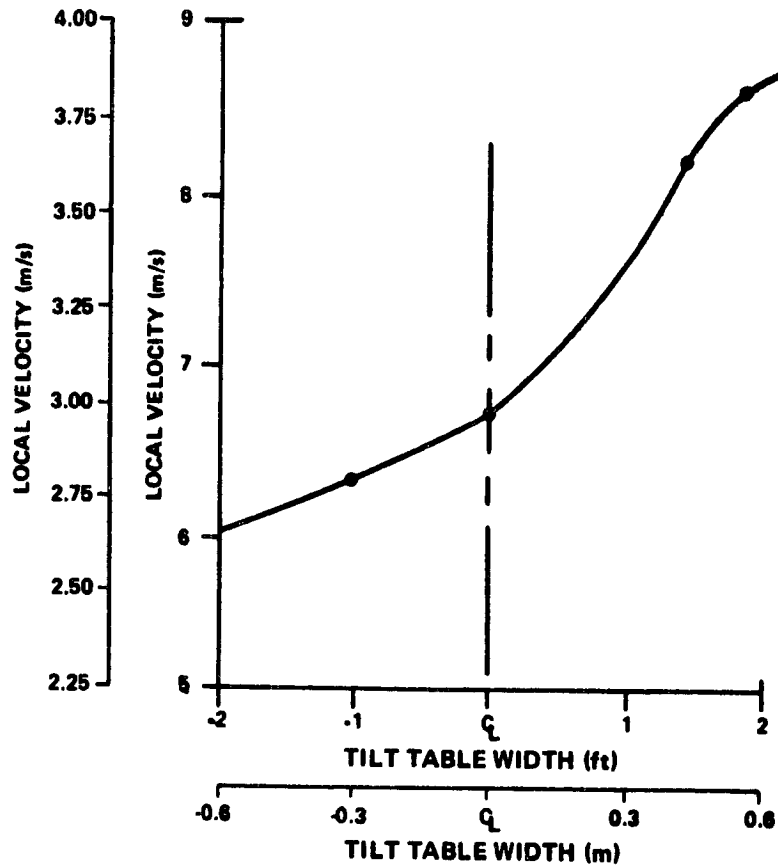


Figure 27. Typical wind velocity profile.

magnitude is controlled by simply moving the fans away from or toward the test item. Although the velocity profile as shown is not smooth, this nonuniform profile has been found to be sufficient to give good wind velocity simulation as it affects collector performance (due to the fluctuating nature of natural wind).

## IV. COLLECTOR PERFORMANCE EVALUATION

Performance testing in the simulator includes stagnation temperature determination, collector efficiency evaluation, incident angle modifier, and time constant determination. Analytical techniques used in evaluating the latter three (using simulator data) are given in detail here because they vary slightly from those techniques given in ASHRAE 93-77.

### A. Stagnation Testing

Stagnation tests (no flow or stall tests as they are sometimes called), are normally run without wind simulation and with the collector tilted at 45 deg, unless otherwise specified. Flux levels normal to the collector of 790 and 950 W/m<sup>2</sup> (250 and 300 Btu/h-ft<sup>2</sup>) are usually imposed at zero incidence angle. Maximum and average absorber plate temperatures are reported as data output for each flux level used.

### B. Collector Efficiency

The pertinent efficiency parameters are determined using experimental data. The three basic forms of the collector efficiency equation [6, 7, 8, 9] are

$$\eta = (\tau\alpha)_{e,n} - U_L \frac{(\bar{T}_p - T_a)}{I_n} \quad (2)$$

$$\eta = F' \left[ (\tau\alpha)_{e,n} - U_L \frac{(\bar{T}_f - T_a)}{I_n} \right] \quad (3)$$

$$\eta = F_R \left[ (\tau\alpha)_{e,n} - U_L \frac{(T_{ff} - T_a)}{I_n} \right] \quad (4)$$

ORIGINAL PAGE IS  
OF POOR QUALITY

Equation (4) is commonly referred to as the Hottel-Whillier-Bliss (H-W-B) Equation.

These equations are derived based on steady-state conditions. They also tacitly assume that the solar flux irradiates the entire collector area which is exactly equal to the heat loss area. However, the new collector standard, ASHRAE 93-77, specifies that the efficiency will be based on the gross or overall collector area,  $A_g$ . This gross area includes internal manifolding and mount hardware projection, as well as any other hardware affixed integrally to the collector which takes up roof or mounting space. This area is, in general, different from the collector area irradiated by normal incident solar rays,  $A_a$ , known as the aperture or irradiated area. Finally, the area through which heat is lost (defined as that portion of the absorber surface area through which energy is lost through the upper face of the collector),  $A_L$ , may be different from either the gross or aperture areas. Figure 28 shows the difference between these areas.

An energy balance on a typical flat plate collector can be used to determine the effect of these areas on the collector dependent parameters of the efficiency equations [i.e.,  $(\tau\alpha)_{e,n}$ ,  $U_L$ ,  $F'$ , and  $F_R$ ]. The instantaneous steady-state efficiency for a collector in which no work is done so that the rate of heat extracted from the collector,  $\dot{Q}_u$ , is defined by

$$\dot{Q}_u = \dot{Q}_{in} - \dot{Q}_{out} \quad , \quad (5)$$

and the collector efficiency is defined by

$$\eta = \frac{\dot{Q}_u}{\dot{Q}_i} = \frac{\dot{Q}_{in} - \dot{Q}_{out}}{\dot{Q}_i} \quad ; \quad (6)$$

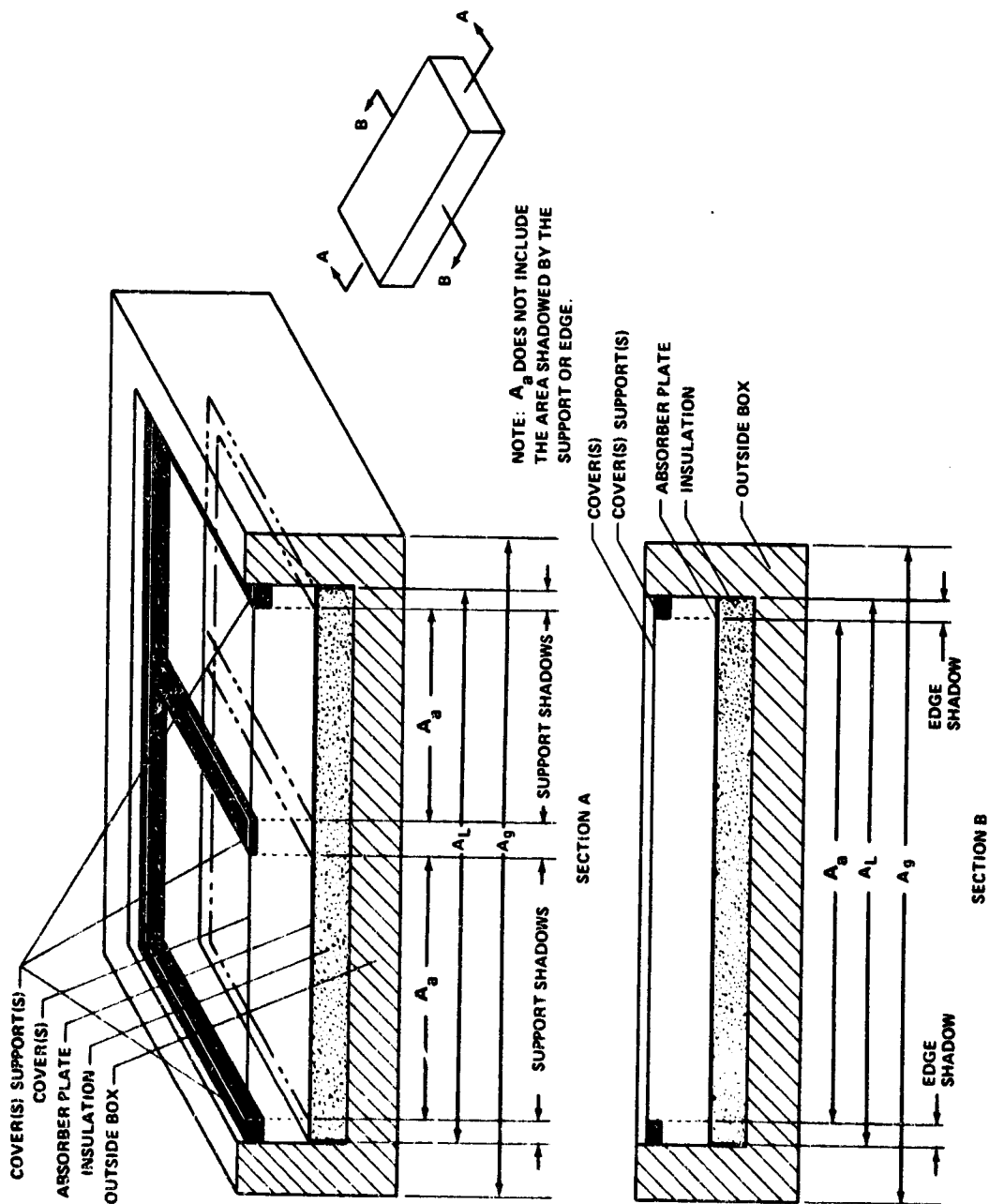


Figure 28. Collector area definitions.

however, the rate of heat incident on the collector,  $\dot{Q}_i$ , is

$$\dot{Q}_i = I_n A_g \quad . \quad (7)$$

The rate of heat into the collector absorber is

$$\dot{Q}_{in} = A_a (\tau\alpha)_{e,n} I_n \quad , \quad (8)$$

and the rate of heat loss from the absorber plate is

$$Q_{out} = A_L U_L (\bar{T}_p - T_a) \quad . \quad (9)$$

Substituting equations (7), (8), and (9) into equation (6) yields

$$\eta = (\tau\alpha)_{e,n} \frac{A_a}{A_g} - U_L \frac{(\bar{T}_p - T_a)}{I_n} \frac{A_L}{A_g} \quad . \quad (10)$$

Using experimentally generated data, the rate of heat into the collector is determined by

$$\dot{Q}_u = \dot{m} c_p (T_{fo} - T_{fi}) \quad , \quad (11)$$

or the efficiency may be found using experimental data by

$$\eta = \dot{V} \rho c_p \frac{(T_{fo} - T_{fi})}{I_n A_g} \quad , \quad (12)$$

ORIGINAL PAGE IS  
OF POOR QUALITY



where all property values are for the transport media used in testing (typical temperature varying fluid properties used in liquid collector testing is given in Appendix D). Although the loss coefficient may vary with temperature for a given collector, it has been found to be relatively accurate to assume it constant for most flat plate collectors. Therefore, assuming that the loss coefficient is constant for most flat plate collectors and that the solar incidence angle is nearly normal, the efficiency equation may be approximated by a straight line. The slope intercept is given by

$$y = a - bx \quad , \quad (13)$$

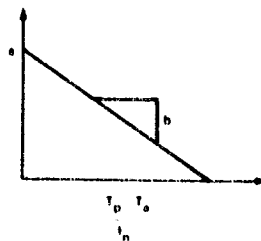
where y is by similarity to equation (10) the efficiency and x is analogous to the collector parameter  $(\bar{T}_p - T_a)/I_n$ . By this comparison, the y intercept, a, is given by

$$a = \frac{A_a}{A_g} (\tau\alpha)_{c,n} \quad , \quad (14)$$

where the subscript n is added to assure normal incident values are used and the slope, b, is given by

$$b = \frac{A_L}{A_g} U_L \quad . \quad (15)$$

Since  $A_g$ ,  $A_a$ , and  $A_L$  are measurable physical quantities of the collector,  $(\tau\alpha)_{c,n}$  and  $U_L$  may be determined from linear fits of experimental data if they do not vary with temperature or incident flux.



Likewise, the abscissa can be altered so that  $F'$  and  $F_R$  may be determined by using two efficiency equations derived in a fashion similar to equation (10). These derivations yield

$$\eta = F' \left[ \frac{A_a}{A_g} (\tau\alpha)_{e,n} - U_L \frac{A_L}{A_g} \frac{(\bar{T}_f - T_a)}{I_n} \right] \quad (16)$$

and

$$\eta = F_R \left[ \frac{A_a}{A_g} (\tau\alpha)_{e,n} - U_L \frac{A_L}{A_g} \frac{(T_{fi} - T_a)}{I_n} \right] \quad (17)$$

Using equation (16), values for the constants in the linear equations are found by

$$a_1 = F' \frac{A_a}{A_g} (\tau\alpha)_{e,n} \quad (18)$$

and

$$b_1 = F' \frac{A_L}{A_g} U_L \quad (19)$$

and, using equation (17), by

$$a_2 = F_R \frac{A_a}{A_g} (\tau\alpha)_{e,n} \quad (20)$$

and

$$b_2 = F_R \frac{A_L}{A_g} U_L \quad (21)$$

Using the  $(\tau\alpha)_{e,n}$  and  $U_L$  values determined earlier,  $F'$  can be determined from either equation (15) or (16) and checked, and  $F_R$  can be determined from either equation (20) or (21) and checked.

To acquire these data, efficiency tests are run at a fixed flux value of  $791 \text{ W/m}^2$  ( $250 \text{ Btu/h-ft}^2$ ) with the illumination rays normal to the collector. The collector is tilted at 45 deg and the room ambient temperature is allowed to float (but usually remains fairly steady). Depending on time of year, the ambient temperature will normally range between 16 and 27°C (60 and 80°F). The wind machine blows room air into the collector (from simulated due south) at a 3.4 m/s (7.5 mph) average velocity. The flowrate is maintained at  $101.354 \text{ N/m}^2$  ( $14.7 \text{ lb/h-ft}^2$ ) for liquid transport media and  $0.6 \text{ m}^3/\text{h-m}^2$  ( $2 \text{ cfm/ft}^2$ ) for air. With these fixed conditions, the collector inlet temperature is controlled at discreet preselected values [usually 0, 14, 28, 42, and 55°C (0, 25, 50, 75, and 100°F) above ambient] until a steady-state collector outlet temperature is achieved. Using the average collector plate (Fig. 29), fluid inlet, fluid outlet, and ambient air temperatures along with fluid properties and flux values determined during mapping, collector correlator parameters,  $\Gamma$ , are determined and plotted against efficiency (Fig. 30). Using these data along with collector area measurements, data points are plotted for the three different collector efficiency correlators. These data points are then put in a linear regression program and a first order curve fit is generated from these data points. The slope and intercept are found for this curve and the collector parameters determined as discussed earlier. Although not specified in ASHRAE 93-77, air collector efficiency tests are run at a number of flowrates. From early tests, it has been discovered that efficiency maps vary considerably depending on what flowrate is used. For these reasons, most air collector tests are conducted at a minimum of two flowrates. One flowrate is set as indicated at  $0.6 \text{ m}^3/\text{h-m}^2$  ( $2 \text{ cfm/ft}^2$ ), the other at an arbitrary higher flowrate or at a value recommended by the manufacturer.

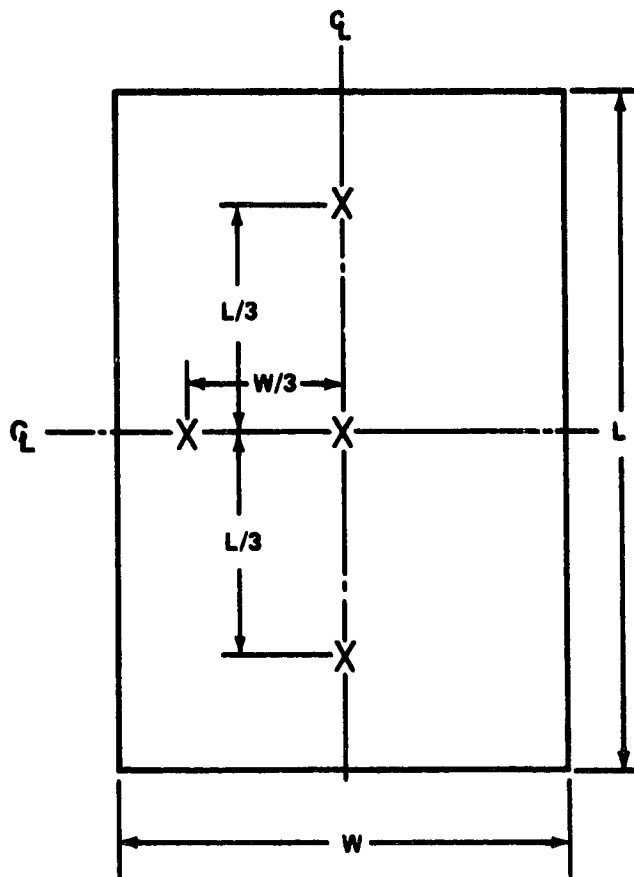


Figure 29. Typical collector surface measurement locations.

For collectors with size envelopes which are larger than the 1.2 by 2.4 m (4 by 8 ft) irradiation capability, a special test arrangement is used. In these cases, efficiency data are generated in the simulator with a portion of the collector intentionally shaded. The shadowed area,  $A_s$ , is obscured by an opaque plate to assure zero irradiation input to this part of the collector. This causes the irradiated or aperture area,  $A_a$ , to be significantly less than the loss area,  $A_L$ , so that

$$A_L = A_s + A_a \quad (22)$$

ORIGINAL PAGE IS  
POOR QUALITY

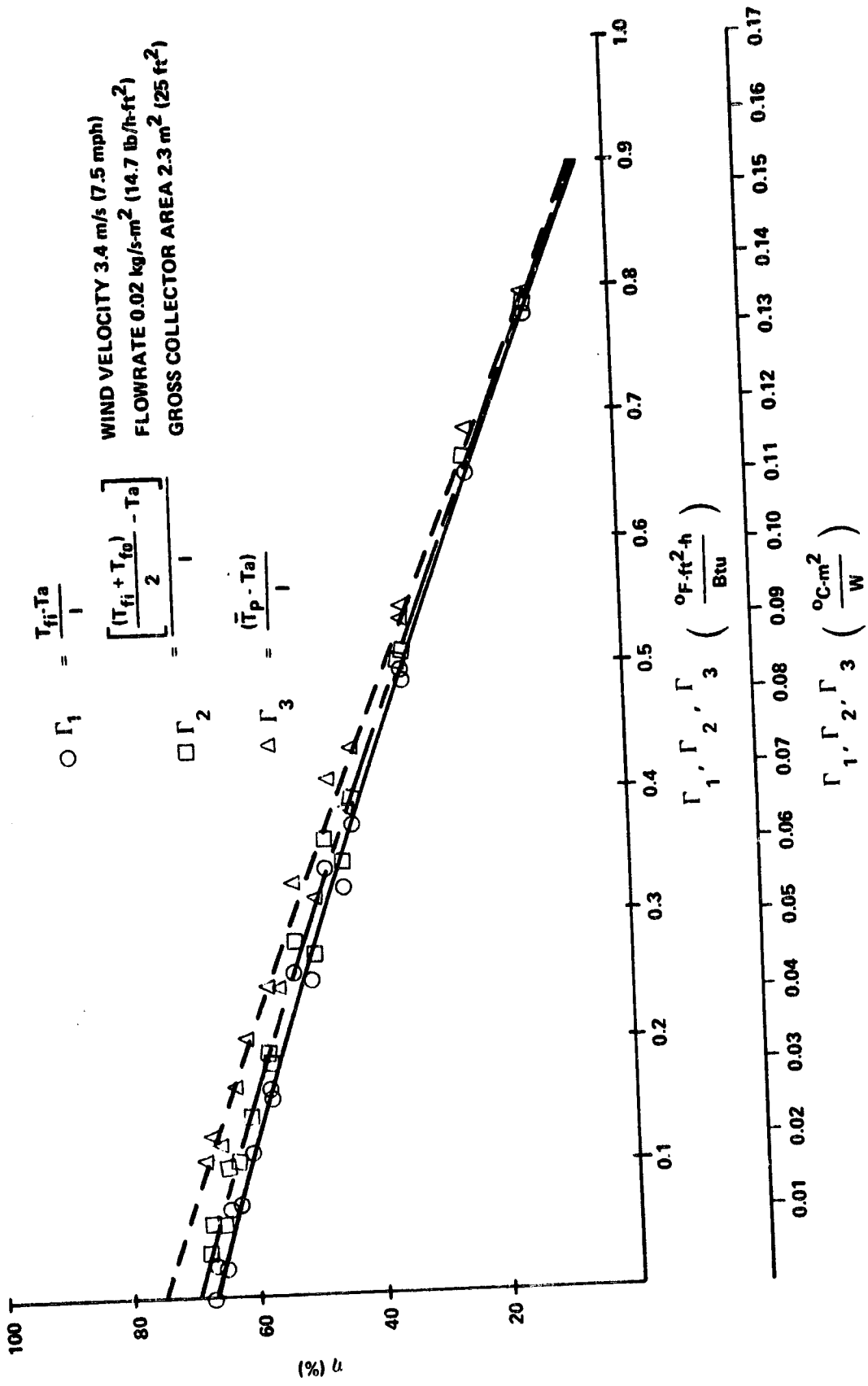


Figure 30. Collector indoor thermal performance test.

Using this efficiency data gathered in the simulator with a portion of the collector shaded, corrections are made to make these data applicable to a fully irradiated collector. Justification for these correction techniques follows.

The energy collected,  $\dot{Q}_u$ , is given by

$$\dot{Q}_u = F_{R_s} A_a \{ [(\tau\alpha)_{e,n}]_s I_n - U_{L_s} (A_a + A_s) (T_{fi} - T_a) \} \quad (23)$$

and

$$\eta_s = F_{R_s} \left\{ \frac{A_a}{A_g} [(\tau\alpha)_{e,n}]_s - U_{L_s} \frac{(A_a + A_s)}{A_g} \frac{(T_{fi} - T_a)}{I_n} \right\} \quad (24)$$

where the irradiated area for an unshaded collector is given by  $A_a + A_s$ . If the collector is not shaded, the energy collected is given by

$$\dot{Q}_u = F_R \{ (A_a + A_s) (\tau\alpha)_{e,n} I_n - U_L (A_a + A_s) (T_{fi} - T_a) \} \quad (25)$$

and

$$\eta = F_R \left\{ \frac{(A_a + A_s)}{A_g} (\tau\alpha)_{e,n} - U_L \frac{(A_a + A_s)}{A_g} \frac{(T_{fi} - T_a)}{I_n} \right\} \quad (26)$$

Now, since  $(\tau\alpha)_{e,n}$  is a function only of coating properties,  $F_R$  is dependent on flowrate and collector configuration, and  $U_L$  is normally only weakly dependent on collector temperature; i.e.,

$$[(\tau\alpha)_{e,n}]_s = (\tau\alpha)_{e,n} \quad ,$$

$$F_{R_s} = F_R \text{ and } U_{L_s} = U_L \quad ,$$

ORIGINAL PAGE IS  
OF POOR QUALITY

(27)

from which

$$\eta = F_R \left\{ \frac{A_a}{A_g} (\tau\alpha)_{c,n} + \frac{A_s}{A_g} (\tau\alpha)_{c,n} - U_L \frac{A_a + A_s}{A_g} \frac{(T_{fi} - T_a)}{I_n} \right\} \quad (28)$$

$$\eta = \eta_s + F_R \frac{A_s}{A_g} (\tau\alpha)_{c,n} \quad (29)$$

Therefore, simulator efficiency data generated by shadowing a portion of the collector are corrected by simply adding the second term to the simulator generated efficiency.

Figure 31 compares experimental data for a collector tested with full irradiation to corrected data for the same collector with only partial irradiation. The fully irradiated item was tested outside with the shaded collector item tested indoors in the simulator. Examination of these curves shows relatively good correlation between data from the two test conditions for two internal air flow-rates in the air collector.

Comparison of the collector efficiency parameters  $\{(\tau\alpha)_c, F^t, F_R, \text{ and } U_L\}$  allows relative and absolute assessment of collector performance. However, because of the limits of the environmental conditions when generating these data, they must be applied carefully. Two of the more significant variables whose effect on collector performance is not apparent when examining collector efficiency parameters only are (1) the effect of incident angles other than normal and (2) the effect of the collector capacitance or thermal response important in transient conditions. These two effects are, however, addressed by other testing to be discussed later. Other performance effects of some importance, but which are not significant enough to warrant evaluation in each collector test, are those of wind velocity and direction variations and loss coefficient changes with temperature. Experimental data give the effects of wind velocity on a selectively coated, double glass liquid collector and a single glass, nonselective air collector (Fig. 32). Wind direction effects have not been examined experimentally. Typical loss coefficient variation with temperature is given for a single covered, nonselective collector as depicted in Figure 33.

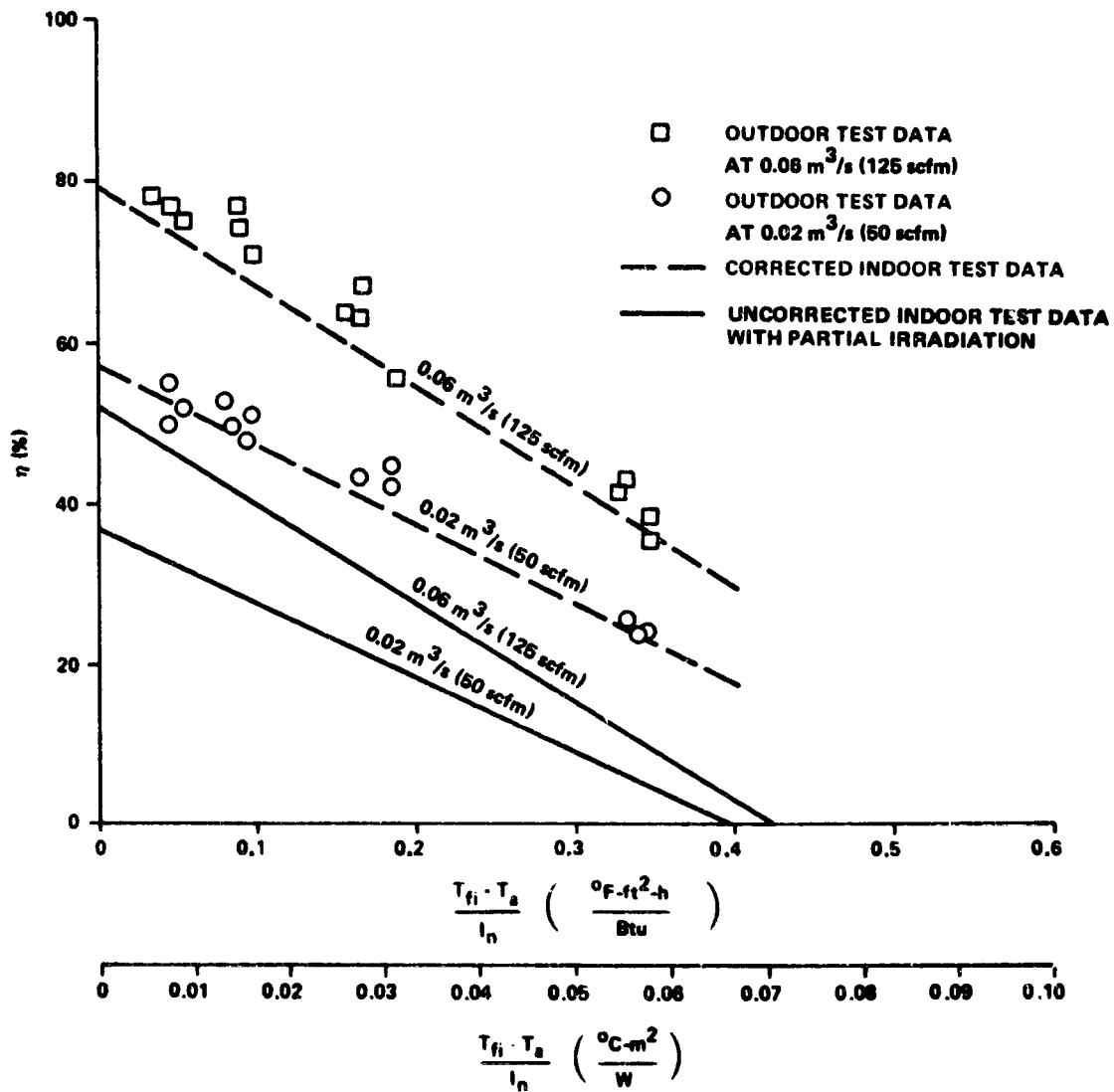


Figure 31. Overall collector efficiency data.

ORIGINAL PAGE IS  
OF POOR QUALITY



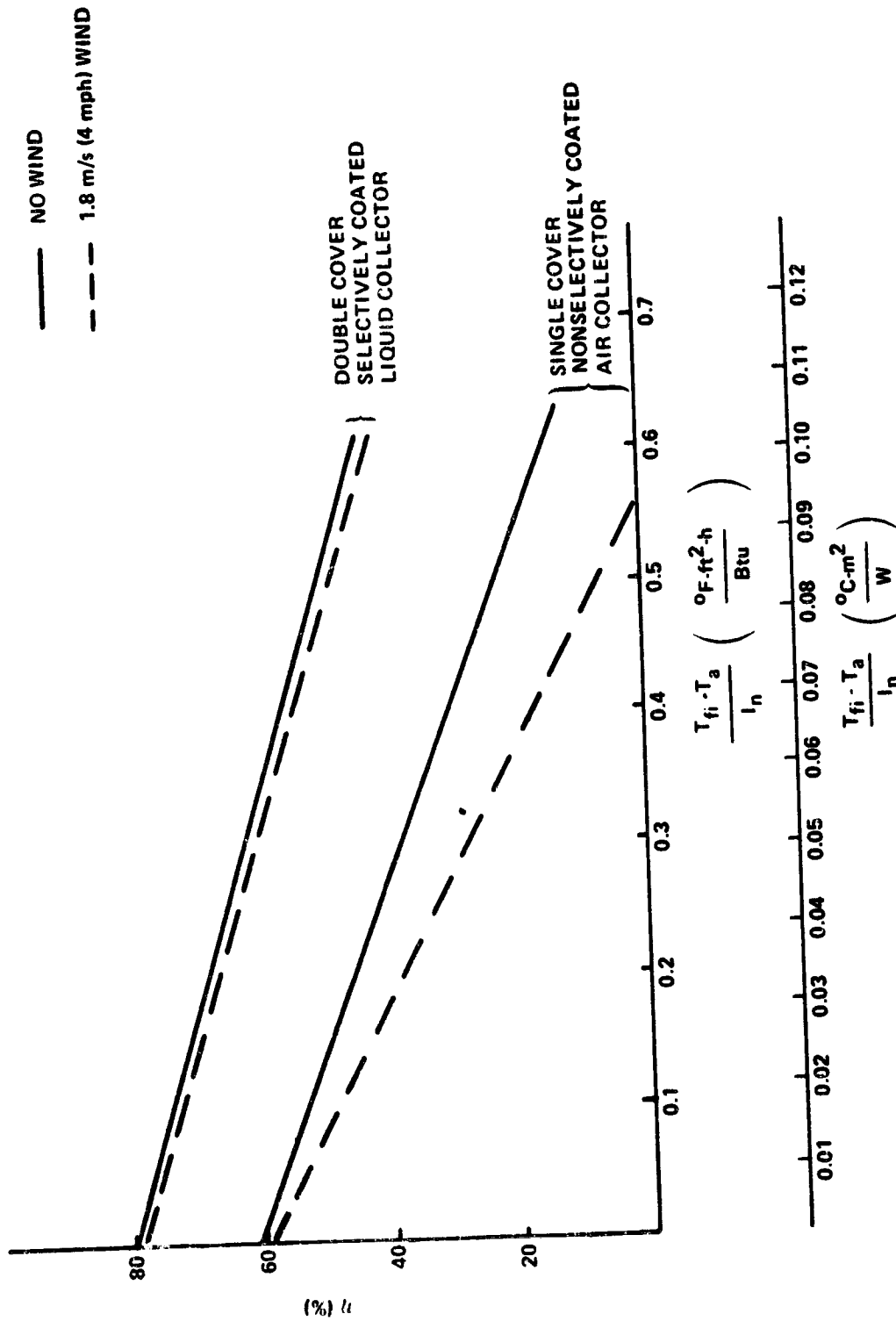


Figure 32. Effect of wind on collector efficiency.

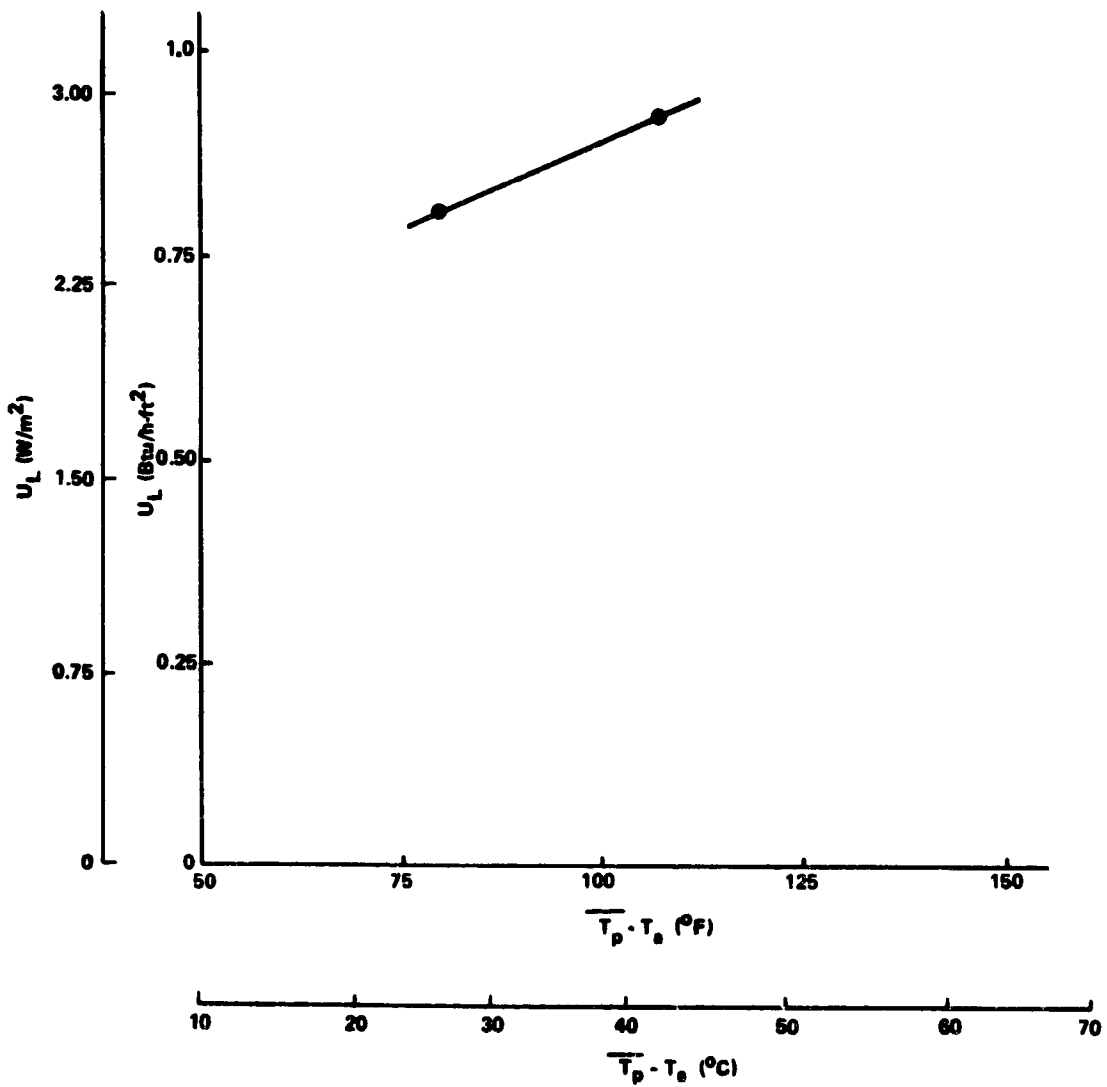


Figure 33. Typical variation of heat loss with temperature.

ORIGINAL PAGE IS  
OF POOR QUALITY

Although evaluation of these effects are within the capability of this facility, other effects are not. These include the capability of determining the effects of parameters such as sky sink temperature and diffuse to direct flux ratios. Aging and other environmental effects such as dust accumulation on the cover, precipitation effects of rain, snow, sleet, and hail, the corrosive effects of outdoor conditions, and long duration effects such as ultraviolet degradation and outgassing are accomplished to some extent in outdoor facility testing and during laboratory testing of material coupons.

### C. Incident Angle Modifier

The efficiency plot as discussed in Paragraph IV. B does not completely define the efficiency variation, since it assumes  $(\tau\alpha)_e$  does not vary regardless of the solar incident angle. This is not always true because the spectral properties of covers and coatings vary dramatically at high incident angles (Fig. 34). Most efficiency data are, however, reported for near normal incident radiation test conditions. Reference 10 indicates these angles should be restrained to values less than 30 deg. Since the Sun angle varies significantly with time of day on a fixed tilt collector, evaluation of this variable is important.

To use the previously discussed H-W-B efficiency equation for variable incidence angles, a new factor known as the incident angle modifier,  $K_{\tau\alpha}$ , is introduced to correct the  $(\tau\alpha)_{e,n}$  value. This value is defined as

$$K_{\tau\alpha} = \frac{(\tau\alpha)_{e,\theta}}{(\tau\alpha)_{e,n}} \quad (30)$$

The use of an "all day" or "overall" efficiency factor to account for this variation in collector efficiency is also common. Unfortunately, the definitions used in finding this value usually includes other effects. In particular, system peculiar effects as well as those effects associated with the collector's thermal dynamics (e.g., collector control logic and collector time response) are included. Since the modifier is not dependent on these type effects, it is preferable.

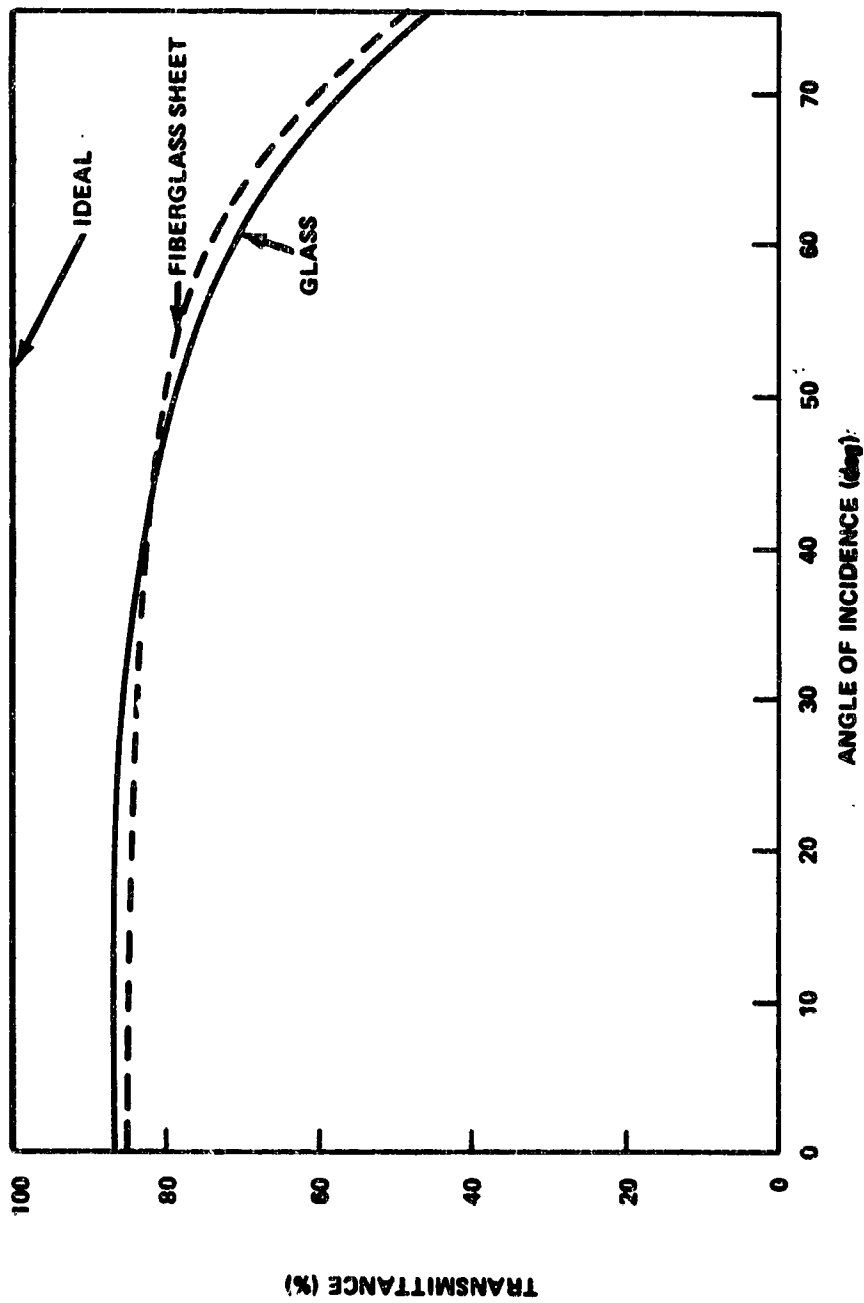


Figure 34. Variation of transmittance with incidence angle.

ORIGINAL PAGE IS  
OF POOR QUALITY

The modifier operates on the first term of the H-W-B equation and can be further defined by

$$K_{\tau\alpha} = \frac{F_R(\tau\alpha) e, \theta}{\eta_{e, n}} \quad (31)$$

Using this, the H-W-B efficiency equation may then be rewritten as

$$\eta = F_R \left[ \frac{A_a}{A_g} K_{\tau\alpha}(\tau\alpha) e, n - U_L \frac{A_L}{A_g} \frac{(T_{fi} - T_a)}{I_n} \right] \quad (32)$$

In using equation (32) to experimentally determine  $K_{\tau\alpha}$ , Reference 10 requires that  $T_{fi}$  be set equal to  $T_a$  within  $\pm 2^\circ\text{F}$ . Since this test condition is difficult to achieve in the simulator, a more general definition of  $K_{\tau\alpha}$  was used for which  $T_{fi} \neq T_a$ . This is obtained by solving equation (32) for  $K_{\tau\alpha}$ ; i. e.,

$$K_{\tau\alpha} = \frac{\eta + F_R U_L \frac{A_L}{A_g} \frac{(T_{fi} - T_a)}{I_n}}{(\tau\alpha)_{e, n} F_R \frac{A_a}{A_g}} \quad (33)$$

Since  $K_{\tau\alpha}$  varies, as the spectral properties, with  $\cos \theta$  [10], it may be written in the form

$$K_{\tau\alpha} = 1 + b \left( \frac{1}{\cos \theta} - 1 \right) \quad (34)$$

where  $b$  is experimentally determined as indicated. Values for  $b$  are found at 0, 30, 45, and 75 deg incident angles. Then, using this value along with previously determined values of  $F_R$ ,  $(\tau\alpha)_{e,n}$ , and  $U_L$ , the more general form of the efficiency equation, equation (32), can be used to determine collector performance for any Sun/collector attitude.

During initial incident angle modifier tests, it was discovered that incident solar energy normal to the collector face deviated from the expected cosine relationship for a direct beam ray as the incident angle was increased. This deviation is quite large for large incident angles and is shown in Figure 35.

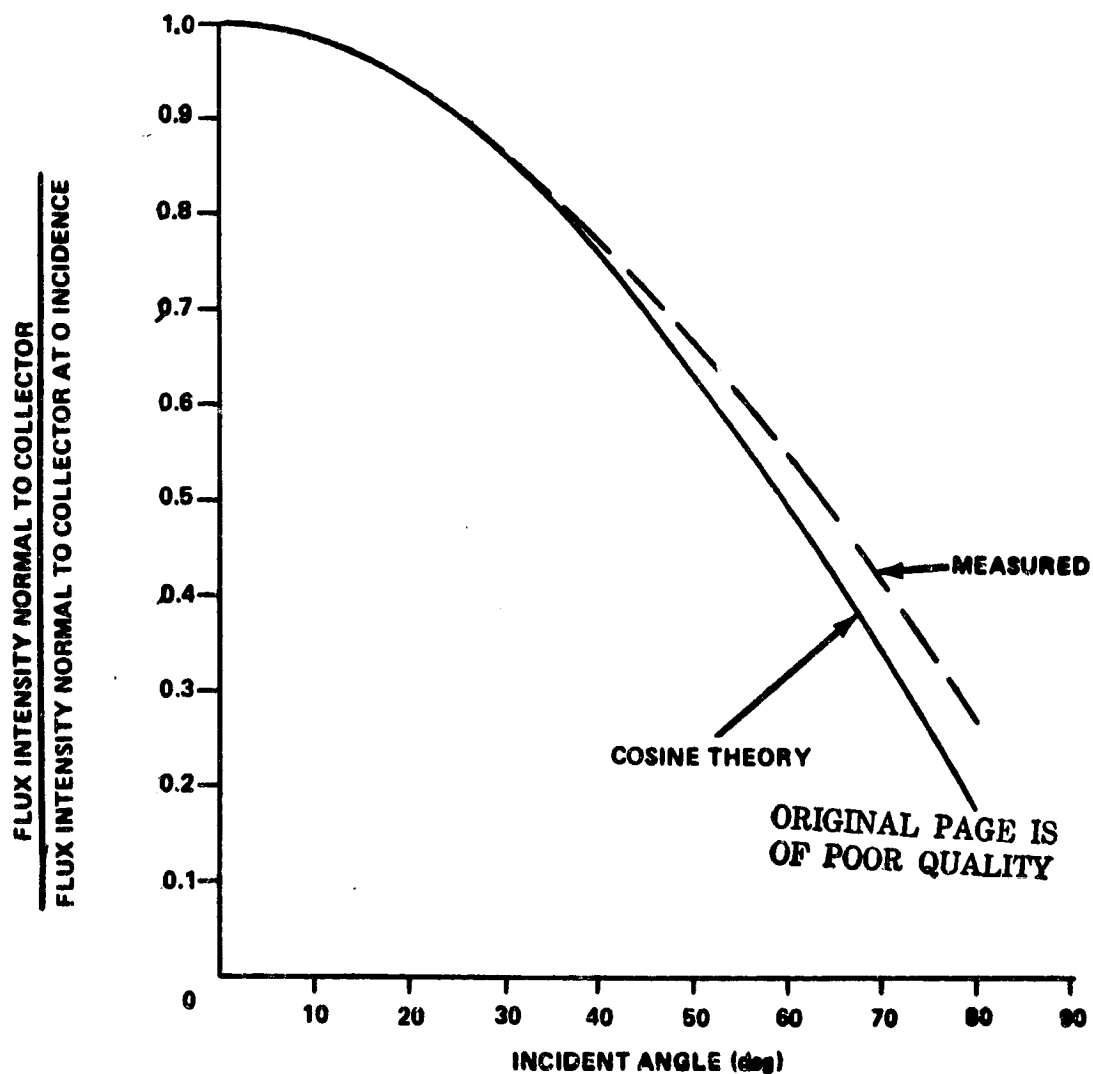


Figure 35. Variation of normal flux with incidence angle.

The deviation indicates a larger total flux at high incidence angles than is predicted. This is a result of reflected energy from the tilt table and adjacent hardware. In the future, plans are to cover the reflecting surface with a black cloth in an attempt to inhibit the reflections.

During the first few incident angle tests, control of incidence angles was achieved by simple rotation of the tilt table in the horizontal plane. However, the exact change in incident angle had to be determined by calculations due to the two-dimensional effects; i. e., horizontal rotation changed the apparent tilt and azimuth angle. Furthermore, it was found that certain collector configurations yield incident angle modifiers which vary differently in the north-south plane than they do in an east-west plane (Fig. 36). As a result of these complications, a special fixture was built which allowed limiting incident angle changes to only azimuthal or east-west variations. Collectors whose physical characteristics indicate the modifier variations in these two planes could occur are evaluated in the north-south plane also by simply rotating the Sun simulator.

Figure 37 shows a photograph of such a collector which does have a preferential modifier. In this particular design, a sheet of plastic is accordioned between the absorber and the outer cover. The accordion folds run east-west (or left-right-left as seen in the photograph). In the east-west plane the incident rays are nearly parallel to the folds; however, in the north-south plane the oblique ray must pass through an increased number of plastic layers. Therefore, it is apparent the incident angle modifier would decrease more dramatically with angle in the north-south plane. Figures 38 and 39 show experimental data which demonstrate this effect on the illustrated collector.

## D. Time Constant

The efficiency data discussed earlier is generated for steady-state conditions only. However, none of the parameters discussed indicate the transient behavior of the collector. For this reason, the collector time constant is also determined to quantify the relative transient behavior of the collector.

The unsteady energy equation governing heat transfer in the collector, assuming the entire collector acts at the fluid temperature and normal incident flux with no work, is

$$\dot{Q}_{\text{stored}} = \dot{Q}_{\text{in}} - \dot{Q}_{\text{out}} \quad .$$

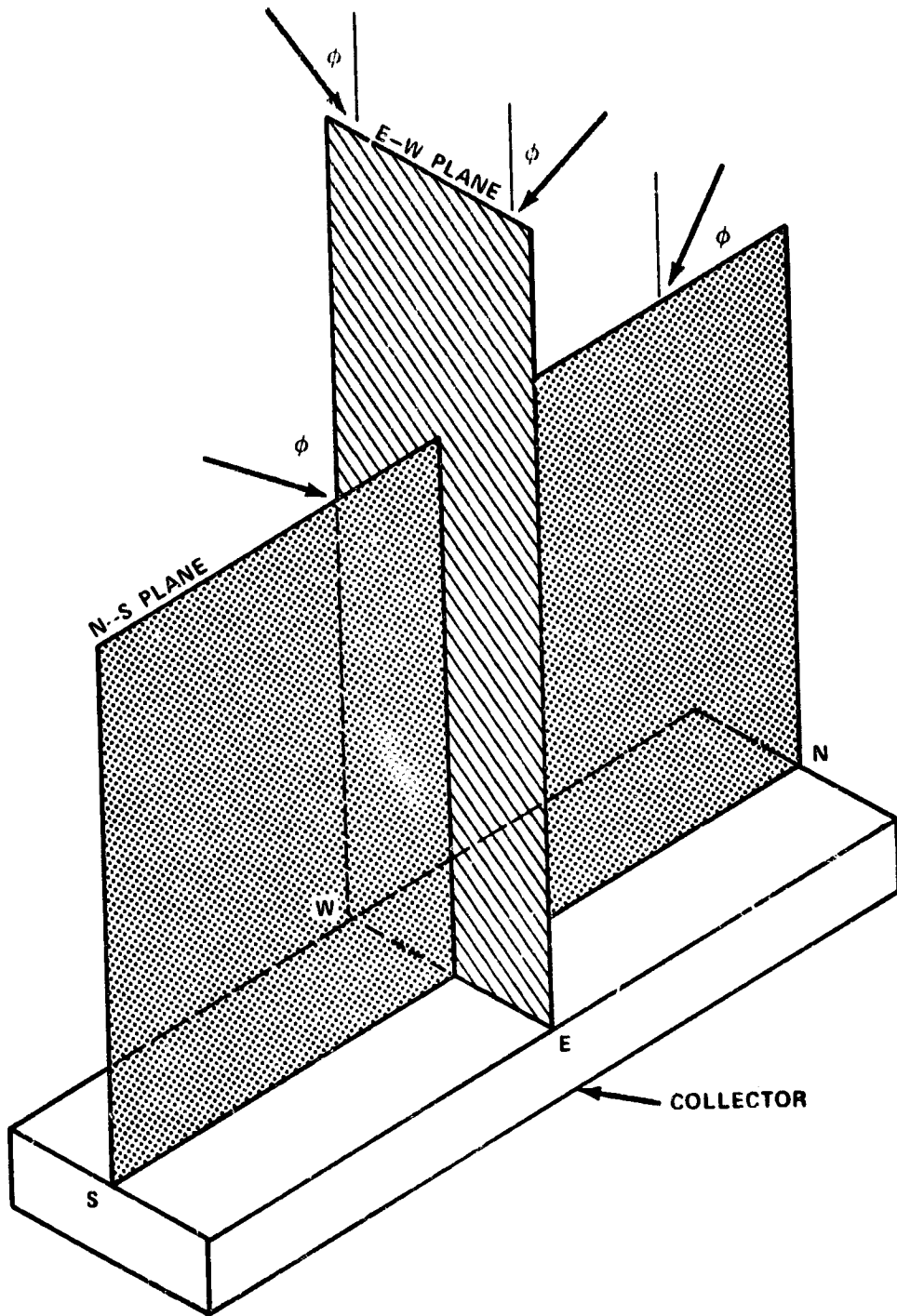


Figure 36. Preferential incidence angle modifier.

ORIGINAL PAGE IS  
OF POOR QUALITY



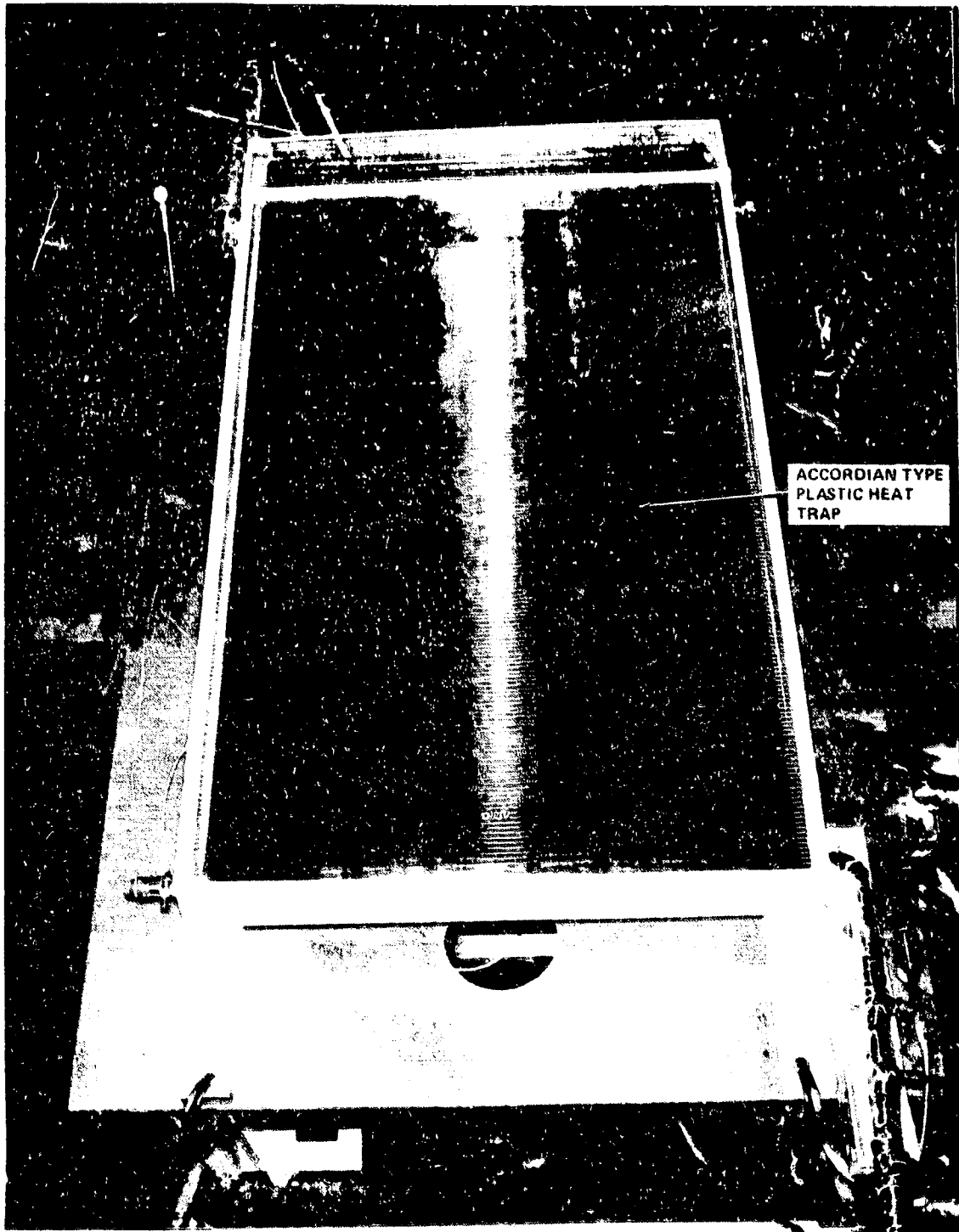
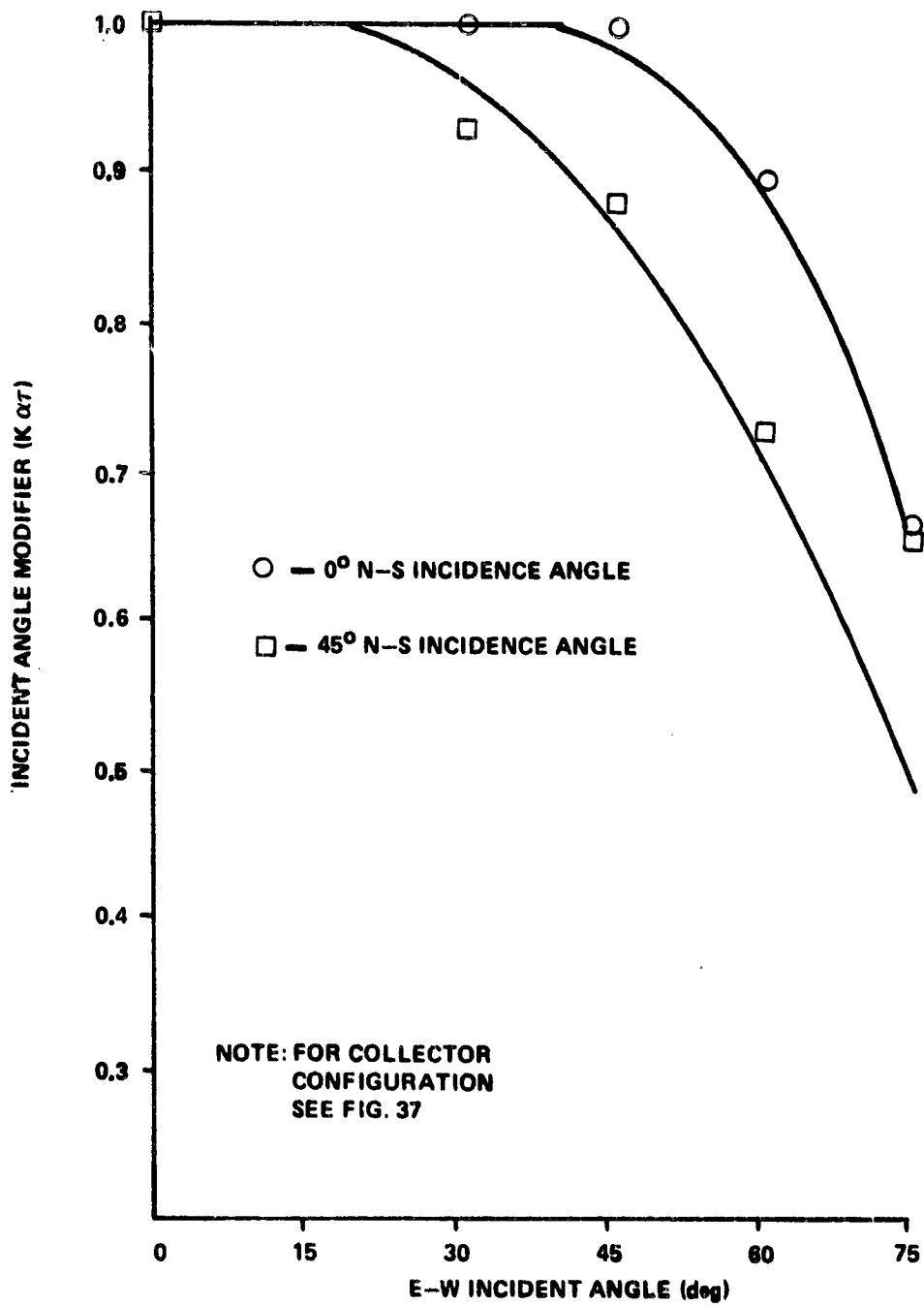


Figure 37. Collector with preferential incidence angle modifier.



ORIGINAL PAGE IS OF POOR QUALITY

Figure 38. Collector incidence angle modifier versus east-west incidence angle.

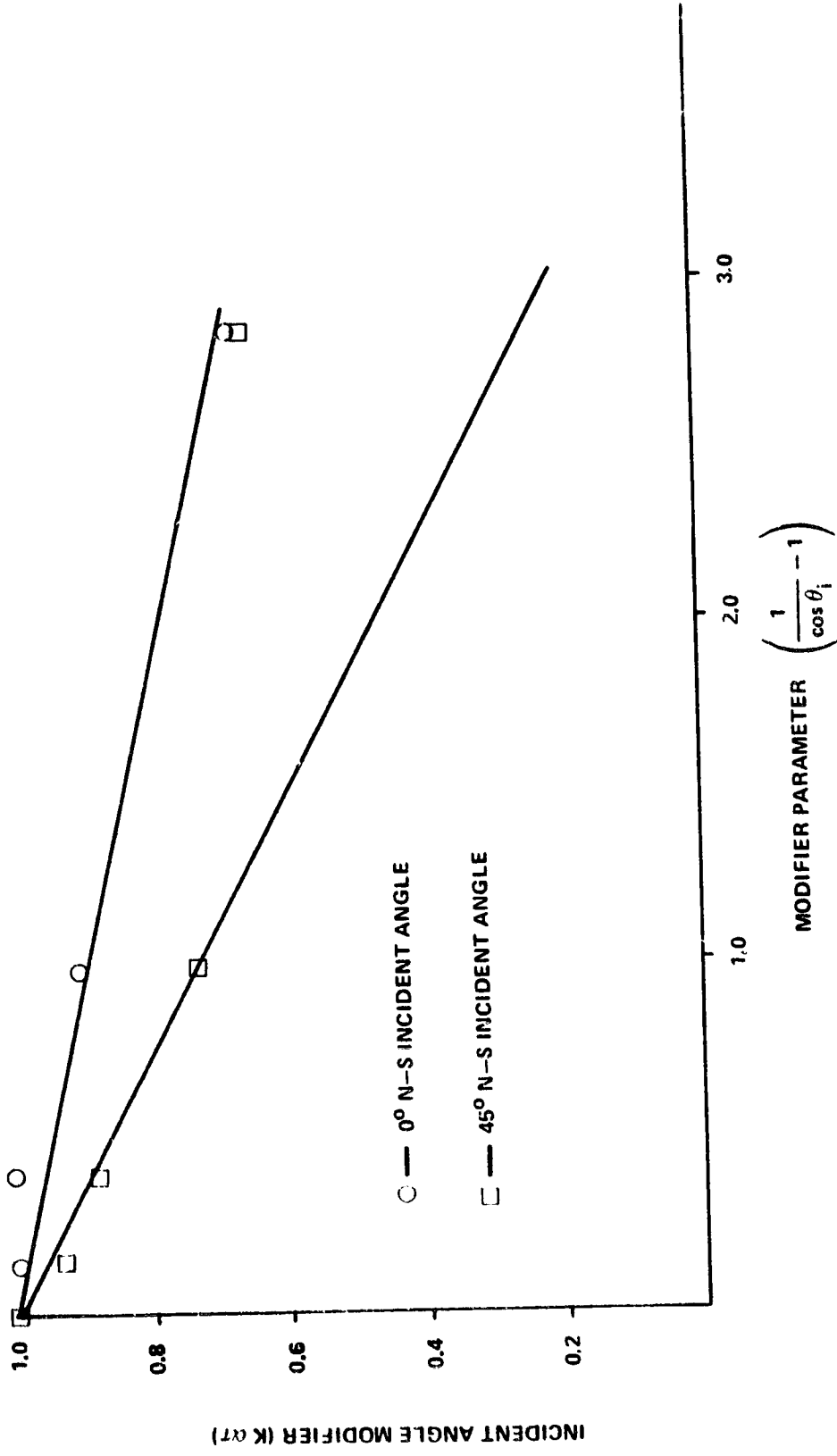


Figure 39. Collector incident angle modifier versus modifier parameters.

Using the unsteady energy balance equation and the average fluid temperature similar to equation (16), we find

$$(\dot{m}c_p)_f (T_{fo} - T_{fi}) = F' [I_n A_a (\tau\alpha)_e - U_{L L} A_L (\bar{T}_f - T_a)] \quad (35)$$

Now, if  $T_a$  and  $T_{fi}$  are held constant, we can differentiate so that

$$(\dot{m}c_p)_f \cdot dT_{fo} = F' A_a (\tau\alpha)_e dI_n - F' U_{L L} A_L d\bar{T}_f \quad (36)$$

Using the numerators of equations (16) and (17) we see

$$F' [A_a (\tau\alpha)_e I_n - U_{L L} A_L (\bar{T}_f - T_a)] = F'_R [I_n A_a (\tau\alpha)_e - U_{L L} A_L (T_{fi} - T_a)] \quad ,$$

and after differentiation (with a constant  $T_a$  and  $T_{fi}$ ) we find that

$$F' A_a (\tau\alpha)_e dI_n - F' U_{L L} A_L d\bar{T}_f = F'_R A_a (\tau\alpha)_e dI_n \quad ,$$

and after rearranging, we find that

$$[F' A_a (\tau\alpha)_e - F'_R A_a (\tau\alpha)_e] dI_n = F' U_{L L} A_L d\bar{T}_f \quad (37)$$

Solving equation (37) for  $dI_n$  and substituting into equation (36), we have

$$(\dot{m}c_p)_f dT_{fo} = F' A_a (\tau\alpha)_e \left[ \frac{F' U_{L L} A_L d\bar{T}_f}{F' A_a (\tau\alpha)_e - F'_R A_a (\tau\alpha)_e} \right] - F' U_{L L} A_L d\bar{T}_f \quad .$$

ORIGINAL PAGE IS  
OF POOR QUALITY

Rearranging and simplifying, we find that

$$(\dot{m}cp)_f dT_{fo} = F^v U_L A_L \left( \frac{F^v}{F^R} - 1 \right) d\bar{T}_f$$

or

$$\frac{(\dot{m}cp)_f dT_{fo}}{F^v U_L A_L} = \frac{1}{\left[ \frac{F^v}{F^R} - 1 \right]} d\bar{T}_f \quad (38)$$

Solving for  $d\bar{T}_f/dt$ ,

$$\frac{d\bar{T}_f}{dt} = \frac{(\dot{m}cp)_f}{F^v U_L A_L} \left[ \frac{F^v}{F^R} - 1 \right] \frac{dT_{fo}}{dt} \quad (39)$$

Similarly, an unsteady energy balance on the collector/fluid control volume yields

$$\begin{aligned} (\dot{m}cp)_{f+c} \frac{d\bar{T}_f}{dt} &= F^R [\Lambda_a (\tau a)_{e,n} - U_L A_L (T_{fi} - T_a)] \\ &\quad - (\dot{m}cp)_f \cdot (T_{fo} - T_{fi}) \end{aligned} \quad (40)$$

where  $(\dot{m}cp)_{f+c}$  is the effective capacitance of the collector/fluid combination.

Substituting equation (39) into (40) and integrating both sides from the initial conditions ( $\bar{T}_{fo, \text{initial}}$  and  $t = 0$ ) to  $t = t$ , we find that

$$\frac{F_{R_a n} I(\tau_a)_{e,n} - U_L A_L (T_{fi} - T_a) - (\dot{m}c_p)_f (T_{fo} - T_{fi})}{F_{R_a n} I(\tau_a)_{e,n} - U_L A_L (T_{fi} - T_a) - (\dot{m}c_p)_f (T_{fo_{initial}} - T_{fi})} = e^{-[(\dot{m}c_p)_f / K(\dot{m}c_p)_{f+c}]t} \quad (41)$$

where  $K$  is the coefficient of  $dT_{fo}/dt$  in equation (39) and the quotient exponent of the right side of equation (41),  $(\dot{m}c_p)_f / K(\dot{m}c_p)_{f+c}$ , is defined as the time constant. The response time is the time required for the left side of equation (41) to reach 36.8 percent of its initial value.

In tests, this value is found by subjecting the collector to a normal flux of  $790 \text{ W/m}^2$  ( $250 \text{ Btu/h-ft}^2$ ). Other conditions are set as prescribed in the previously discussed efficiency tests. The one exception is that the collector fluid inlet,  $T_{fi}$ , is set to within  $7^\circ \text{C}$  ( $12^\circ \text{F}$ ) of ambient rather than  $\pm 1^\circ \text{C}$  ( $2^\circ \text{F}$ ) and held constant. After steady-state is reached, the simulator illumination array is turned off. This condition is defined as the zero time state and the left side of equation (39) is plotted versus time. The time, in minutes, to reach the 36.8 percent point is obtained from a strip chart plot. This value is the response time constant. Figure 40 illustrates an example of how this value is extracted from test data.

## E. Variations from ASHRAE Standard 93-77

The test facility has the capability of meeting most of the test requirements given in the ASHRAE standard 93-77 entitled "Method of Testing Solar Collectors Based on Thermal Performance" [10]. Some differences between this standard requirement and those practiced at this facility do exist. These deviations in some cases are intentional, in others they result from facility operational design limitations which occurred before this standard was published. Facility modifications to conform with ASHRAE 93-77 are either deemed not feasible or considered unnecessary. Since this is the most widely accepted collector test standard to date, it is worthwhile to detail these differences as they exist using the standard requirements as the reference. If no deviations are indicated, ASHRAE standards are met. The specific paragraphs in the standard in which these differences occur are 2.1, 2.4, 5.1.1, 5.1.2, 6.6.6, 6.1.3, 6.2.2, 7.1.2, 7.1.3, 7.1.4, 7.1.5, 7.2.7, 7.3.3, 7.3.5, 8.2, 8.9, 9.1, and 9.2. A more detailed discussion of these deviations follows.

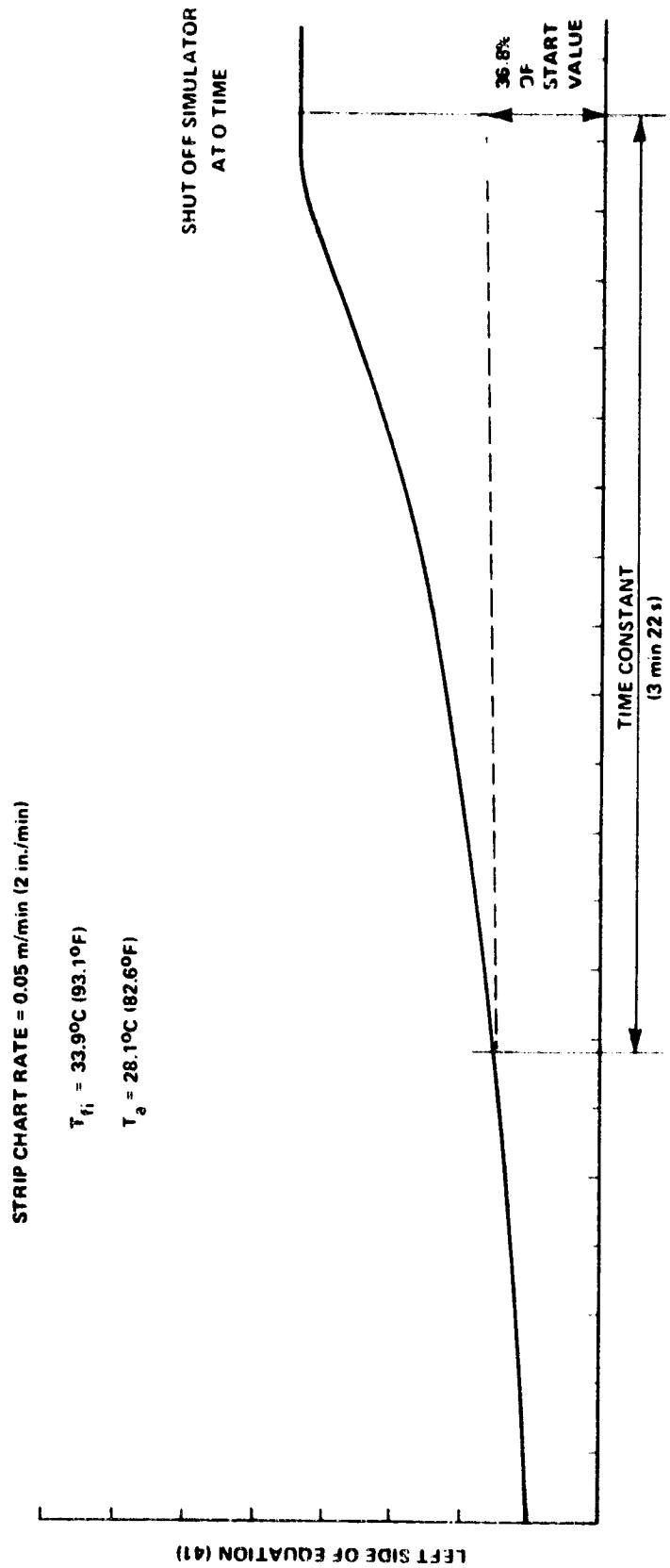


Figure 40. Typical collector time constant plot.

In general, ASHRAE requirements are given for concentrating and non-concentrating collectors (Paragraph 2.1), where this facility is designed to accommodate only flat plate collectors. This does not preclude performance testing of other nonconcentrating or possibly some type of concentrating collector types; however, these capabilities have not been addressed to date. In general, new collectors are tested in the simulator, then exposed and retested at 6-month intervals after exposure to assess weathering effects. The collectors are tested as a single unit (module) with no external manifolding included (Paragraph 5.1.2). No attempt is made to simulate edge, end, or backside loss boundary conditions which occur in actual installations as noted in the standard.

All collector efficiency tests are run at 0 deg azimuth and 45 deg tilt unless special test requirements are specified. A 50/50 by volume ethylene glycol/water mixture is the transport media used in all liquid tests, unless otherwise specified. Direct flux pyroheliometer and diffuse measurements as required in Paragraphs 6.1.1, 6.1.3, and 7.1.3 are considered unnecessary for flat plate collector testing and, as a result, are included only as special test requirements.

Measurement accuracies generally meet specifications outlined in Paragraphs 6.2.2 and 7.1.7. The measurement techniques are also different from those specified in Paragraphs 7.1.4 and 7.1.5. Actual accuracies are given in Table 1. Techniques suggested for housing the ambient air temperature measure (Paragraph 7.1.4) are not observed. Also, testing has indicated that mixing devices specified in Paragraph 7.1.4 are not necessary. The measurement of wind velocity and solar flux is made only prior to each test; consequently, Paragraph 7.1.3 is not observed. Ambient air temperature measurements are made in the open immediately behind the collector; therefore, the housing requirements specified in Paragraph 7.1.2 are not observed.

The techniques used to determine collector parameters have been discussed in detail and are slightly different from those outlined in ASHRAE 93-77.

The theoretical power required by the collector prime mover (Paragraph 8.9) is not determined during each test. Although collector flowrate versus pressure drop data is run on each collector, it is not generated in the simulator facility. The simulator uniformity and collimation specifications given in the ASHRAE standard in Paragraphs 7.3.3 and 7.5.4 are not met by the facility. The actual values are recorded in earlier sections of this report. Also, the flow configurations suggested in the standard figures are not rigorously observed.



The configuration factor between the simulator and the tilt table at a 2.7 m (9 ft) distance is approximately 0.1 for a 1.2 by 2.4 m (4 by 8 ft) collector. A maximum value of 0.05 is indicated in Paragraph 7.3.5.

Performance equations have been adjusted in this document to consider the overall collector area in all efficiency evaluations. Also, the evaluation techniques given in Paragraphs 2.4 and 8.2 have been altered slightly.

## V. SIMULATOR TESTING

### A. Advantages of Simulator Testing

As stated earlier, the time savings associated with using the simulator in lieu of natural outdoor testing may be significant. In Huntsville, Alabama, the average mean percentage of sunshine for the year [12] is approximately 58 percent. The period available for outdoor testing (to satisfy ASHRAE 93-77 minimum flux requirements) generally occurs in a period between 10 a. m. and 2 p. m. solar time, depending on time of year. Since steady-state conditions must be achieved before valid performance data points can be acquired, relatively cloud free conditions are needed continuously for periods on the order of the collector time constant (1 to 10 min for most flat plate collectors). Because of the fluctuating nature of the outdoor environment, realization of simultaneous occurrence of these conditions is time consuming. These complications, combined with the need to set up stable collector fluid inlet conditions, require longer outdoor testing duration to achieve the same results. Estimates indicate 3 to 5 times as much time is required to secure a complete performance map outdoors as it does indoors. This manpower magnifying factor, coupled with the real problems associated with scheduling manpower (to make full use of test workmen's time when testing outdoors) gives an obvious advantage to indoor simulator testing.

In addition, disadvantages of outdoor testing must include inconsistency of test input boundary conditions. Due to varying outdoor conditions such as wind velocity, direction, solar flux, ambient air temperature, ratio of diffuse to direct solar flux, and changing incidence angle, determination of operating points for performance calculations is difficult. These variations introduce an error band in performance parameter determination which is virtually absent in the fixed environment in which simulator testing occurs.

These advantages make a strong case for solar simulator testing. There are, however, a number of negative aspects of indoor testing that should be noted for completeness. First, the simulation capability is never exact. As discussed, the uniformity, collimation, and spectral reproduction are important qualities whose reproduction of naturally occurring levels is never perfect. These imperfections must be addressed with respect to the effect on the parameters to be determined, as well as the desired quality of information. Second, the collector size which can be tested is limited to some extent by the illumination area. This limit is mitigated somewhat since testing of oversized flat plate collectors has been found to give reasonable results for collector sizes up to 50 percent larger than the simulator illumination capability.

The material cost of operating such a facility is significant, primarily because of lamp replacement costs. However, manpower expenditures override the economic disadvantages so that the overall economics of the simulator is favorable. Reference 13 contains a more complete examination of the economics of operating such a facility.

## B. Comparison of Outdoor and Simulated Indoor Tests

Proof of simulator fidelity is best achieved through comparative testing. This was done during initial startup of the facility by comparing collector efficiency data generated in outdoor testing with data from simulator tests. Two different collectors were tested in each environment with boundary conditions which were forced to be similar.

Testing of these collectors was performed first outdoors, then indoors so that simulator test could be run at nearly identical collector inlet temperature and average solar flux levels. The same fluid was used in corresponding tests. Fluid loop simulation equipment used outdoors was also used indoors, and identical instrumentation and acquisition equipment were used in both tests in an effort to null out equipment induced variables.

Although attempts were made to null out variations between indoor and outdoor tests, some parameters differed. Those parameters which varied between the two comparative tests were as follows:

ORIGINAL PAGE IS  
OF POOR QUALITY

1. Ambient air temperature
2. Sky sink temperature
3. Wind velocity fluctuations
4. Diffuse to total flux ratio
5. Incident angle.

Techniques to correct for variations in these parameters, as well as inside tilt angle and plate temperature differences, are given in Reference 14. However, no corrections were made herein because the resulting efficiency differences were small.

The two collectors used in these tests were nonproduction experimental models of an air collector and a liquid collector. The air collector was an MSFC in-house design (Fig. 41). The liquid collector tested was a small Honeywell model built under another collector study (Fig. 42).

The air collector tested has a nominal overall area of  $1.7 \text{ m}^2$  ( $18 \text{ ft}^2$ ) with dimensions of 0.9 by 1.8 m (3 by 6 ft). This collector has a single cover painted flat black. The backside insulation is an integral part of the collector urethane structure. The internal design uses a lengthwise flow separator to cause the air to traverse the collector length twice.

The liquid collector is  $1.1 \text{ m}^2$  ( $12 \text{ ft}^2$ ) in overall area; i. e., 0.9 by 1.2 m (3 by 4 ft). The collector has a selective iron oxide coating with two covers. Backside, edge, and end insulation are all of semirigid fiberglass. A summary of both air and liquid collector features is given in Table 3.

Comparative data for both indoor and outdoor tests for the air collector are given in Figure 43. Figure 44 gives similar data for the liquid tests. The air collector efficiency plots show the greatest dispersion. Nevertheless, these data points indicate efficiency comparisons within 6 percent of the measured outdoor value. Liquid collector data indicate agreement within 4 percent. Figures 45 and 46 give linear regression data fit plots of simulator generated efficiency data correlated against average absorber plate, average fluid, and fluid inlet temperature values for liquid and air collectors. It should be noted that the level of agreement between these two types of tests is within the calculation accuracy of the instrumentation. From these comparisons, the simulator reproduction of external conditions for the purpose of defining common flat plate efficiency was concluded to be very good.

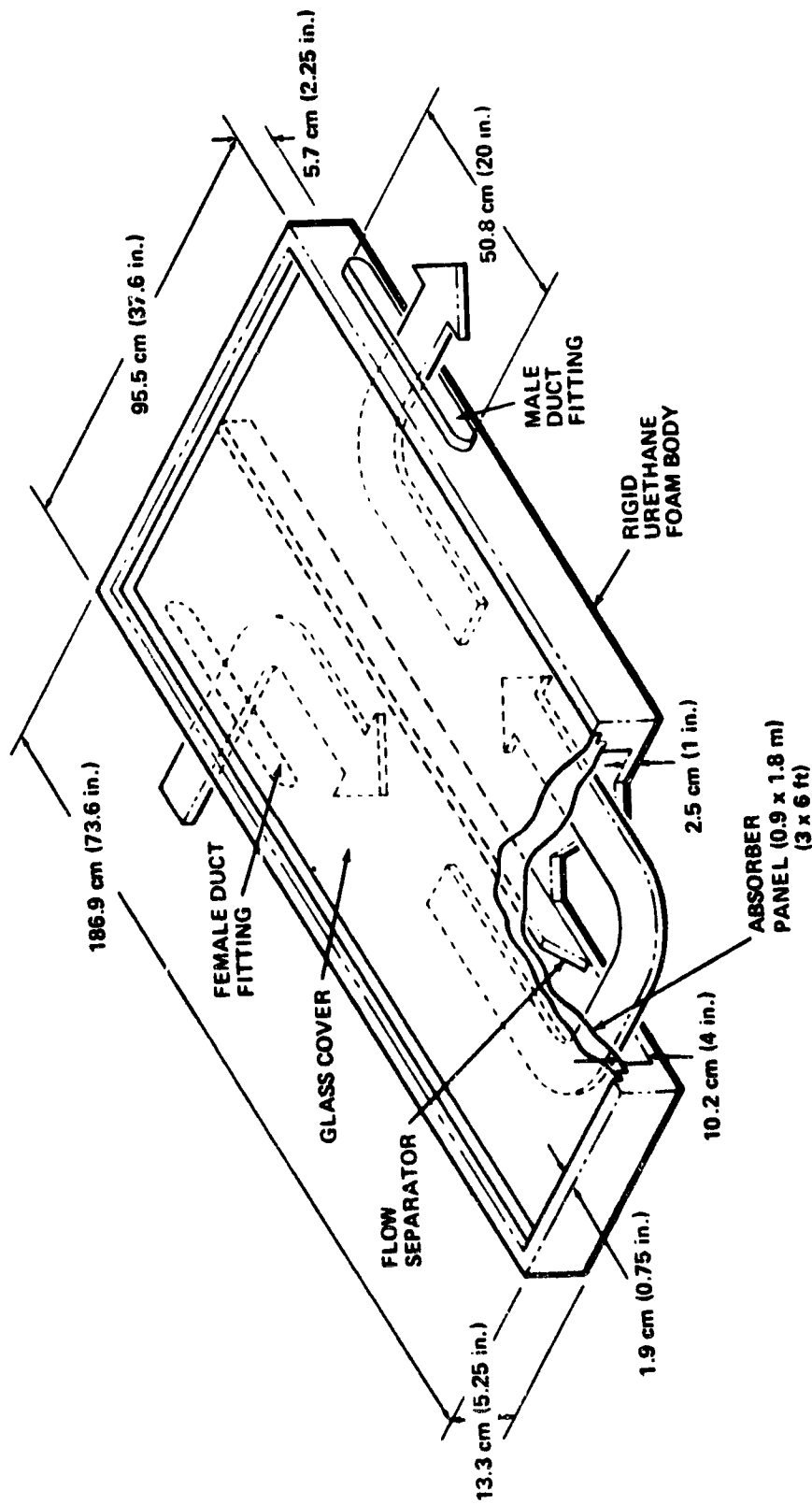


Figure 41. MSFC prototype air collector.

ORIGINAL PAGE IS  
OF POOR QUALITY.

LEGEND
L = 1.2 m (4 ft)
W = 0.9 m (3 ft)

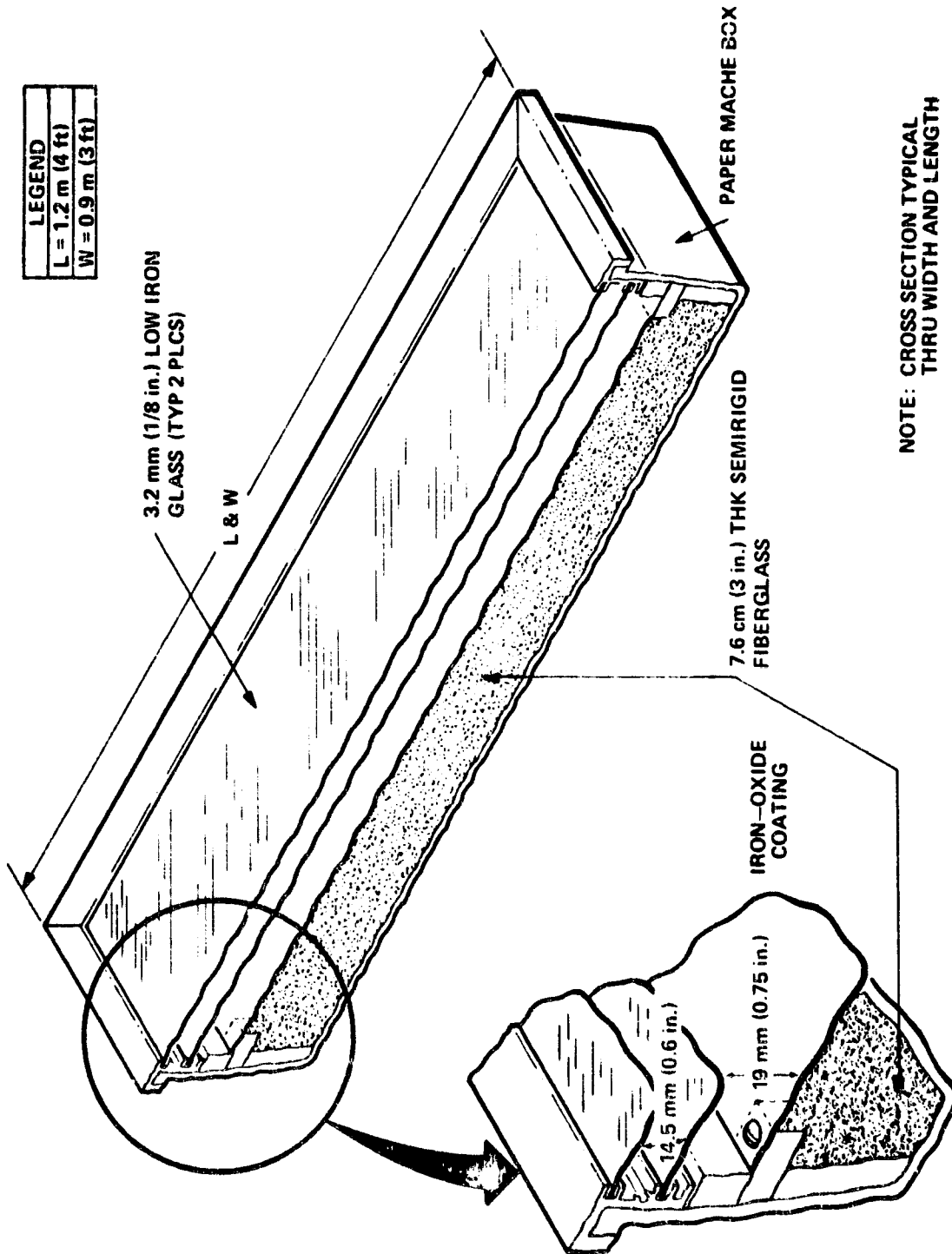


Figure 42. Prototype liquid collector.

TABLE 3. FEATURES OF COLLECTORS USED IN SIMULATOR EVALUATION

Collector #	Collector Dimensions			Collector Area			Collector Cost			In-situ Exchange	Sampling		Notes	
	Length (cm)	Width (cm)	Thickness (cm)	Length (cm)	Width (cm)	Area (cm <sup>2</sup> )	Area (ft <sup>2</sup> )	Area (m <sup>2</sup> )	Cost (\$)		Material	Frequency		Volume (ml)
MSU-1 (1968)	14.2 (5.6)	9.5 (3.7)	10.8 (4.2)	94.0 (11.5)	14.1 (1.5)	1328 (30.5)	15.2 (1.7)	16.5 (1.8)	DS Class	DS Class	1	100	2.0 (0.2)	1968
MSU-2 (1968)	14.2 (5.6)	9.5 (3.7)	10.8 (4.2)	94.0 (11.5)	14.1 (1.5)	1328 (30.5)	15.2 (1.7)	16.5 (1.8)	DS Class	DS Class	1	100	2.0 (0.2)	1968

Source: R. R. R. R.

ORIGINAL PAGE IS OF POOR QUALITY

ORIGINAL PAGE IS OF POOR QUALITY

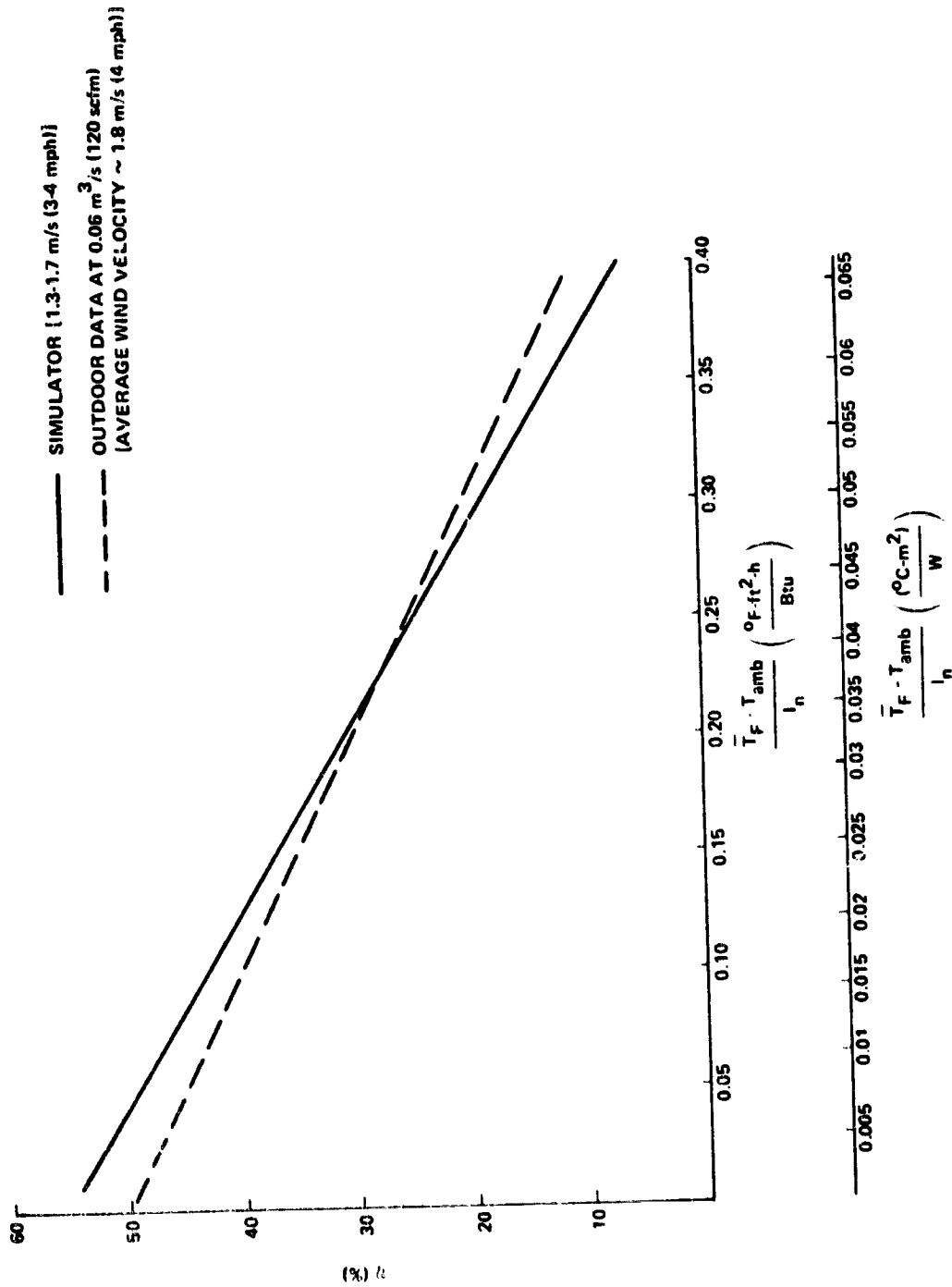


Figure 43. Air collector outdoor/indoor collector efficiency comparison.

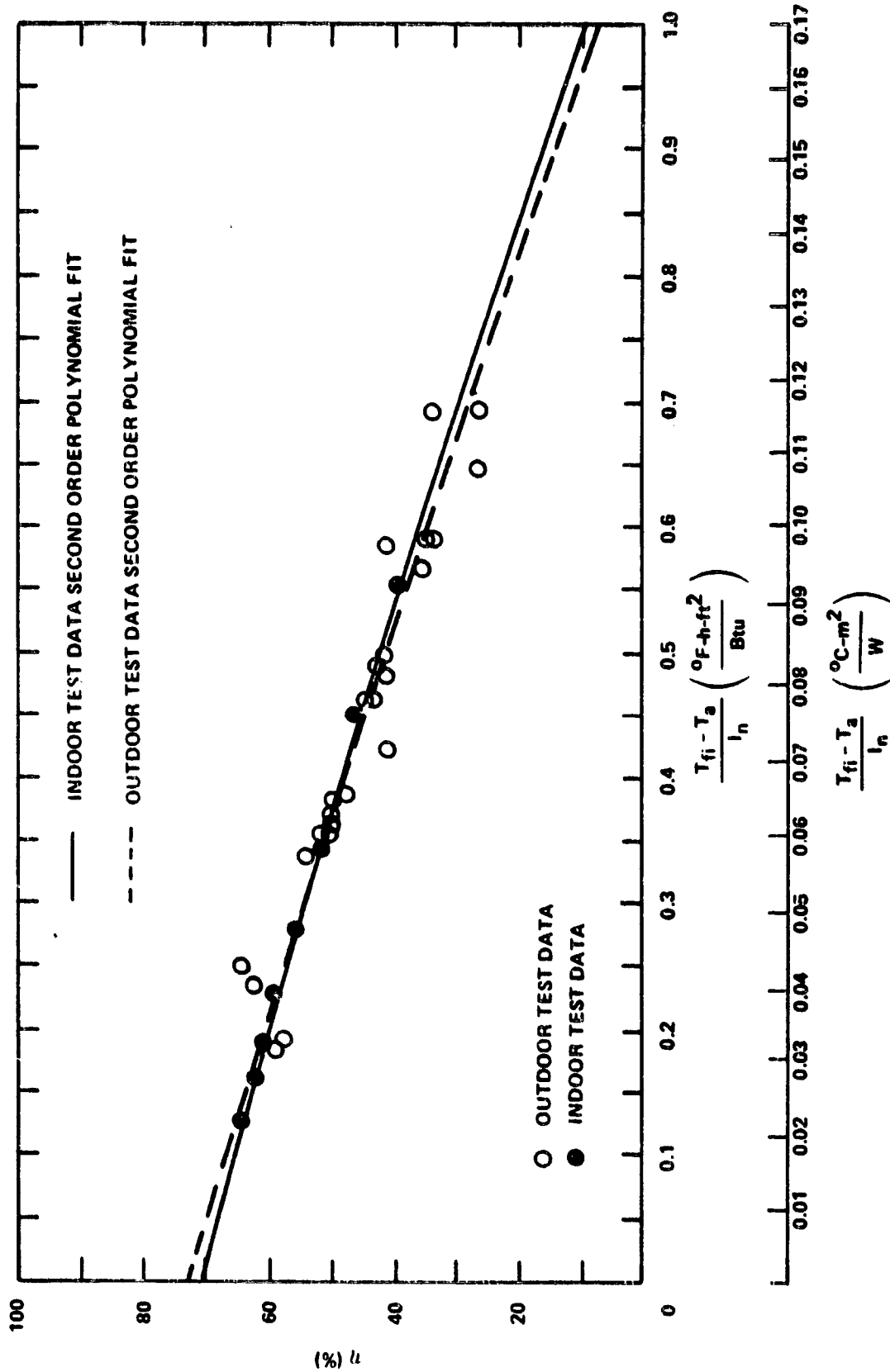


Figure 44. Liquid collector outdoor/simulator efficiency comparison.



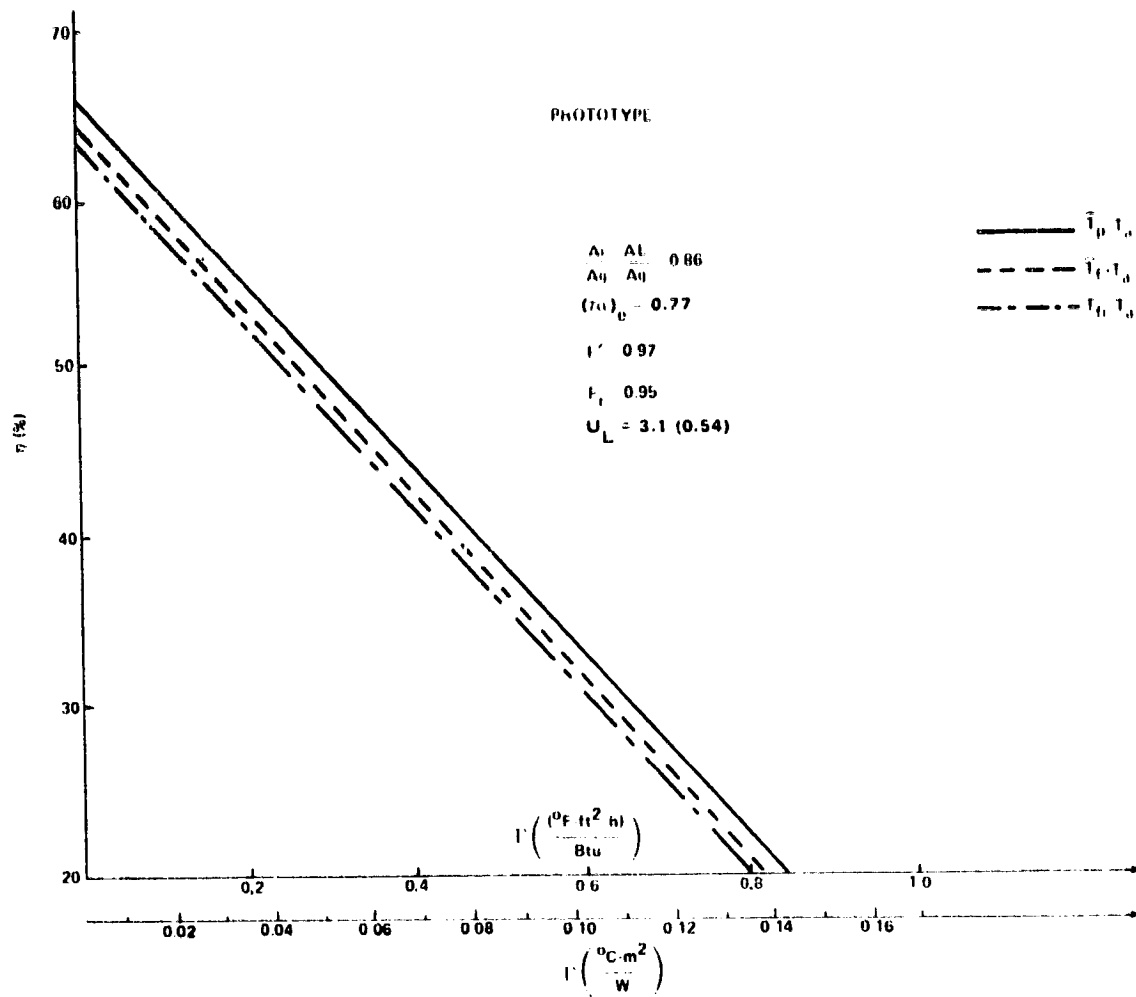


Figure 45. Liquid collector efficiency.

This conclusion is reasonable even though variations in flux intensity and collimation do exist between simulator conditions and true solar exposure because the high thermal diffusivity of the flat plate collector tends to null out the local thermal differences resulting from less than perfect simulation. Since the collector performance is nearly identical to that occurring under natural conditions, no further simulator improvements were deemed necessary.

ORIGINAL PAGE IS  
OF POOR QUALITY

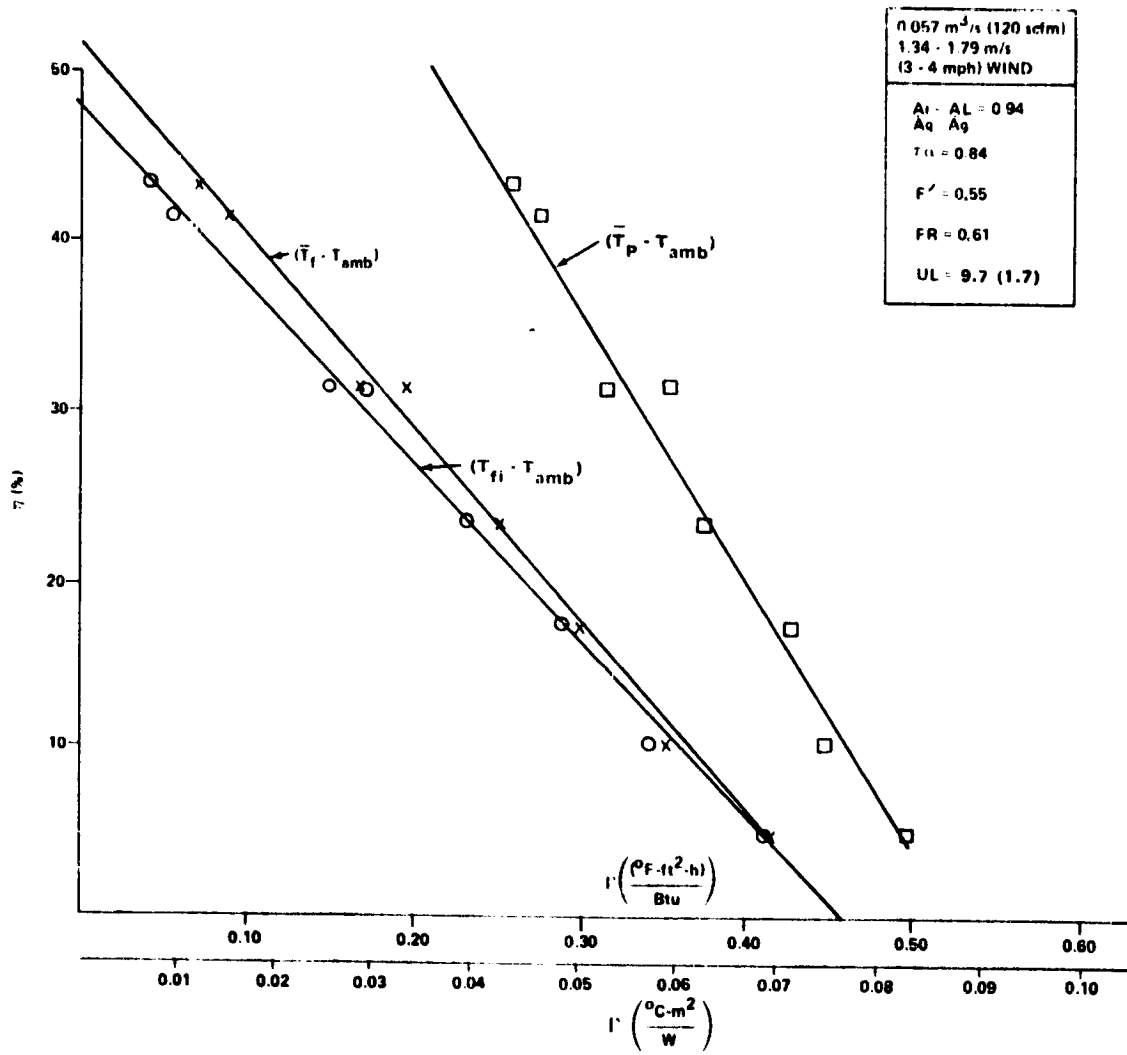


Figure 46. Air collector efficiency.

C-2

## C. Production Collector Tests

Since November, 1976 (when initial operations began) to the time of this writing, three liquid collectors have been tested to the ASHRAE 93-77 specifications. These were a Libby-Owen-Ford (LOF), a Honeywell, and a Daystar collector. All collectors were to be deployed in the MSFC development program. Table 4 presents a summary of the collector configurations for each production collector. Simulator efficiency curves and parameters for the three liquid collectors are given in Figure 47. Table 5 lists performance parameters calculated using data from the simulator.

A single production air collector has also been tested. This collector was a Solar Energy Products Company (SEPCO) collector. It was tested both indoors and outdoors for data comparison, since its overall area was greater than the irradiation capability of the simulator. Techniques used to generate analytically correct simulator data have been discussed earlier. Figure 48 gives the simulator generated efficiency plot, and Table 6 lists performance parameters resulting from these test conditions along with measured areas used to determine these parameters.

In addition to efficiency data, both incident angle modifier and time constant were generated for all collectors. These data are summarized for production collectors in Tables 7 and 8.

**ORIGINAL PAGE IS  
OF POOR QUALITY**

TABLE 4. SUMMARY OF PRODUCTION COLLECTOR FEATURES

Liquid									
Production Collector Part No.	Length <sup>a</sup>	Width <sup>a</sup>	Depth <sup>a</sup>	No. Covers	Type Covers / -	Backside Insulation	Type Coating	ρ, g/cm <sup>3</sup>	Weight <sup>a</sup>
Lennox Honeywell (LCS-1-1)	1.5 m (6 ft)	0.9 m (3 ft)	16.5 cm (6.5 in.)	2	0.32 cm (0.125 in.) Tempered-Etched / 0.96	Semirigid Fiberglass	Black Chrome Selective Coating	0.95-0.12	39.5 kg (15.5 lb)
Daystar (21B)	2.0 m (6 ft 5 in.)	0.6 m (2 ft 0.5 in.)	13.3 cm (5.25 in.)	1	0.48 cm (0.187 in.) Tempered / 0.90	Isocyanurate Foam	Nonselective Flat Black Paint	0.985-0.985	65.5 kg (145 lb)
LCF (112)	2.1 m (7 ft)	0.9 m (3 ft)	12.1 cm (4.75 in.)	2	0.32 cm (0.125 in.) Tempered / -	7.6 cm (3 in.) Treated Fiberglass	Nonselective Flat Black	0.977 -	59.0 kg (130 lb)

Air									
Production Collector Part No.	Length <sup>a</sup>	Width <sup>a</sup>	Depth <sup>a</sup>	No. Covers	Type Covers	Backside Insulation	Type Coating	ρ, g/cm <sup>3</sup>	Weight <sup>a</sup>
SEPCO (EF 212)	3.7 m (12 ft 2.75 in.)	0.6 m (2 ft 1.125 in.)	8.4 cm (3.313 in.)	1	0.48 cm (0.187 in.) Tempered / 0.90	Isocyanurate Foam Board	Nonselective Flat Black Paint	0.907-0.90	29.5 kg (65 lb)

a. Measured values.

ORIGINAL PAGE IS OF POOR QUALITY

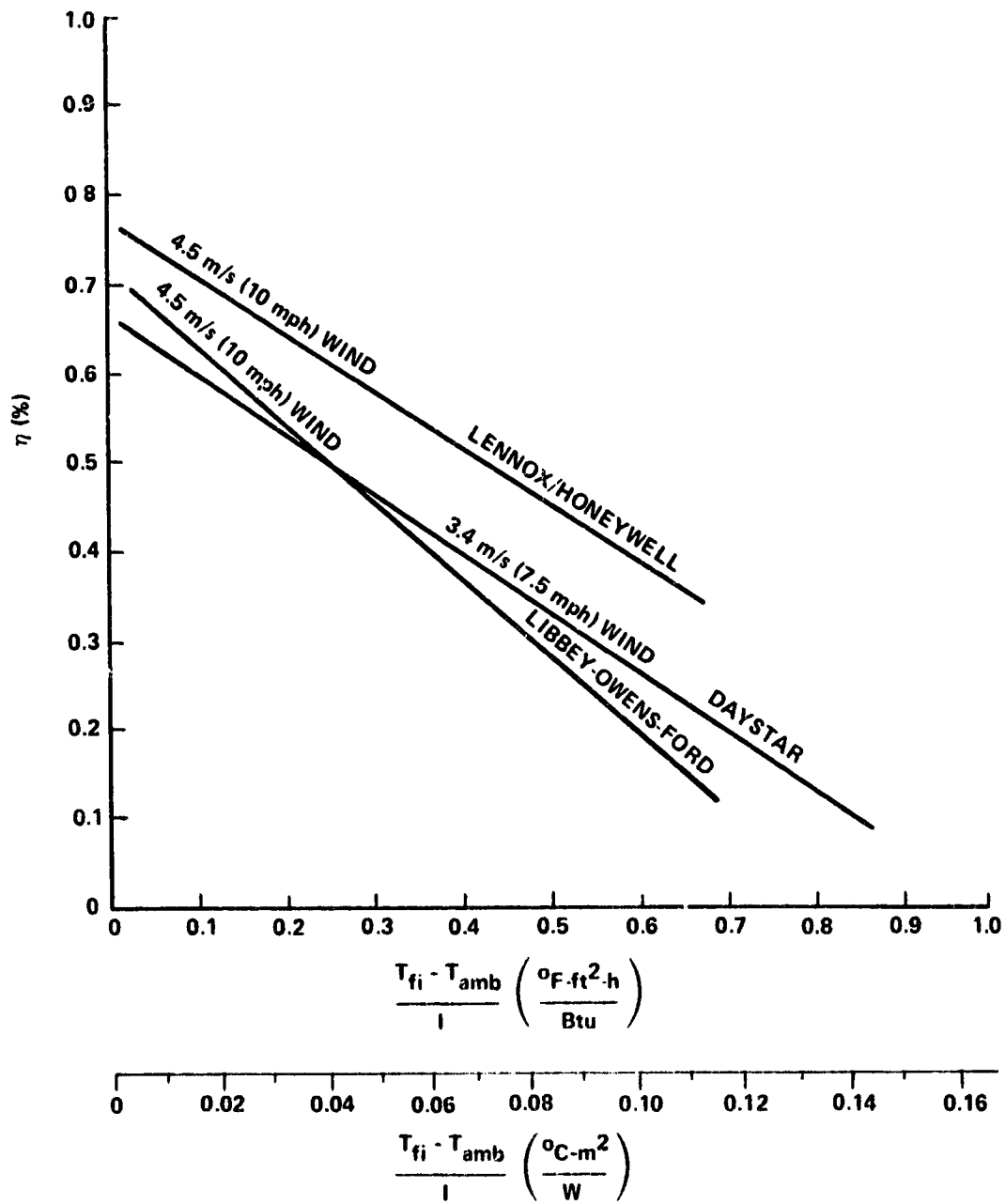


Figure 47. Liquid type production collector efficiency.

TABLE 5. PRODUCTION COLLECTOR (LIQUID)  
EFFICIENCY PARAMETERS

Production Collector Part No.	$A_g$	$A_a / A_L$	$(\tau\alpha)_{e,n}$	$F_R$	$F'$	$U_L$
Lennox/ Honeywell (LSC-18-1)	1.67 m <sup>2</sup> (18 ft <sup>2</sup> )	1.42 m <sup>2</sup> /1.42 m <sup>2</sup> (15.3 ft <sup>2</sup> /15.3 ft <sup>2</sup> )	0.89	0.89	0.91	4.20 W/m <sup>2</sup> °C (0.74 Btu/h-ft <sup>2</sup> -°F)
Daystar (21B)	2.32 m <sup>2</sup> (25 ft <sup>2</sup> )	1.95 m <sup>2</sup> /1.95 m <sup>2</sup> (21 ft <sup>2</sup> /21 ft <sup>2</sup> )	0.91	0.89	0.93	5.22 W/m <sup>2</sup> °C (0.92 Btu/h-ft <sup>2</sup> -°F)
LOF (1112)	1.95 m <sup>2</sup> (21 ft <sup>2</sup> )	1.83 m <sup>2</sup> /1.83 m <sup>2</sup> (19.74 ft <sup>2</sup> /19.74 ft <sup>2</sup> )	0.80	0.90	0.94	5.56 W/m <sup>2</sup> °C (0.98 Btu/h-ft <sup>2</sup> -°F)

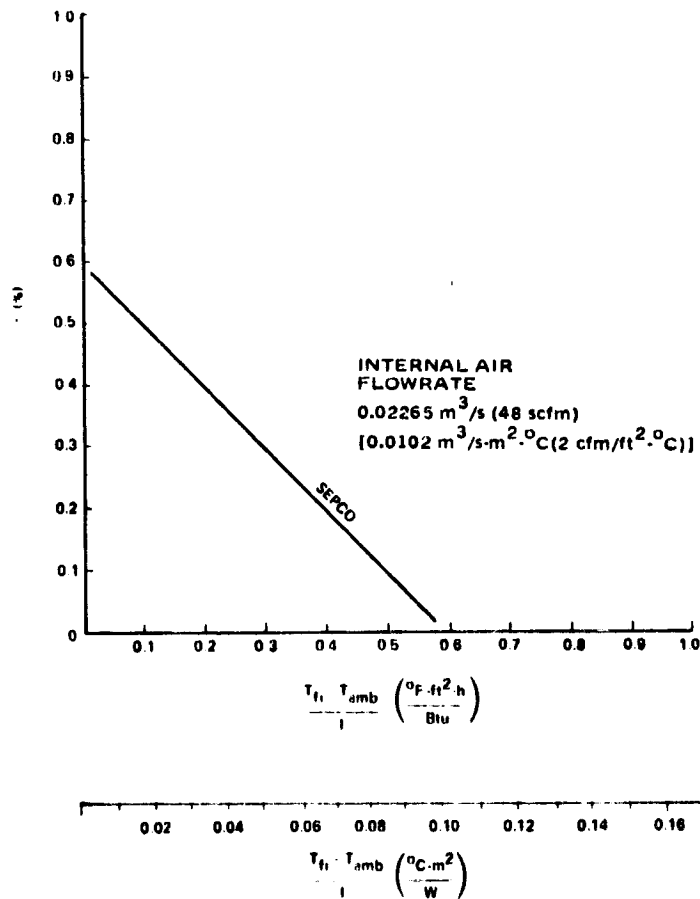


Figure 48. Air type production collector efficiency.

ORIGINAL PAGE IS  
OF POOR QUALITY

TABLE 6. PRODUCTION (AIR) COLLECTOR EFFICIENCY PARAMETERS

Production Collector Part No.	$A_R$	$A_a/A_f$	$(\tau\alpha)_{e,u}$	$F_R$	$F'$	$U_L$	$\dot{V}$
SEPCO (EF-212)	2.1 m <sup>2</sup> (22.5 ft <sup>2</sup> )	2.2 m <sup>2</sup> - 2.2 m <sup>2</sup> (24.0 ft <sup>2</sup> - 24.0 ft <sup>2</sup> )	0.90 1	0.71	0.91	6.9 W/m <sup>2</sup> -°C (1.2 Btu/h-ft <sup>2</sup> -°F)	0.02 m <sup>3</sup> /s (48 cfm)

Note: Since indoor-outdoor test comparisons were excellent, indoor data were used for these correlations.

TABLE 7. PRODUCTION COLLECTOR INCIDENT ANGLE MODIFIERS

$$K_{\alpha\tau} = 1 - b_o \left( \frac{1}{\cos \theta_i} - 1 \right)$$

Liquid

Production Collector Part No.	$b_o$
Lennox/Honeywell (LSC-18-1)	0.10
Daystar (218)	0.11
LOF (1112)	0.10

Air

Production Collector Part No.	$b_o$
SEPCO (EF-212)	0.13

Note: Air flowrate = 185 cfm

TABLE 8. PRODUCTION COLLECTOR TIME CONSTANT DATA

Liquid

Production Collector Part No.	Time Constant (min-s)
Lennox/ Honeywell (ISC-18-1)	2-0
Daystar (21B)	3-22
LOF (1112)	1-45

Air

Production Collector Part No.	Time Constant (min-s)
SEPCO (EF-212)	4-30

ORIGINAL PAGE IS  
OF POOR QUALITY



## REFERENCES

1. Yass, K. and Curtis, H. B.: Low-Cost Air Mass 2 Solar Simulator. NASA TM X-3059, presented at the United States Section Meeting of the International Solar Energy Society, Cleveland, Ohio, October 3-4, 1973.
2. Composite Solar Simulator Requirements for the Solar Heating and Cooling Development Program. NASA internal document SHC 2005, October 1975.
3. Griner, D. B.: MSFC Solar Simulator Test Plane Uniformity Measurement. NASA TM X-73364, December 1976.
4. Griner, D. B.: Test Plane Uniformity Analysis for the MSFC Solar Simulator Array. NASA TM X-64991, March 1976.
5. Procedure for Operation of the MSFC Simulator Facility. Unpublished NASA internal working document MTCP-FA-SHAC-100, November 1976.
6. Hottel and Woertz: The Performance of Flat-Plate Solar-Heat Collectors. Trans. ASME, February 1942, pp. 91-104.
7. Whillier: Solar Energy Collection and Its Utilization for House Heating. Sc D. Thesis, Mechanical Engineering Department, Massachusetts Institute of Technology, May 1953.
8. Hottel and Whillier: Evaluation of Flat-Plate Solar-Collector Performance. Volume II, Transactions of Conference on the Use of Solar Energy, University of Arizona, 1958, pp. 74-104.
9. Bliss, R. W.: The Derivation of General "Plate-Efficiency Factors" Useful in the Design of Flat-Plate Solar Heat Collectors, Solar Energy. Vol. 3, p. 55, 1959.
10. Method of Testing Solar Collectors Based on Thermal Performance. Prepared by ASHRAE Standard Committee 93-77, 1977.
11. Simon, F. F.: Flat-Plate Solar Collector Performance Evaluation with a Solar Simulator as a Basis for Collector Selection & Performance Prediction. NASA TM X-71793.

## REFERENCES (Concluded)

12. Weather Atlas of the United States. U.S. Environmental Data Service, U.S. Printing Office, June 1968.
13. Reily, J. C., Melton, D. E., Reese, D. R., Patrick, S. L., and Losey, R. E.: Economic Trade-offs Between the Performance of Collector Thermal Performance Tests on a Solar Simulator as Opposed to Outdoor Testing. Paper presented to 1977 meeting of American Section of International Solar Energy Society, June 1977.
14. Simon, F. F., and Burco, E. H.: Outdoor Flat-Plate Collector Performance Prediction from Solar Simulator Test Plan. NASA TM X-71009, presented at the 10th AIAA Thermal Physics Conference, Denver, Colorado, May 27, 1975.

ORIGINAL PAGE IS  
OF POOR QUALITY

APPENDIX A  
MEASUREMENT DEVICES

**PRECEDING PAGE BLANK NOT FILMED**

Instrumentation and Equipment for Air Collector Test

<u>Apparatus</u>	<u>Manufacturer / Model</u>	<u>Range / Accuracy</u>
Platinum Resistance Thermometer	Supplied by Collector Manufacturer	-17.8 to 260°C ± 0.3°C (0 to 500°F ± 0.5°F)
Pyranometer	Eppley — PSP	0 to 2522 W/m <sup>2</sup> (0 to 800 Btu/ft <sup>2</sup> · h) ± 3%
Air Loop	MSFC Supplied	N/A
Thermopile Differential	Medtherm	-17.8 to -6.7°C ± 0.03°C (0 to 20°F) ± 0.05°F
Directional Anemometer	Supplied by AMC	0 to 13.4 m/s (0 to 30 mph)
Flow Measurement Nozzle	Air Filter Testing Labs, 1.59 in. dia.	0.02 to 0.66 m <sup>3</sup> /s (35 to 130 cfm)
Platinum Resistance Thermometer	Hy-Cal	-17.8 to 260°C ± 0.3°C (0 to 500°F ± 0.5°F)
Strip Chart Recorder	Mosley 680	5 to 500 MV ± 2%
Floor Fan	MSFC Supplied	N/A
Solar Simulator	MSFC Supplied	See SHC 3006
Inclined Manometer	MSFC Supplied	0 to 0.1 m H <sub>2</sub> O ± 0.0003 m (0 to 4 in. H <sub>2</sub> O ± 0.01 in.)

ORIGINAL PAGE IS OF POOR QUALITY

<u>Apparatus</u>	<u>Manufacturer/Model</u>	<u>Range/Accuracy</u>
Differential Pressure Transducer	AMETEK 52D0010.AML	0 to 0.3 in H <sub>2</sub> O ± 0.5% 0 to 10 in. H <sub>2</sub> O ± 0.5%

Note: All transducers with the exception of the Eppley-PSP pyranometer used in recording test data are calibrated by either NASA or AMC calibration laboratories as required by MSFC MMH 5300.4C. The PSP pyranometer was calibrated by the manufacturer.

## Instrumentation and Equipment for Liquid Collector Test

<u>Apparatus</u>	<u>Manufacturer/Model</u>	<u>Range/Accuracy</u>
Platinum Resistance Thermometer	Supplied by Collector Manufacturer	-17.8 to 260°C ± 1.1°C (0 to 500°F ± 2°F)
Pyranometer	Eppley — PSP	2522 W/m <sup>2</sup> (0 to 800 Btu/ft <sup>2</sup> · h) ± 3%
Liquid Loop	MSFC Supplied	$6.3 \times 10^{-6}$ to $7.57 \times 10^{-5}$ m <sup>3</sup> /s (0.1 to 0.5 gpm)
Directional Anemometer	MSFC Supplied	0 to 13.4 m/s (0 to 30 mph)
Flowmeter	Foxboro/1/2-2 8IT3C1	$6.3 \times 10^{-6}$ to $5.7 \times 10^{-5}$ m <sup>3</sup> /s (0.1 to 0.9 ± 1% gpm)
Platinum Resistance Thermometer	Minco Products	15.6 to 121.1°C ± 0.03°C (60 to 250°F ± 0.05°F)
Strip Chart Recorder	Mosley 680	5 to 500 MV ± 2%
Floor Fan	MSFC Supplied	N/A
Solar Simulator	MSFC Supplied	See SHC 3063
Differential Pressure Sensor	Statham	0 to 68947.6 N/m <sup>2</sup> (0 to 10 psia ± 1%)
Platinum Resistance	Hy-Cal	-45.6 to 204.4°C ± 0.56°C (-50 to 400°F ± 1°F)

APPENDIX B  
COLLECTOR OBSERVATIONS AND MEASUREMENTS

**ORIGINAL PAGE IS  
OF POOR QUALITY**

Collector Observations

Date: \_\_\_\_\_

Mfr. \_\_\_\_\_

Model No. \_\_\_\_\_

Serial No. \_\_\_\_\_

Number of Cover(s) \_\_\_\_\_

Type of Cover(s) \_\_\_\_\_ inner; \_\_\_\_\_ outer

Cover Spacing(s) \_\_\_\_\_ m (in.) inner to outer \_\_\_\_\_ m (in.) inner to  
or outer to absorber \_\_\_\_\_ absorber

Coating Type \_\_\_\_\_

Coating Company \_\_\_\_\_

Insulation Type \_\_\_\_\_

Backside Insulation Thickness \_\_\_\_\_ m (in.)

Edge Insulation Thickness \_\_\_\_\_ m (in.)

End Insulation Thickness \_\_\_\_\_ m (in.)

Size of Unit:

Overall Collector Area \_\_\_\_\_ m<sup>2</sup> (in.<sup>2</sup>)

length \_\_\_\_\_ m (in.) × width \_\_\_\_\_ m (in.) ×

depth \_\_\_\_\_ m (in.)

Loss or Absorber area \_\_\_\_\_ m<sup>2</sup> (in.<sup>2</sup>)

length \_\_\_\_\_ m (in.) × width \_\_\_\_\_ m (in.)

Aperture area \_\_\_\_\_ m<sup>2</sup> (in.<sup>2</sup>)

length \_\_\_\_\_ m (in.) × width \_\_\_\_\_ m (in.) ×

depth \_\_\_\_\_ m (in.)

Comments & Other Observations: \_\_\_\_\_

\_\_\_\_\_

\_\_\_\_\_

Observer \_\_\_\_\_ Signed \_\_\_\_\_



Collector Measurements

Date: \_\_\_\_\_

Mfgr. \_\_\_\_\_

Model No. \_\_\_\_\_

Serial No. \_\_\_\_\_

$\tau$  Solar Normal Measurement \_\_\_\_\_

$\alpha$  Solar Normal Measurement \_\_\_\_\_

$c$  Normal Measurement \_\_\_\_\_

Test Date (s) \_\_\_\_\_, \_\_\_\_\_, \_\_\_\_\_, \_\_\_\_\_,  
\_\_\_\_\_

Test Incidence Angle (deg) \_\_\_\_\_

Test Tilt Angle (deg) \_\_\_\_\_

Test Azimuth Angle (deg) \_\_\_\_\_

Transport Fluid \_\_\_\_\_

Inlet Temperature Test Point ( $^{\circ}$ F) \_\_\_\_\_, \_\_\_\_\_, \_\_\_\_\_, \_\_\_\_\_, \_\_\_\_\_, \_\_\_\_\_

Corresponding Solar Flux  $W/m^2$  ( $\frac{Btu}{h-ft^2}$ ) \_\_\_\_\_, \_\_\_\_\_, \_\_\_\_\_, \_\_\_\_\_, \_\_\_\_\_, \_\_\_\_\_

Flowrate (s)  $kg/s$  or  $m^3/s$  (lb/h or cfm) \_\_\_\_\_

Ambient air temperature  $^{\circ}$ C ( $^{\circ}$ F) \_\_\_\_\_

Barometric Pressure in. Hg (mmHg) \_\_\_\_\_

Inlet Pressure  $N/m^2$  or  $mmHg$  (psi or in.  $H_2O$ ) \_\_\_\_\_

Wind Velocity  $m/s$  (mph) \_\_\_\_\_, \_\_\_\_\_, \_\_\_\_\_, \_\_\_\_\_, \_\_\_\_\_, \_\_\_\_\_,  
\_\_\_\_\_

Efficiency Data Parameters:

First order fit ( $y = a - bx$ )

a = \_\_\_\_\_ b = \_\_\_\_\_

ORIGINAL PAGE IS  
OF POOR QUALITY

Second order fit ( $y = a + bx + cx^2$ )

a = \_\_\_\_\_ b = \_\_\_\_\_ c = \_\_\_\_\_

Incident angle  $K_{\alpha\tau} = 1 + b \left( \frac{1}{\cos} - 1 \right)$

b = \_\_\_\_\_

Time constant \_\_\_\_\_ min

Comments and Other Observations: \_\_\_\_\_

\_\_\_\_\_

\_\_\_\_\_

\_\_\_\_\_

\_\_\_\_\_

\_\_\_\_\_

Observer \_\_\_\_\_ Signed \_\_\_\_\_

APPENDIX C  
SIMULATOR OPERATING PROCEDURES

1. Solar Simulator System Setup (Test Table Tilt Angle Equals the Tilt Angle of the Lamp Array)

The following is the procedure to be used for determining the system setup parameters to be used for collector testing. Figure C-1 shows the simulator testing setup and defines the symbols used.

1.1 A test flux level will be specified in the test requirements. Before the test specimen is mounted on the test table, a field map will be required to determine if the simulator power controller is set to produce the proper flux level. This procedure is described in Paragraph 2 and will have to be performed iteratively until the required flux level is obtained.

1.2 Mount the test specimen centered on the test table.

1.3 Measure the distance from the top of the test table to the top surface of the collector. Record this distance ( $d_c$ ).

1.4 Using the following formulae, compute  $h_{test}$  and  $L_{test}$ :

$$h_s = (d_{test} + d_c + d_t) (\cos \theta)$$

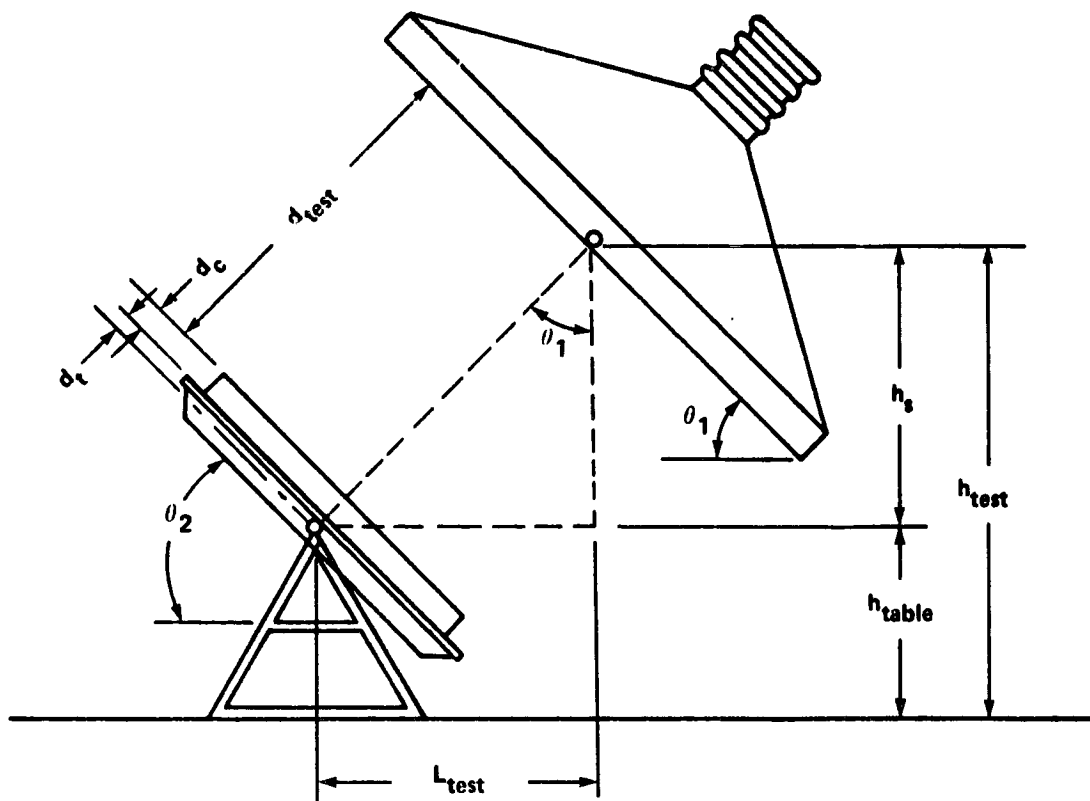
$$L_{test} = (d_{test} + d_c + d_t) (\sin \theta)$$

$$h_{test} = h_s + h_{table}$$

where

$$d_{test} = 2.7 \text{ m (9 ft)}$$

$$d_t = 0.4 \text{ m (1.5 in.)}$$



- $d_t$  = DISTANCE FROM TABLE PIVOT POINT TO TABLE SURFACE 0.04 m (1.5 in.)
- $d_c$  = DISTANCE FROM BACK SURFACE OF COLLECTOR TO ITS TOP SURFACE
- $d_{test}$  = DISTANCE FROM SIMULATOR LENS PLANE TO THE COLLECTOR TOP SURFACE 2.8 m (9 ft)
- $\theta_1$  = SIMULATOR TILT ANGLE
- $\theta_2$  = TABLE TILT ANGLE
- $h_{table}$  = VERTICAL DISTANCE FROM FLOOR TO TABLE PIVOT POINT 1.2 m (49 in.)
- $h_s$  = VERTICAL DISTANCE FROM TABLE PIVOT POINT TO THE CENTER POINT OF THE LENS PLANE
- $h_{test}$  = VERTICAL DISTANCE FROM FLOOR TO THE CENTER POINT OF THE LENS PLANE
- $L_{test}$  = HORIZONTAL DISTANCE FROM THE CENTER POINT OF THE LENS PLANE TO THE TABLE PIVOT POINT

Figure C-1. Solar simulator setup.

ORIGINAL PAGE IS  
OF POOR QUALITY

$\theta$  = Tilt angle

$h_{\text{table}} = 1.2 \text{ m (49 in.)}$  .

- 1.5 Using the chain hoist located at the right side of the simulator lamp array, adjust the array to the required tilt angle and the height ( $h_{\text{test}}$ ) as measured from the binding posts located on either side of the center of the lamp array.
- 1.6 Attach a plumb bob to each binding post mentioned in Step 1.5, and place a mark on the floor directly under each.
- 1.7 Draw a chalk line connecting the two points and bisect the chalk line.
- 1.8 Construct a line perpendicular to the line drawn in Step 1.7, passing through its center. This line should extend at least a distance ( $L_{\text{test}}$ ) in a northerly direction.
- 1.9 Measure off a distance equal to  $L_{\text{test}}$  from the baseline in Step 1.5 along the line drawn in Step 1.8 and mark this point.
- 1.10 Center the test table (left-to-right) over the line drawn in Step 1.8 and locate so that the pivot point of the table is directly over the mark made in Step 1.9.
- 1.11 Set the test table tilt angle to the angle required for testing.

The flow systems should now be set up, all instrumentation should be hooked up, and the system should be ready for testing.

## 2. Field Mapping

A field map should be taken prior to any series of tests and after any test during which a significant number of lamps have burned out. The following steps define the field map procedure:

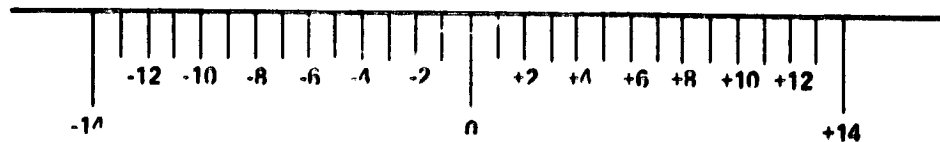
- 2.1 The simulator lamp array should be set up as described in Steps 1.4 through 1.11 using 0.25 m (9.4 in.) for  $d_c$  in the equations listed in Step 1.4.

- 2.2 Mount the mapping frame on the test table. The frame must be offset 15 cm (6 in.) either above or below the horizontal centerline of the test table and centered horizontally. This is necessary because of the valves mounted on the table. A pair of mounting holes in the frame should be aligned over the horizontal centerline of the table.
- 2.3 Mount the scanner bar in the holes in the frame over the horizontal centerline of the table. These holes will now be the zero reference point for vertical scans.
- 2.4 Connect the cable assembly from the scanner console to the detector carriage.
- 2.5 Power up the two 15 V power supplies in the scanner console and adjust both supplies to read 15 V.
- 2.6 Turn on the 400 cycle supply in Building 4619.
- 2.7 Turn on the power to the chart recorder; turn off the chart drive mechanism and raise the pen.
- 2.8 Turn on the simulator in accordance with the startup procedure (Paragraph 3.3). Allow the simulator to reach its operating temperature.
- 2.9 Move the detector carriage to the center of the scanner bar. Insure that the three-position scanner switch is in its center position.
- 2.10 Cover the detector and zero the galvanometer using the bias control. Zero the chart recorder.
- 2.11 Uncover the detector and adjust the gain control until the chart recorder pen is at approximately 80 percent of full scale. Repeat Step 2.10 to check for zero.
- 2.12 Repeat Steps 2.10 and 2.11 until the recorder reads zero when the detector is covered and approximately 80 percent when uncovered. Record this level on the chart recorder by lowering the pen and running the chart drive for a short time.

- 2.13 Switch the scanner switch to the L → R position. The carriage should move to the right reference side of the table (i.e., the right side of the table when looking at the simulator). The carriage should stop at the end of the carriage and the red indicator lamp should light.
- 2.14 Place the pyranometer on the carriage bar over the center of the table and take two readings from the computer printout of the flux level. Write these flux level readings on the chart recorder paper next to the mark recorded in Step 2.12.
- 2.15 Set the scanner switch to the R → L position, start the chart recorder, and lower the pen. Press the button next to the red indicator lamp until the lamp goes out. The carriage will now scan from right-to-left and stop on the left-hand side of the table, lighting the red indicator. Stop the chart recorder, raise the pen, and mark the vertical position (in this case zero) and R → L on the chart recorder paper to indicate a right-to-left scan.
- 2.16 Set the scanner switch to the L → R position, start the chart recorder, and lower the pen. Press the button next to the red indicator lamp until the lamp goes out. The carriage will scan from left-to-right and stop on the right-hand side of the table, lighting the red indicator. Stop the chart recorder, raise the pen, and mark the vertical position and L → R on the chart recorder paper.
- 2.17 Move the scanner bar down 0.025 m (6 in.) and repeat Steps 2.15 and 2.16, marking the chart with -0.025 m (-6 in.). Continue this process moving the bar 0.025 m (6 in.) at a time, repeating Steps 2.15 and 2.16 until -1.2 m (-18 in.) is scanned.
- 2.18 Now move the bar back to the zero point and repeat Steps 2.15 and 2.16. Repeat Step 2.17 only in a positive direction (up the table).
- 2.19 Review the chart recorder data to insure that the L → R chart is a mirror image of the R → L data. If it is not, or if the two "zero" maps do not agree, check the mapping system and the simulator. Then remap the field. If it is, proceed with the data analysis.
- 2.20 Using the right-to-left scans and a scale similar to the one which follows, read off the chart recorder amplitude at the points indicated on the scale.

ORIGINAL PAGE IS  
OF POOR QUALITY





2.21 Record the reading in tabular form from 1.2 m (48 in.) through 0 to -1.2 m (-48 in.) scan and forward this data along with the level measured in Step 2.12 and the flux level measured in Step 2.14 for analysis.

### 3. Startup Procedure

The following steps define the startup procedure:

- 3.1 Arrange with the Data Collection Group to monitor simulator operation.
- 3.2 Insure that screen is between simulator and the visitors' booth.

### 4. Simulator Powerup Procedure

The following steps define the powerup procedure:

- 4.1 Open cooling water hand valve on the power controller console (A on Fig. C-2).
- 4.2 Close main supply breaker (480 V) located on power duct above the door to Room 158A, Building 4619.
- 4.3 Close main circuit breaker on Panel AA-3.
- 4.4 Close control circuit breaker (No. 2) on Panel AA-3.
- 4.5 Close exhaust fan circuit breaker (No. 18) on Panel AA-3.
- 4.6 Check over-temperature meter relay for a setting of 93.3°C (200°F) (B on Fig. C-2).
- 4.7 Set air flow damper to maximum open position (C on Fig. C-2).

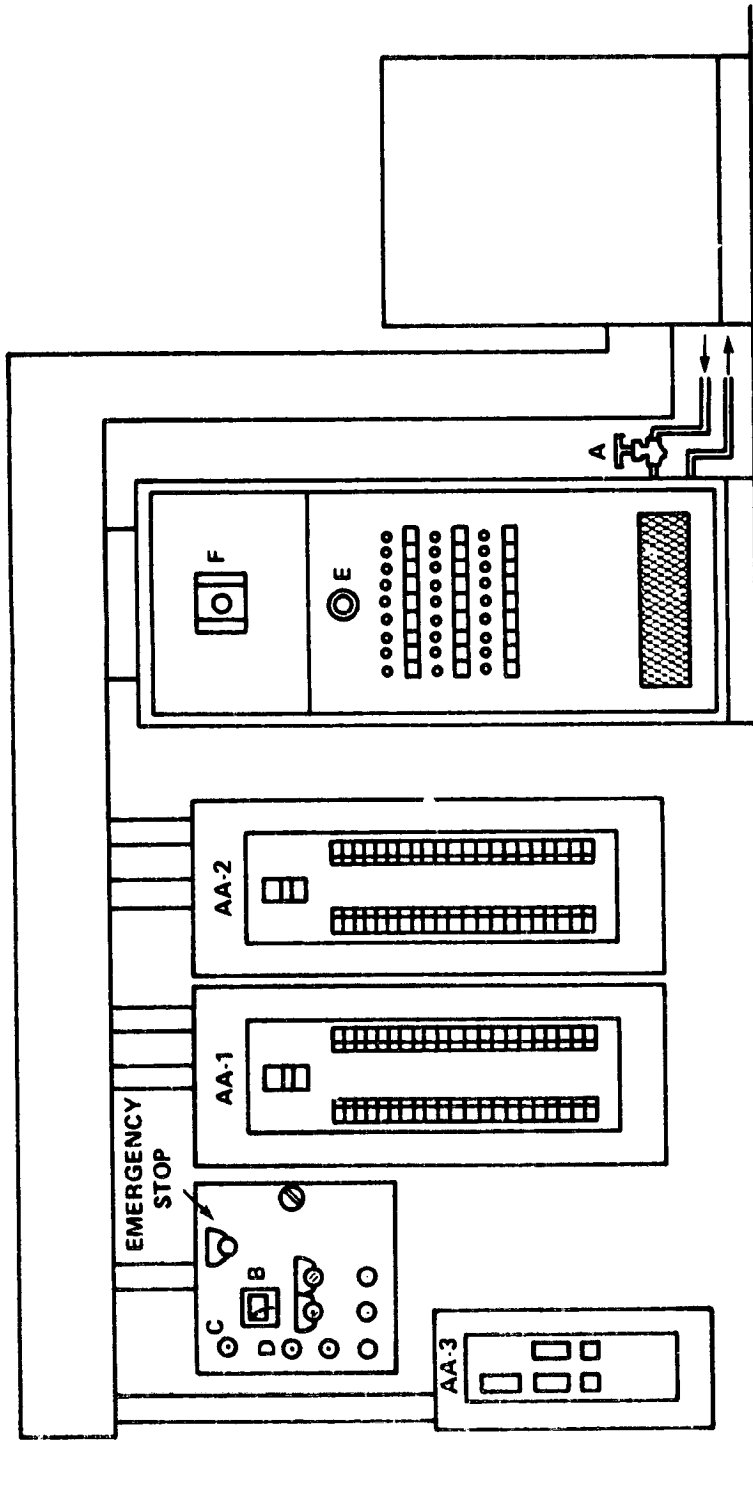


Figure C-2. Solar simulator controls.

ORIGINAL PAGE IS  
OF POOR QUALITY

- 4.8 Start exhaust fan using start button on fan control panel (D on Fig. C-2).
- 4.9 Set level potentiometer on power controller console to zero (E on Fig. C-2).
- 4.10 Close main circuit breaker on power controller console (F on Fig. C-2).
- 4.11 Check Panels AA-1 and AA-2 to insure that all lamp circuit breakers required for simulator operation are turned on.
- 4.12 Close main circuit breaker on Panel AA-1.
- 4.13 Close main circuit breaker on Panel AA-2.
- 4.14 Gradually increase level potentiometer on power controller to desired operating point.
- 4.15 Adjust air flow damper to obtain the prescribed operating temperature (TBD) as monitored on the computer teletype.

#### 5. Simulator Power-Down Procedure

The following steps define the power-down procedure:

- 5.1 Set level potentiometer on power controller to zero.
- 5.2 Open main circuit breaker on Panel AA-1.
- 5.3 Open main circuit breaker on Panel AA-2.
- 5.4 Open main circuit breaker on power controller console.
- 5.5 Set air flow damper to maximum open position.
- 5.6 When lamp base temperature is below 38°C (100° F), as observed on computer teletype, stop exhaust fan using stop button on fan control panel (G on Fig. C-2).
- 5.7 Open exhaust fan circuit breaker (No. 18) on Panel AA-3.

- 5.8 Open control circuit breaker (No. 2) on Panel AA-3.
- 5.9 Open main circuit breaker on Panel AA-3.
- 5.10 Open main supply breaker (480 V) located on power duct above the door of Room 158A, Building 4619.
- 5.11 Close cooling water hand valve on the power controller console.
- 6. Shut-Down Procedure

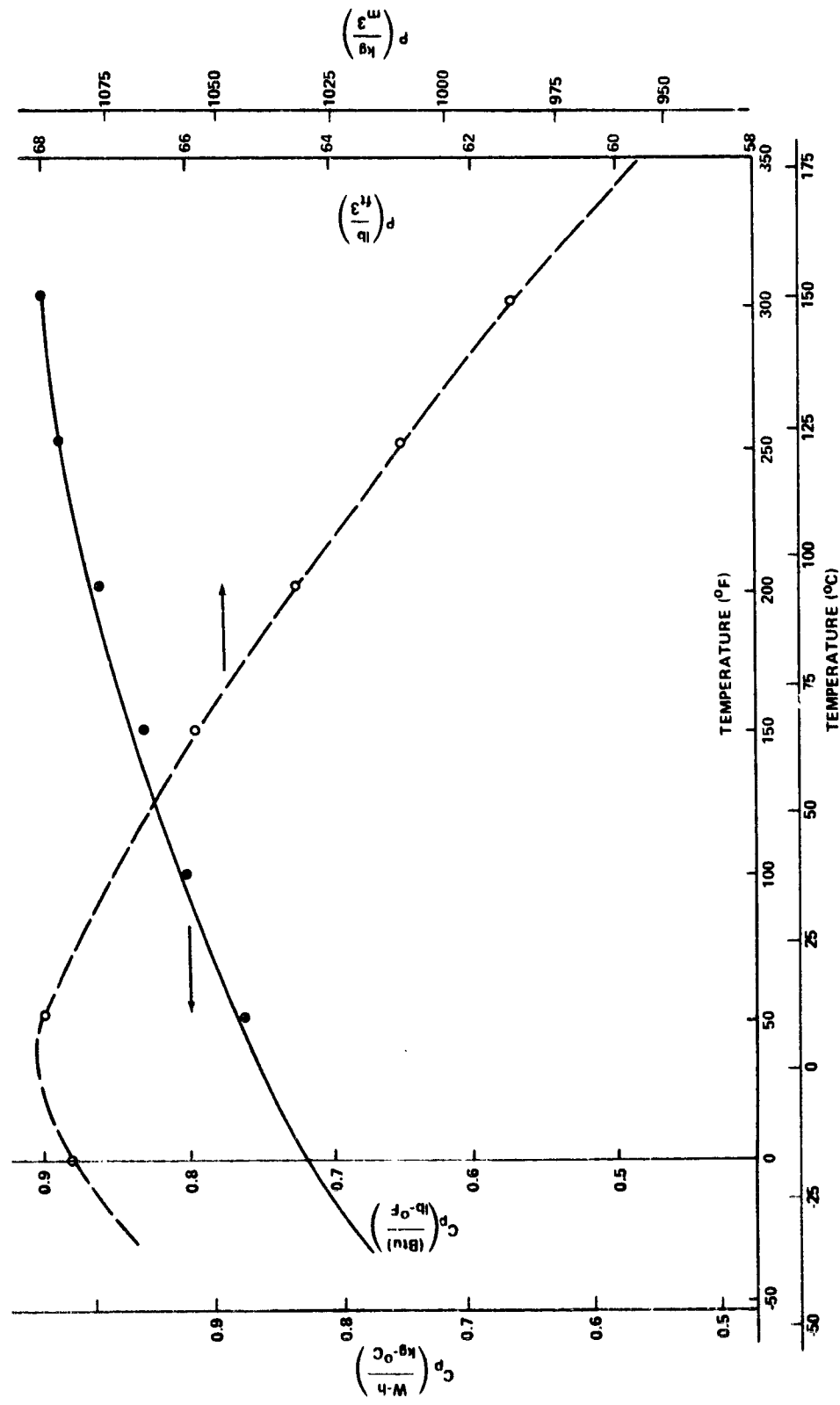
Notify the Data Collection Group that simulator operation has been completed.

APPENDIX D

PROPERTIES OF 50 PERCENT BY VOLUME (52.7 PERCENT  
BY WEIGHT) ETHYLENE GLYCOL IN WATER

ORIGINAL PAGE IS  
OF POOR QUALITY

50% BY VOL (52.7% BY WT) ETHYLENE GLYCOL IN WATER

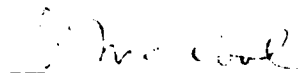


## APPROVAL

### USE OF THE MARSHALL SPACE FLIGHT CENTER SOLAR SIMULATOR IN COLLECTOR PERFORMANCE EVALUATION

By William R. Humphries

The information in this report has been reviewed for security classification. Review of any information concerning Department of Defense or nuclear energy activities or programs has been made by the MSFC Security Classification Officer. This report, in its entirety, has been determined to be unclassified.



---

A. A. McCOOL

Director, Structures and Propulsion Laboratory

ORIGINAL PAGE IS  
OF POOR QUALITY